Technical developments for real-time MRI-guided HDR brachytherapy

Ellis Beld

Technical developments for real-time MRI-guided HDR brachytherapy
PhD thesis, Utrecht University, The Netherlands

Cover: Mt. Rinjani, Indonesia (by Ellis Beld)
Lay-out: Ellis Beld
Typeset: LaTeX
Printed by: Proefschriftmaken
ISBN: 978-94-6380-264-2

Financial support for publication of this thesis was kindly provided by Elekta.

Technical developments for real-time MRI-guided HDR brachytherapy

Technische ontwikkelingen voor real-time MRI-geleide HDR brachytherapie

(met een samenvatting in het Nederlands)

Proefschrift

ter verkrijging van de graad van doctor aan de Universiteit Utrecht op gezag van de rector magnificus, prof.dr. H.R.B.M. Kummeling, ingevolge het besluit van het college voor promoties in het openbaar te verdedigen op donderdag 28 maart 2019 des middags te 12.45 uur

door

Ellis Beld
geboren op 12 oktober 1988 te Goor

Promotoren:	Prof. dr. ir. J.J.W. Lagendijk
	Prof. dr. ir. M.A. Viergever
Copromotoren:	Dr. ir. M.A. Moerland
	Dr. ir. P.R. Seevinck

Contents

Chapter 1

Introduction

1.1 Brachytherapy

Brachytherapy is a treatment which uses radioactive sources for radiation delivery from inside a patient's body at a short distance, i.e. inside or in the vicinity of the target volume. The technique allows to deliver a high dose locally to the tumor, with a steep dose fall-off in the surrounding healthy tissue. Accordingly, brachytherapy offers the possibility to irradiate cancerous tissue while sparing the surrounding organs at risk as much as possible. Application of the radioactive source can be interstitial (sources implanted within tumor tissue), intracavitary (sources placed into body cavities) or on the surface (sources placed on molds on the surface of tissue to be treated) [1]. Depending on the type and stage of cancer, brachytherapy can be provided as a single treatment modality or combined with external beam radiotherapy.

Brachytherapy can be divided in two categories: permanent implant brachytherapy and stepping source brachytherapy (or temporary implant brachytherapy). Permanent implant brachytherapy involves the insertion of small radioactive sources (most commonly iodine-125), called seeds, permanently into the tumor. The seeds, typically between 40 and 100 for a prostate implant, emit low levels of radiation for several months and are left in place permanently while the radiation decays to a negligible level. This type of treatment is often referred to as low-dose-rate (LDR) brachytherapy. On the other hand, stepping source brachytherapy is involved with the use of a single radioactive source with a high activity that is directed temporarily into implanted catheters or applicators. First, several catheters are placed close to, or inside, the tumor. Then, a remote afterloading device is utilized to remotely guide the source into each implanted catheter to deliver the prescribed dose. After delivery of the prescribed dose, the source is retracted and guided back into a shielded safe inside the afterloading device. Stepping source brachytherapy can be given as pulsed-dose-rate (PDR) brachytherapy and as high-dose-rate (HDR) brachytherapy. PDR brachytherapy is applied to deliver the dose in a large number of small pulses, i.e. fractions. A fraction is given every one or two hours and the total treatment may last up to several days. In high-dose-rate (HDR) brachytherapy, one or several fractions with a high dose are delivered using a source of high activity, most commonly iridium-192 (with an initial activity of $\sim$370 GBq [2]).

As stated above, HDR brachytherapy involves the utilization of a remote afterloading device to remotely deliver the prescribed dose to the patient. The HDR afterloading device contains a single source of high activity, most commonly Ir-192. The source consists of a small line source in a steel capsule, which is welded to the end of a flexible source wire (also called drive cable). When not in use, the source is stored in a shielded safe inside the afterloader. The afterloader is equipped with several channels that can be connected to the implanted applicators or catheters in the patient by tubes referred to as transfer tubes. To deliver the dose to the patient, the source is sent out and directed through the individual channels into the implanted applicators or catheters. The source is directed to programmed positions within the catheters, i.e. the dwell positions. The source will remain at each dwell position for a planned period of time, i.e. the source dwell time, specified for each individual dwell position. Accordingly, the source steps through the catheters to deliver the planned dose to the target volume, after which the source is retracted and stored in the safe. This source

stepping procedure is accomplished by a drive mechanism consisting of stepper motors inside the afterloader, controlled by a remote computer.

1.2 MRI-guided prostate HDR brachytherapy

1.2.1 Prostate HDR brachytherapy

Prostate cancer is one of the important tumor types for which HDR brachytherapy has been applied. Besides HDR brachytherapy, several other effective treatments have been established for prostate cancer, including prostatectomy, androgen deprivation therapy, external beam radiotherapy, and LDR brachytherapy, or a combination of these. HDR brachytherapy has proven to be an effective treatment [3–5]. The large advantage of HDR brachytherapy is the ability to obtain an optimal dose distribution due to the possibility to accurately control the source and vary the source dwell times during treatment [6, 7]. HDR brachytherapy can be delivered as a boost treatment after external beam radiotherapy, but is increasingly used as a monotherapy as an alternative to LDR brachytherapy. HDR brachytherapy has demonstrated favorable results as monotherapy for whole gland prostate cancer [7–11]. Furthermore, hypofractionation has gained interest as prostate tumors exhibit a low α/β-ratio, which makes them radiobiologically eligible for hypofractionated schemes [6, 12]. Minimization of the number of treatment fractions has shown good initial outcomes [13, 14], and may reduce costs and the risk associated with the treatment, while increasing the patient convenience [14, 15]. Consequently, single-fraction HDR brachytherapy may become the preferred treatment for low and intermediate-risk disease [16]. Additionally, single-fraction MRI-guided HDR brachytherapy has achieved positive results for salvage treatment of radiorecurrent prostate cancer [17, 18].

1.2.2 Magnetic resonance imaging for prostate HDR brachytherapy

Magnetic resonance imaging (MRI) is the preferred and recommended imaging modality for guidance of prostate HDR brachytherapy [19–22]. MRI provides superior soft tissue contrast and can play a role in a variety of steps in the prostate brachytherapy process: patient selection, simulation, treatment planning, implant, postimplant assessment, and follow-up and surveillance. Multiparametric MRI is increasingly applied as a standard for diagnostic imaging, where the following functional imaging techniques are included: diffusion weighted imaging (DWI), dynamic contrast enhanced (DCE) MRI, and less frequently MR spectroscopy [23]. Another component of the multiparametric MRI exam is high-resolution T2-weighted imaging, as it provides a good prostate gland visualization and discrimination between the peripheral zone and the central gland [24, 25]. HDR brachytherapy treatment planning is often performed based on the multiparametric MRI exam, in which particularly T2-weighted imaging and DWI have demonstrated considerable promise in the detection and

localization of prostate cancer [26–28]. MRI can be used for the pre-treatment plan as well as the for dose optimization during intraoperative treatment planning after catheter insertion [29]. Additionally, MRI has been applied for real-time guidance during the implantation of LDR brachytherapy seeds as well as HDR brachytherapy needles [19, 30]. Besides the applications for HDR brachytherapy, MRI has also been incorporated to provide postimplant dosimetry for LDR brachytherapy [31, 32]. Lastly, MRI is valuable to evaluate recurrent disease in men with a rising prostate-specific antigen (PSA) level after prostate cancer treatment. Therefore, MRI plays an important role in salvage brachytherapy [18, 33].

Several centers have been working on the application of MR imaging for guidance during HDR brachytherapy, for varying tumor sites, with different treatment designs. MRI guidance has been applied for verification of the needle positions after insertion or for real-time visualization or tracking during needle insertion [19, 34, 35]. Both open and closed bore MRI systems have been applied for these purposes. In most situations, the patient needs to be transferred to a different table after MR imaging and verification of the needle positions, to transfer the patient to the shielded treatment room in which the radiation is delivered. Frequently, this involves a transfer of the patient from the radiology department to the radiotherapy department.

1.2.3 Prostate HDR brachytherapy at UMC Utrecht

Since 2013, focal HDR brachytherapy has been performed in the UMC Utrecht for primary treatment of prostate cancer and salvage treatment of radiorecurrent prostate cancer. The treatment is given in a single fraction of 19 Gy, prescribed as 19 Gy to at least 95% (D_{95}) of the clinical target volume (CTV). This treatment is given under general or spinal anesthesia on an outpatient basis. Accurate and safe dose delivery is pursued by MR imaging pre-treatment for treatment planning and intraoperatively after catheter insertion as well as directly before irradiation.

The HDR brachytherapy treatment in the UMC Utrecht is performed in an HDR brachytherapy MRI suite. This means that the department possesses an HDR brachytherapy bunker in which a 1.5 T MRI system is located. A schematic overview of the workflow of the HDR brachytherapy treatment performed clinically is shown in Figure 1.1. An initial treatment plan is made based on a multiparametric diagnostic MRI exam. Before the start of the treatment, the patient is positioned on the MRI table top (a trolley) which is moved to the room adjacent to the MRI room. Here, the catheter insertion takes place under ultrasound guidance and using a template grid to guide the catheters to the predefined positions. The catheters used are made of plastic. After catheter insertion, the patient is moved to the adjacent MRI scanner room and brought into the scanner. The intraoperative MRI exam is taken, consisting of: a 2D volumetric T_2-weighted turbo spin echo sequence for delineation, a 3D balanced steady-state free precession (bSSFP) sequence for delineation and catheter reconstruction, and a 2D volumetric T_1-weighted turbo spin echo sequence for additional checks of the catheter positions. Then the patient is moved back out of the MRI bore. The intraoperative MRI scans (the T_2-weighted and 3D bSSFP scans) are fused with the diagnostic treatment planning scan. The

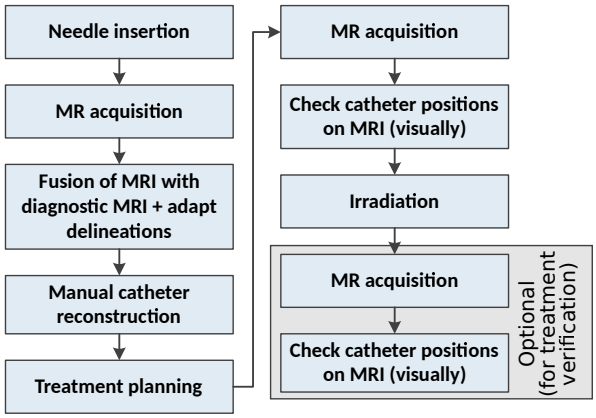

Figure 1.1 Schematic overview of the clinical workflow of the prostate HDR brachytherapy treatment in the UMC Utrecht. The last two steps to acquire another set of MR images and perform an additional check of the catheter positions is optional, as a treatment verification step.

delineations are propagated from the planning MRI to the intraoperative MRI and manually adapted by the radiation oncologist. The catheter tracks are reconstructed manually, where the position of the catheter tip and the entry point are indicated in the bSSFP scan. A final treatment plan is made based on the intraoperative MRI scan with delineations and the reconstructed catheter positions. The patient is moved one more time in the MRI bore for an additional MRI acquisition to check if the catheters are still in the correct positions with respect to the anatomy. In a situation where severe movements of the catheters were observed, the treatment plan can be adapted. Then, the afterloader is connected and the radiation is delivered in a remotely controlled process using an HDR afterloading device. As an extra option, the patient can be moved into the MRI bore again after irradiation for an additional check of the catheter positions, as a treatment verification step.

1.3 Developments in treatment verification

In HDR brachytherapy, high doses are delivered in short periods of time, especially in single fraction treatments. Errors in source positioning can have an enormous impact on the delivered dose due to steep dose gradients. Because of the large number of manual operations, HDR brachytherapy is concerned with relatively high chances on errors/incidents. Examples of reported errors are: reconstruction errors, wrong catheter/indexer length, catheter mislabeling, and incorrect afterloader connection [36, 37]. Possible sources of errors not related to human interactions are afterloader malfunction and applicator displacements. To prevent or detect these errors, treatment verification is highly important.

Considerable research has been conducted on the development of techniques for treatment verification of HDR brachytherapy. A technique which is applied in clinical settings is the

use of repeated imaging to assess anatomical changes and catheter movements for a varying range of organs. Repeated imaging, either CT or MRI, proved the need for position verification for subsequent fractions [38] and position verification directly before treatment [39]. Furthermore, repeated imaging is useful for adaptive treatment planning [40] and provides information for dosimetric evaluations when performed directly before and after the treatment [41, 42].

The technique of *in vivo* dosimetry focuses on determination of the delivered dose in certain positions *in vivo* close to the target volume using dosimetric systems, for example thermoluminescent dosimeters (TLD) [43, 44], metal oxide semiconductor field effect transistor detectors (MOSFET) [45–47], and optically stimulated luminescent dosimeters [48–50]. *In vivo* dosimetry has been demonstrated in real time by a source tracking approach using a luminescent point dosimeter [51], semiconductor detectors [52] and noninvasive EPID panels [53, 54]. However, *in vivo* dosimetry techniques are involved with large measurement uncertainties and are only sensitive to gross errors [55], as the dose is measured in single points in locations where a steep dose gradient is present.

Electromagnetic (EM) tracking involves the detection of small coils in an electromagnetic field generated by a field emitter, and can be used to determine the position and orientation of a catheter [56–58]. An other technique for needle tracking is fiber Bragg gratings (FBG)-based sensing [59], which involves measurement of the deflection of a needle. However, these tracking techniques apply their own coordinate system independent of the anatomical coordinate system, which requires a registration and can, therefore, lead to errors.

Except for the method of repeated imaging, the techniques mentioned in this section have their limitations and are currently not commercially available [55]. Therefore, these techniques are not clinically applied.

1.4 Magnetic susceptibility and device tracking

1.4.1 Magnetic susceptibility

Medical instruments are generally made of paramagnetic materials and, therefore, induce artifacts in the MR images related to their magnetic susceptibility. Also the instruments applied in HDR brachytherapy, for example a titanium needle or an HDR brachytherapy (dummy) source, exhibit this behavior. The magnetic susceptibility of a material is a property that quantifies the tendency of a material to interact with and distort a magnetic field; it denotes the extent to which a material becomes magnetized when placed in an external magnetic field. The magnetic susceptibility, χ, is defined as the ratio of the magnetization, M, to the applied magnetic field, H [60]:

$$\chi = M/H. \tag{1.1}$$

When placed in an external magnetic field, most biological tissues generate a weak magnetic field in the direction opposed to the direction of the applied magnetic field (i.e. a dispersion

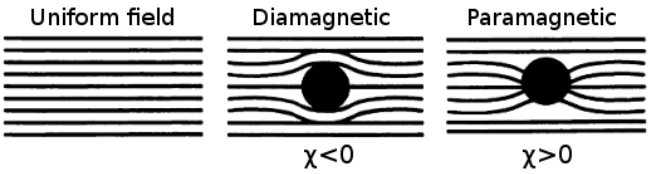

Figure 1.2 Schematic depiction of the differences between diamagnetic and paramagnetic materials. Diamagnetic materials ($\chi < 0$) generate a weak magnetic field in the direction opposed to an applied external magnetic field, locally decreasing the field strength. Paramagnetic materials ($\chi > 0$) generate a magnetic field in the direction equal to that of the applied field, locally increasing the field strength (adapted from [61]).

of the magnetic field lines, see Figure 1.2). This phenomenon is termed diamagnetism and holds for all substances that have a negative magnetic susceptibility ($\chi < 0$) [60]. Materials that generate a magnetization in the direction equal to that of the applied magnetic field (i.e. a concentration of the magnetic field lines, see Figure 1.2) are associated with paramagnetism or ferromagnetism [60]. This holds for substances that have a positive magnetic susceptibility ($\chi > 0$). Paramagnetic materials consist of atoms with an unpaired electron whose nonzero magnetic moments are randomly distributed in the absence of an external magnetic field, but align when placed in an external magnetic field producing a weak magnetic field that augments the applied field. All materials with susceptibility values of $0 < \chi < 0.01$ can be classified as paramagnetic. Ferromagnetic materials consist of permanent domains of electron spin magnetic moments, aligning with each other and producing a magnetic field, independent of the presence of an external magnetic field. Ferromagnetic materials have a susceptibility value of $\chi > 0.01$. Additionally, superparamagnetism is produced by contrast agents, consisting of ferromagnetic particles mixed into a background substance [60]. In the absence of an external field, thermal motion leads to vanishing magnetization. But, when placed in an external field, the particles can produce a strong magnetic field. As an indication, Table 1.1 presents the magnetic susceptibility values for a range of common materials.

1.4.2 Susceptibility artifacts

Materials with a magnetic susceptibility rather different from that of the surrounding tissue induce artifacts in MRI. This presents a challenge for the use of interventional instruments, frequently made of paramagnetic materials. A basic aspect related to MR imaging of interventional devices is that the material itself does not generate an MRI signal, due to the absence of hydrogen nuclei, so the object appears dark on MR images. Furthermore, the differences in magnetic susceptibilities between the object and its surrounding tissue cause strong perturbations of the static magnetic field [62]. The magnetic field perturbation causes changes in the resonance frequency, i.e. deviations from the Larmor frequency, resulting in artifacts in the MR images. These effects are also denoted as off-resonance effects. A variety of artifacts can be identified [64]. First, field variations cause large variations in the precession rate. This causes variations in the phase of the spins within a voxel, as the accumulated

Table 1.1 The magnetic susceptibility values (in ppm) for a range of common materials [62, 63].

Material	Susceptibility (ppm)
Gold	-34.00
Copper	-9.63
Water/soft tissue	-9.05
Air	0.36
Aluminum	20.70
Iridium	47.10
Titanium	182.00

phase, $\Delta\varphi$, is directly related to the frequency offset induced by the field perturbation, ΔB_0, via [60]:

$$\Delta\varphi = \gamma \Delta B_0 TE, \tag{1.2}$$

where γ is the gyromagnetic ratio and TE is the echo time. In gradient echo imaging, these local phase variations lead to intravoxel dephasing, which causes signal loss in the MR images. Second, the frequency variations harm a correct excitation and encoding in the slice direction and readout direction [64]. In 2D imaging, the process of frequency-selective slice selection can be influenced by the frequency variations. This can lead to a shift, curving or substantial distortion of the excited slice. Furthermore, it can cause the excitation of a slice with a decreased or increased slice thickness. In the readout direction (i.e. the frequency encoding direction), the frequency variations cause an incorrect frequency encoding, leading to mispositioning during image reconstruction. This is the reason for local image distortions, observed as signal loss and signal pile-up effects as well as geometric distortions. Third, the frequency variations can prevent a successful signal manipulation using pre-pulses such as used for fat suppression techniques relying on frequency-selective saturation of the spins at a frequency equal to the resonance frequency of fat [64]. In any case, the shape and severity of the susceptibility artifacts depend on the type of material (susceptibility), the orientation in the magnetic field, and the size and shape of the object. As an indication, Figure 1.3 demonstrates the artifacts induced by an HDR brachytherapy source for both a gradient echo sequence and a spin echo sequence.

In the past decades, research has been conducted on the quantification of magnetic field perturbations induced by magnetic susceptibility differences using analytical solutions as well as numerical analyses [65–69]. Furthermore, the knowledge about magnetic field perturbations has been implemented to study and simulate the induced susceptibility artifacts [70–78].

Besides the induced susceptibility artifacts, many metallic objects are unsafe for MRI. Ferromagnetic objects may experience strong forces and torques originating from the static magnetic field. A second risk is posed by the chance of radiofrequency (RF) induced heating. The induced susceptibility artifacts and the safety considerations reason the fact that mag-

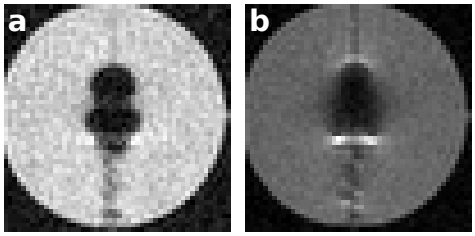

Figure 1.3 Examples of the artifacts induced by an HDR brachytherapy source in the MR images for **(a)** a gradient echo sequence, and **(b)** a spin echo sequence.

netic susceptibility plays an important role in MR imaging. It impacts the choice of materials for medical instruments used in MRI-guided interventions. Hence, in the development of MRI-guided HDR brachytherapy, magnetic susceptibility also plays an important role.

1.4.3 Tracking of interventional devices

A challenge to accurate device localization is posed by the fact that the magnetic susceptibility of most interventional devices induces artifacts in the MR images. In general, the artifacts are larger than the object itself and, in most cases, the artifact's center of mass does not indicate the exact position of the object. Considerable research has been conducted on visualization, localization or tracking of interventional devices and metal objects. The available techniques can be broadly divided in techniques for passive tracking and active tracking. Passive tracking techniques depend on variations in signal intensity due to the interventional device, and can be classified as either negative contrast or positive contrast. Passive tracking techniques with negative contrast rely on the appearance of a signal void or an artifact in the MR image [79, 80]. Passive tracking techniques with positive contrast rely on the generation of high signal intensities at the position of the device by modification of the MRI sequence or by image processing [81–86]. Positive contrast for catheter visualization can also be generated by filling the catheters with a gadolinium contrast agent [87, 88]. On the other hand, active tracking techniques are based on small receiver coils embedded into the device to generate a device signal for tracking, separately from the receiver array [89–91]. Additionally, wireless self-resonant coils can be used to locally enhance the signal intensity in the vicinity of the device, by inductive coupling, to visualize its position [92–94].

The passive tracking techniques predominantly provide visualization of the devices in the MR images, but lack accurate and/or fast localization. Active tracking techniques are inherently faster, but require additional equipment and supplemental hardware built into the interventional devices. Moreover, most active tracking techniques require an additional tracking sequence to be interleaved with the MR sequence to obtain anatomical images. Regarding the value of tracking techniques for real-time MRI guided HDR brachytherapy, fast and accurate localization are required. In this thesis, the artifacts induced by the HDR brachytherapy interventional devices are exploited for a fast and automatic localization.

1.5 Thesis outline

This thesis describes the development of a real-time MRI-guided HDR brachytherapy treatment. We propose a treatment set-up where the patient remains in the MR bore (and thus in the same position) during the complete process of source dwell position reconstruction, treatment planning and irradiation while MR images are acquired to guide the process. Real-time MRI guidance may provide an automatic detection of the source dwell positions as well as real-time treatment verification.

A treatment set-up which applies real-time MRI guided treatment verification involves positioning of the patient inside the MR bore at the moment of irradiation. **Chapter 2** presents a Monte Carlo study investigating the impact of the magnetic field of an MRI scanner on the dose distribution around an Ir-192 source. **Chapter 3** demonstrates a method for real-time source localization. We incorporate the existing knowledge about the field perturbation and the artifact induced by the HDR brachytherapy source to simulate the artifact and apply this for template matching to determine the source position in the MR images. The chapter focuses on obtaining high temporal and spatial resolutions. The source localization method can be applied for automatic detection of the source dwell positions and for real-time source localization during irradiation for treatment verification.To be able to put real-time source localization into practice, an MRI conditional afterloader is required. Therefore, **Chapter 4** presents the development and testing of an MR conditional afterloader. The chapter demonstrates the simultaneous functioning of an MR conditional afterloader and a 1.5 T MRI system in a phantom study. Lastly, for real-time source localization, not only the source position itself is important, but also the information of the patient anatomy is desired. **Chapter 5** focuses on the possibilities of the source localization method of Chapter 3 for clinically relevant MRI sequences which would simultaneously allow visualization of the anatomy. Hence, the chapter describes the simulation of the MRI artifacts induced by the HDR source (and a titanium needle) for a variety of MRI sequences: gradient echo, spin echo, balanced steady state free precession (bSSFP) and bSSFP with spectral attenuated inversion recovery (SPAIR) fat suppression. This generates flexibility in the choice of the MRI sequence for guidance of HDR brachytherapy.

Chapter 2

Monte Carlo study of the impact of a magnetic field on the dose distribution in MRI-guided HDR brachytherapy using Ir-192

The following chapter is based on:

Ellis Beld, Peter R. Seevinck, Jan J.W. Lagendijk, Max A. Viergever and Marinus A. Moerland.

Physics in Medicine and Biology (2016) 61: 6791–6807

Abstract

In the process of developing a robotic MRI-guided high-dose-rate (HDR) prostate brachytherapy treatment, the influence of the MRI scanner's magnetic field on the dose distribution needs to be investigated. A magnetic field causes deflection of electrons in the plane perpendicular to the magnetic field, and it leads to less lateral scattering along the direction parallel with the magnetic field. Monte Carlo simulations were carried out to determine the influence of the magnetic field on the electron behavior and on the total dose distribution around an Ir-192 source. Furthermore, the influence of air pockets being present near the source was studied. The Monte Carlo package Geant4 was utilized for the simulations. The simulated geometries consisted of a simplified point source inside a water phantom. Magnetic field strengths of 0 T, 1.5 T, 3 T, and 7 T were considered. The simulation results demonstrated that the dose distribution was nearly unaffected by the magnetic field, for all investigated magnetic field strengths. Evidence was found that, from a dose perspective, the HDR prostate brachytherapy treatment using Ir-192 can be performed safely inside the MRI scanner. No need was found to account for the magnetic field during treatment planning. Nevertheless, the presence of air pockets in close vicinity of the source, particularly along the direction parallel with the magnetic field, appeared to be an important point for consideration.

2.1 Introduction

High-dose-rate (HDR) brachytherapy has been proven to be an effective treatment for prostate cancer [4, 5]. Recently, single-fraction HDR brachytherapy has been investigated as monotherapy and it may become the treatment of choice for low and intermediate-risk disease [16]. In single fraction HDR brachytherapy, a high dose is given in one fraction, making image guidance of great importance for safe dose delivery. Magnetic resonance imaging (MRI) is the favorable imaging modality, as it enables visualization of the tumor and surrounding tissues as well as detection of the needle and source positions [20, 21, 83]. A robotic fully MRI-guided HDR prostate brachytherapy treatment at 1.5 T is in development at our institution [95], among others aiming at MRI guidance during dose delivery. However, the procedure of MRI guidance involves a patient's body being placed inside the MRI bore, i.e. in a strong magnetic field, at the moment of radiation delivery. This introduces the chance of interaction between particles involved in the irradiation process and the magnetic field.

The combination of radiation therapy with a magnetic field has been studied by several groups, for different purposes. Fundamental theories describe that photons travel unaffected in a magnetic field and that the covered trajectories of charged particles (e.g. secondary electrons) are influenced by the Lorentz force. Already in 1950, the employment of a longitudinal magnetic field (parallel with the radiation) was explored for direct-electron-beam therapy to reduce lateral scattering of secondary electrons [96]. The reduced lateral scattering results from restriction of the scattered electron beam to helical trajectories along the magnetic field direction. Furthermore, research was conducted on the application of longitudinal and transverse magnetic fields in both electron beam therapy and external beam photon radiotherapy to optimize dose distributions [97–103].

In the current situation of the employment of MRI for radiotherapy guidance, the magnetic field causes unintentional modifications of the radiotherapy dose distribution. The impact of an external magnetic field on the dose distribution was investigated for transverse irradiation [104–106], in the development of a radiotherapy treatment system with an integrated MRI system (an MR-linac) [107, 108]. Two main dose effects were described: an asymmetrical point spread kernel and the electron return effect (ERE). The asymmetrical point spread kernel leads to a reduced build-up distance due to deflection of secondary electrons. The ERE concerns secondary electrons leaving tissue at a tissue-air boundary to be forced back into the tissue due to the Lorentz force, causing an increased dose locally. The degree of these effects depends on the magnetic field strength and the electromagnetic particles' energies involved. Besides, the effect of a magnetic field on the dose distribution was investigated for a longitudinal field MR-linac system, where irradiation is performed along the direction parallel with the magnetic field [109, 110]. In this case, highly increased skin doses were reported, as the magnetic field forces contaminated electrons to travel directly towards a patient's skin, allowing no lateral spread [110].

For HDR brachytherapy (using an Ir-192 source) inside the MRI bore, two main distinctions can be found in comparison to the case of an MR-linac. First, the irradiation direction is nearly isotropic, instead of merely perpendicular to or parallel with the magnetic field.

Table 2.1 The range of electrons in air and in water [111], for several electron energies. The last three columns show the radius of an electron trajectory when traveling in vacuum and in a magnetic field (see section 2.6 (Appendix) for the equations for calculation of the values), for magnetic field strengths of 1.5 T, 3 T and 7 T.

Electron energy	Range in air	Range in water	Trajectory radius in vacuum (mm)		
(keV)	(mm)	(mm)	B = 1.5 T	B = 3 T	B = 7 T
50	38	0.04	0.5	0.3	0.1
100	126	0.1	0.7	0.4	0.2
200	393	0.4	1.1	0.6	0.2
300	737	0.8	1.4	0.7	0.3
400	1127	1.3	1.7	0.8	0.4
500	1544	1.8	1.9	1.0	0.4
1000	3802	4.4	3.2	1.6	0.7

Second, the initial photon energies, and thus also the electron energies, involved in HDR brachytherapy are lower. Consequently, a direct translation from the findings for external beam radiotherapy to the situation of an HDR brachytherapy procedure inside the MRI bore is impossible. Before the HDR brachytherapy treatment can be carried out inside the MRI bore, research on the safety of the procedure is necessary. Therefore, this study focusses on the influence of an external magnetic field on the dose distribution around an HDR brachytherapy source.

When ignoring scattering, three types of response to the magnetic field may be expected for the secondary electrons, depending on the angle of their path with respect to the magnetic field direction, due to the Lorentz force. When an electron is directed perpendicular to the magnetic field, its trajectory will bend due to the Lorentz force. On the other hand, when the electron travels parallel or antiparallel with the magnetic field, it will remain traveling along this line. Moreover, when the electron path makes a different angle with the magnetic field lines, the electron will move along a helical path towards the direction (either positive or negative) in which the magnetic field lines point. This predicts the dose distribution in a magnetic field to become more narrow in the plane perpendicular to the magnetic field direction and broader at different angulations, particularly parallel to the magnetic field direction.

For HDR prostate brachytherapy, the anatomical position of the prostate close to the rectum leads to a reasonable chance of the presence of an air pocket near the source. Hence, the ERE can have an impact in these regions. The ERE occurs when electrons, entering the air pocket, follow a path with a radius smaller than the air pocket radius. Table 2.1 presents the range of electrons in air as well as in water [111] and the trajectory radius of electrons traveling in a magnetic field (see section 2.6 (Appendix) for the equations for calculation of the values) for varying electron energies. The ratios between the trajectory radius and the range of electrons in either air or water determine that the impact of the magnetic field on the electron trajectory will be larger in air than in water, due to the lower density of the

matter. Furthermore, the trajectory radii indicate that the ERE is probable to occur in the surroundings of air pockets, which can be as small as a few millimeters. Besides, in the direction parallel with the magnetic field lines, more electrons will travel presumably in the forward direction inside the air pocket (either along a helical path or straight). This gives rise to the possibility of a changed dose at the opposite side of an air pocket in the longitudinal direction, in the case of an external magnetic field.

The focus of this paper is to explore to what extent a magnetic field influences the dose distribution around an HDR brachytherapy source (Ir-192) placed in an external magnetic field. This is conducted by Monte Carlo simulations. The magnetic field strengths of the common clinical MRI systems (1.5 T and 3 T) and an ultra-high field MRI system (7 T), anticipating on possible future developments, are considered. In order to provide a general insight into the impact of the magnetic field on the secondary electrons, the paper starts with a characterization of the secondary electrons and their distribution in a magnetic field. Next, two main aspects are covered. The first is an evaluation of the impact on the general dose distribution around an HDR brachytherapy source. The second aspect is the impact of the magnetic field when air pockets are present in close proximity of the source. The overall aims were to investigate if the HDR brachytherapy treatment can be safely performed inside the MRI bore and to determine if treatment planning needs to be adapted to take into account the magnetic field.

2.2 Methods

2.2.1 Monte Carlo simulations

All Monte Carlo simulations were performed using the Monte Carlo package Geant4 v10.0 [112, 113]. This is an open source toolkit that provides the simulation of electromagnetic interactions of particles with matter. The Geant4 code has been thoroughly validated and employed in many areas, including the field of medical physics [114, 115]. The package has been applied extensively to Monte Carlo simulations related to brachytherapy [116–118]. Moreover, Geant4 permits reliable computation of electromagnetic radiation trajectories in the presence of a magnetic field [119].

In all simulations, the low energy Livermore electromagnetic physics package ('EmLivermorePhysics') was incorporated. This model contains photons (included interactions: Compton scattering, Rayleigh scattering, gamma conversion, and photoelectric effect) and electrons (included interactions: ionization and Bremsstrahlung). A CutValue of 1 μm was utilized, leading to a production threshold of 250 eV for photons and electrons in water and air (i.e. below 250 eV no secondary electrons or photons are generated) and a range cut of 1 μm (i.e. particles with an energy below the threshold energy stop after traveling 1 μm). The maximum step size was set to 0.2 mm, being smaller than the voxel size to secure energy deposition at the correct location. A classical fourth-order Runge-Kutta stepper ('ClassicalRK4') was applied to calculate the trajectories of charged particles in a magnetic field. The embedded

DeltaChord value was 0.05 mm, which is the maximum distance between a curved trajectory and the chord segments approximating the curved path.

A three-dimensional Cartesian coordinate system was defined, where the magnetic field lines were oriented towards the positive z-axis. In all cases, simulations were repeated with magnetic field strengths of respectively B = 0 T, B = 1.5 T, B = 3 T, and B = 7 T.

Statistical accuracy

The statistical accuracy of the simulations was determined by splitting the simulations into N independent batches, and then calculating the statistical uncertainty, ε, of the energy deposition per voxel as follows:

$$\varepsilon = \frac{\sigma}{\sqrt{N} \cdot \bar{X}}, \tag{2.1}$$

where σ is the standard deviation of the values in the voxel, over the N statistical batches, and $\bar{X}$ is the mean over all N values of the voxel.

2.2.2 Investigated cases

Electron behavior

At first, a study on the secondary electron energies involved in HDR brachytherapy (using Ir-192) was carried out. This was realized by running a simulation as described in section 2.2.2 (but with $1 \cdot 10^8$ photons simulated), and recording the energies of all secondary electrons generated. The electron energies making a relevant contribution to energy deposition were determined. The maximum relevant energy was selected, and used as input into the simulations of the electron behavior.

Monte Carlo simulations of electrons traveling in a magnetic field were performed to gain insight into the order of the field's influence on the electron distribution. A 'worst-case scenario' of the maximum possible impact was sketched, taking the maximum relevant secondary electron energy (selected from the study described above) as the initial primary particle energy. The primary particles were generated by a point source producing electrons in a single direction. Two distinct initial directions of the electrons were considered: (I) parallel with the magnetic field, along the positive z-axis, and (II) perpendicular to the magnetic field, along the positive x-axis. A number of $1{\cdot}10^8$ primary electrons were generated. A phantom was simulated, consisting of a homogeneous box of water with dimensions of $1.99{\times}1.99{\times}1.99$ cm^3. The electron point source was placed in the center of the phantom.

The energy deposition was calculated using a scoring grid that covered the phantom. This grid consisted of 199 bins in all three dimensions, such that the source was positioned exactly in the center of one scoring voxel, resulting in scoring voxels of $0.1{\times}0.1{\times}0.1$ mm^3.

Dose distribution

The influence of the magnetic field on the total dose distribution around an Ir-192 source in a magnetic field was investigated by adopting an ideal point source as simplification of the source geometry. This was feasible since the effects due to the cylindrical source geometry are irrelevant to addressing the basic impact of an external magnetic field on the radiation transmission.

A homogeneous water phantom was simulated as a box with dimensions equal to $9.95 \times 9.95 \times 9.95$ cm^3, holding the source at the exact center. Regarding the Ir-192 energy spectrum, the electrons originating from β^- decay were assumed to be negligible [120]. The energy spectrum assigned to the primary particles was the Ir-192 photon spectrum of the US National Nuclear Data Center [121], which was normalized to an intensity of 100%, see Table 2.2. The General Particle Source was included to generate the primary photons, utilizing an isotropic distribution. The number of primary photons was $4 \cdot 10^9$ (split up as $40 \times 1 \cdot 10^8$), with a statistical uncertainty of $1.5 \pm 0.2\%$ at 1.0 cm and $6.7 \pm 0.8\%$ at 4.5 cm distance from the source.

The primary photons cause cascades of electrons depositing energy along their paths. The resulting dose deposition (i.e. energy deposition) was scored on a grid with dimensions equal to the phantom size. The scoring grid consisted of 199 bins in all three dimensions, such that one scoring voxel contained the source in its center. The resulting scoring voxel size was $0.5 \times 0.5 \times 0.5$ mm^3.

Air pockets

In the simulations of the case with an air pocket present close to the Ir-192 source, the parameters and geometry were equal to those mentioned in section 2.2.2, except for the addition of an air pocket. The air pocket was defined in the water phantom as a cube (to prevent partial volume effects) of air with dimensions of $30 \times 30 \times 30$ mm^3, regarded as a realistic dimension for an air pocket appearing in the rectum. Two distinct positions of the air pocket with respect to the source position were considered: (I) at a distance of 3.25 mm along the central x-axis in the direction perpendicular to the magnetic field, to study the ERE, and (II) at a distance of 3.25 mm along the central z-axis in the direction parallel with the magnetic field, to study the effect of a longitudinal magnetic field. Under these circumstances, partial volume effects were prevented, as the air pocket's cubical shape and the distance of 3.25 mm between the source and the air pocket ensure an overlap of the air pocket boundaries with voxel boundaries. Besides, the case where the air pocket was positioned along the longitudinal direction was studied more extensively for a magnetic field strength of 1.5 T, by varying the distance between air pocket and source (10.25 mm), and by varying the air pocket size (5 mm, 10 mm, 15 mm, 20 mm, 25 mm isotropically). The number of primary photons was $2 \cdot 10^9$ (split up as $20 \times 1 \cdot 10^8$), with a statistical uncertainty of $2.2 \pm 0.4\%$ at 1.0 cm and $9.4 \pm 1.6\%$ at 4.5 cm distance from the source.

Table 2.2 The photon energy spectrum of Ir-192 [121] used for the Monte Carlo simulations. The spectrum was normalized to an intensity of 100%.

Energy (keV)	Intensity (%)
110.33	0.0059
136.39	0.0917
176.98	0.0020
201.31	0.2171
205.79	1.5254
280.27	0.0037
283.27	0.1226
295.96	13.2321
308.46	13.6875
316.51	38.1910
329.09	0.0080
374.49	0.3350
416.47	0.3088
420.52	0.0318
468.07	22.0474
484.58	1.4701
485.46	0.0022
489.06	0.2019
588.58	2.0840
593.63	0.0194
599.41	0.0018
604.41	3.7864
612.46	2.4612
703.78	0.0024
765.83	0.0006
884.54	0.1346
1061.49	0.0245
1089.96	0.0005
1378.50	0.0006

2.2.3 Analysis

The analysis of the simulation results was performed in Matlab (The MathWorks, Natick, Massachusetts, United States). In the analysis of the electron behavior, the energy depositions were scaled as percentage of half the maximum deposited energy of the case without magnetic field (i.e. B = 0 T). The energy distributions for the cases with distinct initial electron directions were compared, as well as those for the cases with different magnetic field strengths.

In order to analyze the impact on the total dose distribution, the dose depositions for the different magnetic field strengths were compared both in the plane parallel with the magnetic field and in the perpendicular plane. The dose depositions were normalized to the average dose at 10 mm distance from the source (reference distance recommended by the AAPM task group 43 [122] in the case without magnetic field, which was defined as 100% of the dose. The steep dose gradient around the source, obeying the inverse square law, hampers a simple comparison of the different dose depositions over the total area. Therefore, the dose depositions with and without magnetic field were analyzed by subtracting the two, and then quantifying the differences as: (I) a dose percentage, and (II) a percentage of the local dose without magnetic field. Furthermore, comparisons were made between the isodose contours with and without magnetic field, considering the isodose contours for 5, 10, 30, 100, 300, and 1000 % of the normalized dose.

In the situations with the presence of an air pocket, the dose depositions were analyzed through a plot of the normalized dose along the central axis along which the air pocket was positioned (either the x or z-axis). Comparisons were made between the dose depositions for the cases with distinct magnetic field strengths and the case without air pocket and B = 0 T. Moreover, comparisons were made between cases where the air pocket distance and the air pocket size were varied.

2.3 Results

2.3.1 Electron behavior

The spectrum of secondary electron energies, obtained from a simulation of $1{\cdot}10^8$ primary photons of an Ir-192 source, is shown in Figure 2.1a. The graph demonstrates that mainly low-energy electrons are involved in the irradiation process, showing several peaks up to an energy of 432 keV. The energy fluence spectrum, given in Figure 2.1b, represents the contributions of the secondary electron energies to the energy deposition, as the fluence spectrum is defined as the energy spectrum multiplied by the corresponding energy value of each bin. Based on both spectra, an energy of 432 keV was considered as the highest electron energy relevant to the contribution to energy transfer.

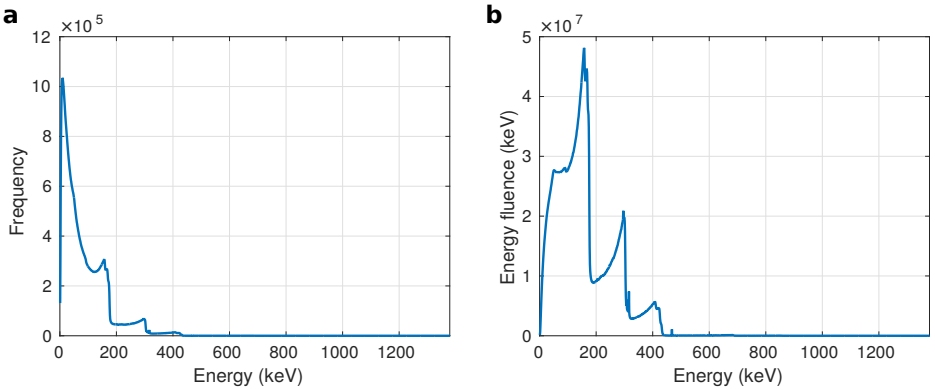

Figure 2.1 (a) The energy spectrum of secondary electrons, obtained from a simulation of $1{\cdot}10^8$ primary photons of an Ir-192 source. **(b)** The energy fluence spectrum of secondary electrons (i.e. the energy spectrum of *a* multiplied by the corresponding energy values).

Insight into the impact of the magnetic field was obtained by Monte Carlo simulation of electrons, generated either parallel with or perpendicular to the magnetic field direction, resulting in the energy depositions presented in Figure 2.2 (with logarithmic scaling). The figure illustrates the effect of the magnetic field on the distribution of electrons traveling in a magnetic field. In the situation of electrons traveling parallel with the magnetic field (Figure 2.2a), the amount of energy deposited along the z-direction was slightly higher in the cases with higher magnetic field strengths. Conversely, in the situation of electrons traveling perpendicular to the magnetic field (Figure 2.2b), a clear deflection pattern was observed for the higher field strengths. Besides, the range over which the energy deposited was decreased when a magnetic field was present, particularly noticeable in the case of B = 7 T.

The energy depositions presented in Figure 2.2 apply to an initial electron energy of 432 keV, representing a 'worst-case scenario' of the electron behavior. Electrons with higher energies have a negligible contribution to energy deposition, and electrons with lower energies experience a reduced impact of the magnetic field as their average range is smaller. Looking at the overall effects, the results demonstrate that the electron behavior was influenced by the magnetic field only at a small scale (submillimeter). Most of the energy transfer took place very close to the point of origin of the electrons, indicating that the actual influence of the magnetic field on the total dose distribution might be minimal.

2.3.2 Dose distribution

The differences between the dose depositions with and without magnetic field, around an ideal point source, are displayed in Figure 2.3. Negative differences indicate a decreased dose due to the magnetic field, whereas positive differences indicate an increased dose. When the source was placed in an external magnetic field, the dose was anisotropically distributed,

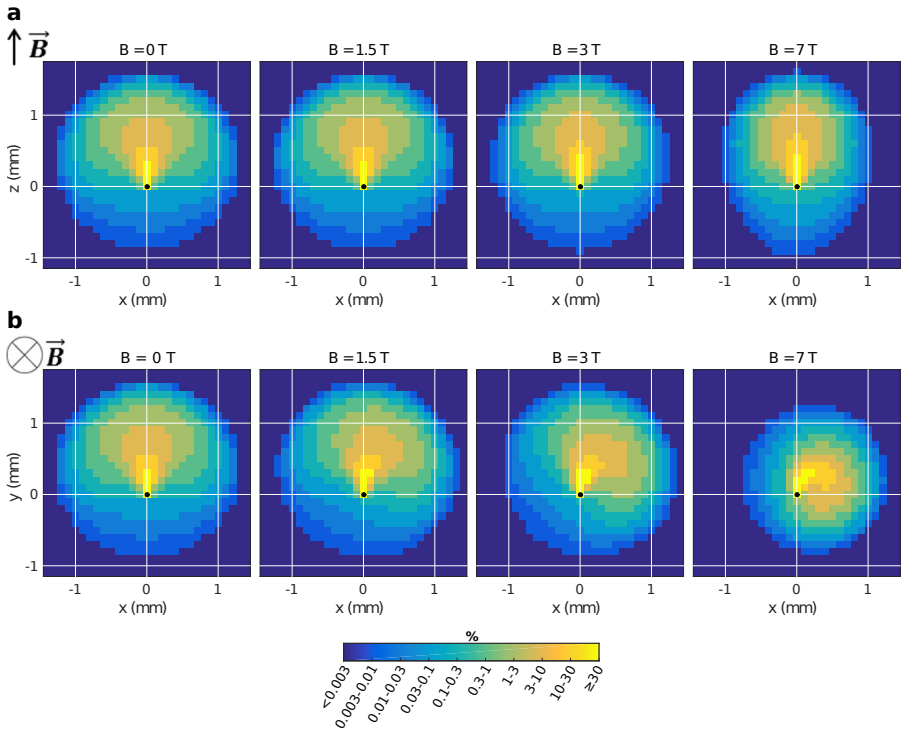

Figure 2.2 The energy deposition in a water phantom obtained from a monoenergetic (432 keV) point source producing electrons in a single direction, **(a)** parallel with the magnetic field, and **(b)** perpendicular to the magnetic field, for field strengths of B = 0 T, B = 1.5 T, B = 3 T, and B = 7 T (from left to right), illustrating the impact of the magnetic field on traveling electrons. The energy deposition is shown on a logarithmic scale, as a percentage of half the maximum deposited energy in the case without magnetic field (i.e. B = 0 T).

in contrast to the case without magnetic field. When regarding the differences as a dose percentage (left and middle columns in Figure 2.3), they were apparent only in the direct vicinity of the source, and more striking with higher magnetic field strengths. The central region, in the direct vicinity of the source, showed a dose increase due to the magnetic field. In the longitudinal plane, an increased dose was observed along the direction of the magnetic field lines. In contrast, a decrease was found in the transverse plane.

The left and middle columns of Figure 2.3 might suggest substantial differences between the dose distributions with and without magnetic field. However, these differences appeared merely around the center, very close to the source, at locations that in any case receive an overdosage. Moreover, when considered as a percentage of the local dose without magnetic field (right column in Figure 2.3), the absolute differences turned out to be well below 4% for B = 1.5 T and B = 3 T. In the case of a magnetic field strength of B = 7 T, the differences were considerably larger: an increase of up to 12% was found along the line through the center, parallel with the magnetic field direction. In the central plane perpendicular to the magnetic field, decreased values of around 4% were observed. Clearly, the higher differences were found only within 3 mm around the source. At a distance of 10 mm from the source, the absolute differences were around the statistical noise level ($\approx 1.7 \pm 1.3\%$) for all three magnetic field strengths (1.5 T, 3 T and 7 T). At positions beyond 10 mm from the source, differences decreased rapidly with increasing distance.

Figure 2.4 demonstrates that distinctions could hardly be noticed between the isodose contours without and with magnetic field, for all magnetic field strengths (1.5 T, 3 T and 7 T). Despite the larger differences found in the case of B = 7 T, no considerable deviations of the isodose contours were observed. Thus, as already expected from the electron behavior shown in Figure 2.2, the secondary electrons affected the dose distribution only on a local scale. Hence, the inverse square law for the distribution of primary photons dominated the distribution of dose around the source, regardless of the presence of a magnetic field.

2.3.3 Air pockets

In the situation that an air pocket was present close to the source in the transverse plane, the dose distribution was slightly affected by the ERE, see Figure 2.5. In more detail, electrons that entered the air region followed deflected paths and were forced to travel back into the water region, causing an increased dose in the water area of the water-air transition. However, this was a rather modest effect, occurring along a region of only one voxel in depth. As a result, the ERE could be perceived as a negligible effect.

In contrast, a more apparent effect was noticed in the situation that the air pocket was located along the longitudinal direction. Dose increases were observed in the water region of the air-water transition at the opposite side of the air pocket, see Figure 2.6a-b. These increases were found for all magnetic field strengths studied, showing slightly higher peak values with increasing field strengths. One remarkable feature, accounting for mentioned dose increases, is that the graphs presented a nearly constant dose deposition within the air pocket zone due

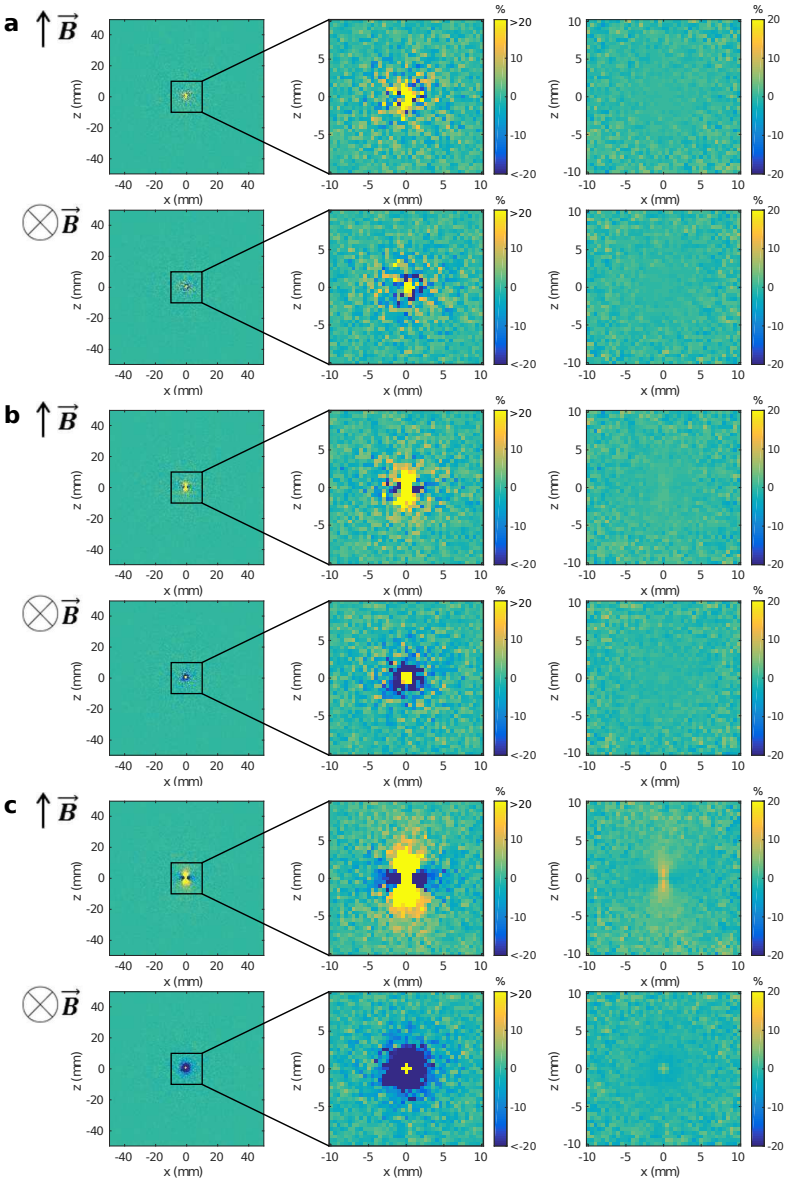

Figure 2.3 The subtractions of the dose depositions with and without magnetic field (dose with magnetic field minus dose without magnetic field), for field strengths of **(a)** 1.5 T, **(b)** 3 T and **(c)** 7 T. The central plane parallel with the magnetic field (upper rows) and the central plane perpendicular to the magnetic field (lower rows) are presented. The dose differences are provided as a percentage of the dose at 10 mm (left and middle column), where the middle column is a zoomed view, and as a percentage of the local dose (right column).

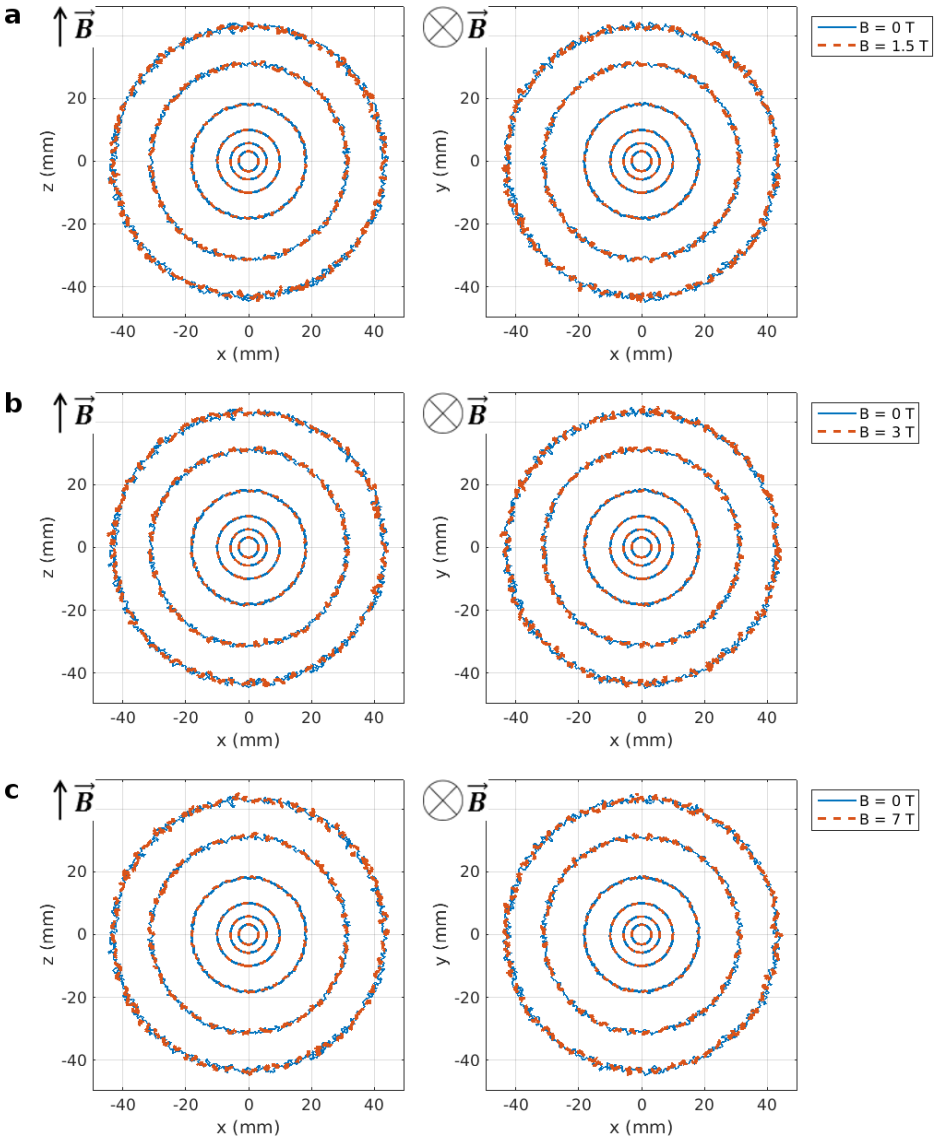

Figure 2.4 The isodose contours without magnetic field (B = 0 T) and with magnetic field, with field strengths of **(a)** B = 1.5 T, **(b)** B = 3 T and **(c)** B = 7 T, in the planes parallel with (left) and perpendicular to (right) the external magnetic field. The isodose contours represent 5, 10, 30, 100, 300, and 1000 % of the normalized dose (from the outside in).

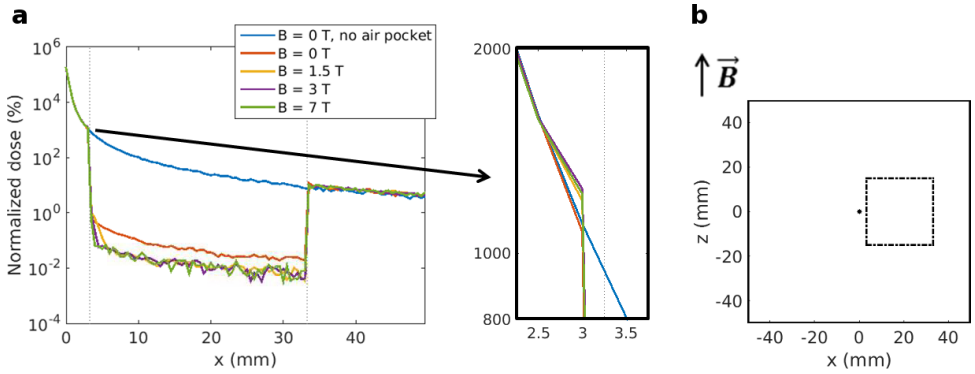

Figure 2.5 (a) The normalized dose profile along the central axis perpendicular to $\vec{B}$ (the x-axis), for the case without air pocket and magnetic field (blue graph) and for the cases with an air pocket present (see b) for all investigated magnetic field strengths, on a logarithmic scale, including a zoomed view of the point at the water-air transition (at x = 3.25 mm) indicated by the black arrow. **(b)** The air pocket position, shown in the central plane of the phantom and indicated by the dotted lines (from x = 3.25 mm up to x = 33.25 mm), with air pocket dimensions of 30×30×30 mm^3.

to the magnetic field, instead of the characteristic quadratic behavior demonstrated in water. Under influence of the magnetic field and provided the substantially lower electron density in air, electrons that entered the air pocket were forced to travel along a helical path in the direction parallel with the magnetic field, finally depositing their energy in the water area at the opposite side of the air pocket. Thus, electrons that otherwise would have been distributed in all directions and subjected to substantially more scattering were now transported in equal directions, predominantly to the opposite side of the air pocket, causing a dose increase there. Consequently, a lower dose was observed at the lateral air-water interfaces.

Additionally, Figure 2.6c-d demonstrates that the dimensions of the air pocket as well as the distance between source and air pocket have a substantial influence on the peak height of the dose increase. In the situation with the air pocket located close to the source (i.e. 3 mm) and a relatively large air pocket size (i.e. 30 mm isotropically), the dose increase due to the magnetic field was considerably high with respect to the situation of B = 0 T (see the yellow graph in Figure 2.6c). A change of one of the two considered parameters, either positioning of the air pocket at a larger distance or a decrease of air pocket dimensions, led to less dose increase with respect to the case of B = 0 T (see the green and purple graphs respectively in Figure 2.6c), although the effect is still noteworthy. Furthermore, the black marks in Figure 2.6c show the peak heights for all cases where the air pocket size was varied. The figure demonstrates that the dose at the near side of the air pocket reflects the amount of available electrons, which decreases gradually along the air pocket and then determines the peak height after deposition at the opposite side, whereas the expected dose decreases considerably faster over distance (in accordance with the inverse square law). The significant dose increases indicate that the presence of air pockets near the source should not be ignored.

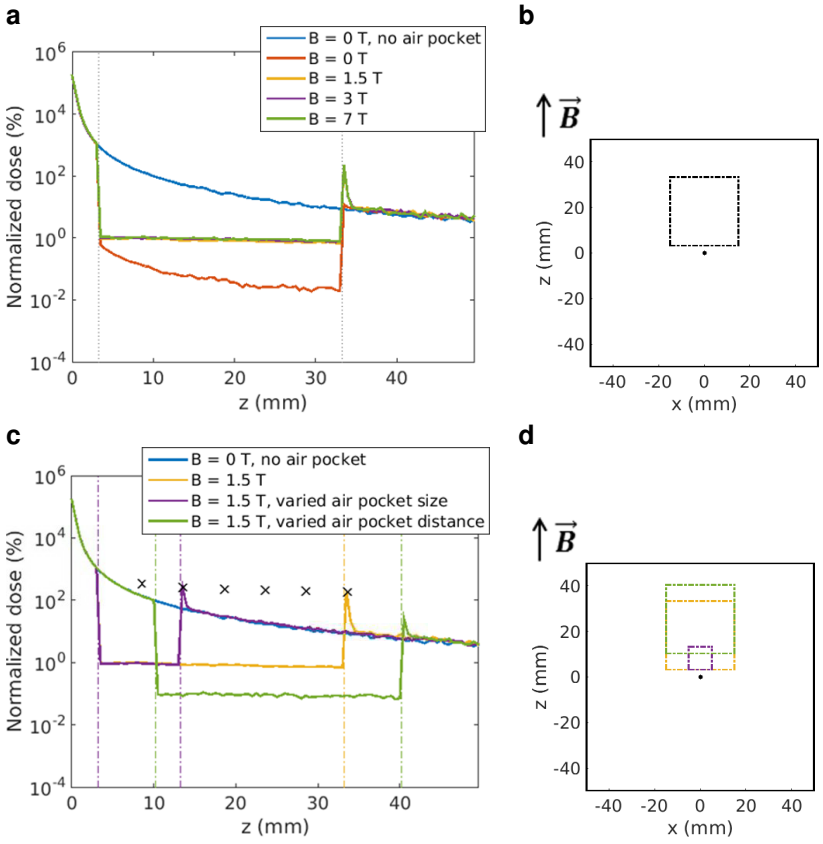

Figure 2.6 The normalized dose profiles (a and c) along the central axis parallel with $\vec{B}$ (the z-axis), on a logarithmic scale. The blue graphs represent the case where neither the air pocket nor the magnetic field were present. Furthermore, **(a)** presents the dose for the cases with an air pocket present for all investigated magnetic field strengths. The position of the air pocket is shown in the central plane of the phantom in **(b)**, indicated by the dotted lines (from z = 3.25 mm up to z = 33.25 mm), with air pocket dimensions of 30×30×30 mm^3. The graphs in **(c)** show the dose profiles for the case of a cubic air pocket with size 30 mm at z = 3.25 mm at 1.5 T (yellow), and for the cases where the air pocket size was varied, i.e. 10 mm cubic (purple), and where the air pocket distance was varied, i.e. 10.25 mm (green). A schematic representation of these air pocket positions and dimensions is given in the central plane of the phantom in **(d)**, with colors corresponding to the graphs in **(c)**. The black marks in **(c)** represent the peak heights for all cases where the air pocket size was varied (5 mm, 10 mm, 15 mm, 20 mm, 25 mm, and 30 mm cubic respectively).

2.4 Discussion

The results of the Monte Carlo simulations provided insight into the effect of a magnetic field on the dose distribution around an Ir-192 HDR brachytherapy source. The magnetic field caused the electron distribution to be narrower and extended in the longitudinal direction and deflected in the transverse plane. However, the results supported that these electron effects occur on a submillimeter scale. This was also confirmed by the simulated total dose distributions around a point source with and without magnetic field; the isodose contours were virtually unaffected by the magnetic field. The dose distributions proved that the inverse square law for the distribution of photons dominated the distribution of dose in a water phantom, regardless of the presence of a magnetic field. This outcome is essential to the interpretation of the impact of the magnetic field as a marginal effect in a clinical situation. Besides this encouraging outcome, the results revealed one topic attention needs to be drawn to: the presence of an air pocket in close proximity to the source. When an air pocket is present near the source along the longitudinal direction and has considerable dimensions, a substantial dose increase can be expected in the tissue area at the opposite side of the air pocket, as proven by the simulations. This fact highlights the necessity of paying attention to the chance of air pockets appearing near the source during treatment.

With regard to the HDR brachytherapy treatment for prostate cancer, the data provided evidence for the fact that the magnetic field does not seriously affect the dose distribution. The minimal impact of the magnetic field for the simulated point source implies that likewise the magnetic field has a negligible impact in the case of the actual source geometry. Consequently, no further simulations were needed to explore the effects for the situation of a cylindrical source geometry. For application in prostate cancer treatment, minimal risks are expected due to air pockets, since, for anatomical reasons, air pockets are highly improbable to appear along the longitudinal direction in the immediate vicinity of the prostate. Due to the fact that the rectum is located posterior to the prostate, air pockets will presumably appear in the transverse direction with respect to the source, leaving the dose distribution roughly unaffected. For a translation of the simulation results to a clinical situation, this indicates that the HDR prostate brachytherapy treatment can be safely performed inside the MRI bore.

When considering MRI-guided HDR brachytherapy for the treatment of a different type of cancer, rather than prostate cancer as in this study, careful attention should be paid to the chances of air pockets appearing close to the source, particularly along the longitudinal direction. A decision can be made on the impact on the dose distribution and the safety of the specific treatment, based on the distance between intended source positions and potential air pockets.

The research demonstrated here was conducted specifically on the usage of an Ir-192 source. When considering HDR brachytherapy with employment of a different type of HDR source, for instance cobalt (Co-60) or cesium (Cs-137), the strength of the magnetic field's effects on the radiation transport will be different due to the particular energies involved with decay of the radioactive isotopes. Co-60 and Cs-137 sources produce photons with energies of respectively 1.17/1.33 MeV and 0.66 MeV, clearly higher than the average photon energy of

an Ir-192 source (i.e. 0.37 MeV). The higher photon energies correspond with an increased secondary electron range, consequently raising the possibility of deviation from the original electron paths. This suggests that the magnetic field has an increased impact when applying either a Co-60 or a Cs-137 source, with respect to the case of the Ir-192 source investigated here. Consequently, when considering employment of a different radioactive isotope for treatment inside an MRI bore, more research must be conducted on the impact of the magnetic field for that specific type of HDR source.

2.5 Conclusion

This paper presents a Monte Carlo study on the impact of an external magnetic field on the dose distribution of an Ir-192 source, for the intended application of MRI-guided HDR prostate brachytherapy. The simulation results demonstrated no considerable influence of the magnetic field on the general dose distribution (differences less than or around the level of the statistical error, i.e. around 1.7% at 10 mm), for the investigated magnetic field strengths of 1.5 T, 3 T and 7 T. The distribution of photons, in accordance with the inverse square law, dominates the total dose distribution. The conclusion for the application of the HDR prostate brachytherapy treatment inside the MRI scanner is twofold. First, from a dose perspective, the procedure can be performed safely inside the MRI scanner. Second, the study proved no need to adapt treatment planning to take into account the magnetic field. Nevertheless, careful attention should be paid to the appearance of air pockets near the source.

2.6 Appendix. Electron trajectory radius in the presence of a magnetic field

An electron traveling in a magnetic field describes a helical path. The electron trajectory radius r is described by the following equation, taking the relativistic electron energy into account [123]:

$$r = \frac{(E_0 + E_k)\sqrt{1 - \left(\frac{E_0}{E_0 + E_k}\right)^2}}{Bqc}, \tag{2.2}$$

where E_0 is the electron rest mass energy (511 keV), E_k is the electron kinetic energy, B is the magnetic field strength, q is the electron charge ($1.6 \cdot 10^{-19}$ C) and c is the speed of light ($3.0 \cdot 10^8$ m/s).

Acknowledgments

This research was funded by the Eurostars Programme, ITEA3, project name: System of Real-Time Systems (SoRTS), project number: 12026.

Chapter 3

MR-based source localization for MR-guided HDR brachytherapy

The following chapter is based on:

Ellis Beld, Marinus A. Moerland, Frank Zijlstra, Max A. Viergever, Jan J.W. Lagendijk and Peter R. Seevinck

Physics in Medicine and Biology (2018) 63: 085002

Abstract

For the purpose of MR-guided high-dose-rate (HDR) brachytherapy, a method for real-time localization of an HDR brachytherapy source was developed, which requires high spatial and temporal resolutions. MR-based localization of an HDR source serves two main aims. First, it enables real-time treatment verification by determination of the HDR source positions during treatment. Second, when using a dummy source, MR-based source localization provides an automatic detection of the source dwell positions after catheter insertion, allowing elimination of the catheter reconstruction procedure. Localization of the HDR source was conducted by simulation of the MR artifacts, followed by a phase correlation localization algorithm applied to the MR images and the simulated images, to determine the position of the HDR source in the MR images. To increase the temporal resolution of the MR acquisition, the spatial resolution was decreased, and a subpixel localization operation was introduced. Furthermore, parallel imaging (sensitivity encoding) was applied to further decrease the MR scan time. The localization method was validated by a comparison with CT, and the accuracy and precision were investigated. The results demonstrated that the described method could be used to determine the HDR source position with a high accuracy (0.4-0.6 mm) and a high precision ($\leq$0.1 mm), at high temporal resolutions (0.15-1.2 s per slice). This would enable real-time treatment verification as well as an automatic detection of the source dwell positions.

3.1 Introduction

Magnetic resonance imaging (MRI) is the preferred imaging modality for guidance of high-dose-rate (HDR) brachytherapy, as it enables visualization of the anatomy with a high soft tissue contrast, as well as detection of interventional devices (e.g., brachytherapy catheters) [20–22]. In some applications, such as HDR prostate brachytherapy, a high dose is delivered in a single fraction (up to 19 Gy), while trying to minimize the dose to organs at risk. Therefore, advanced image guidance is necessary for safe and precise dose delivery [18]. A fully MRI-guided robotic HDR prostate brachytherapy treatment at 1.5 T is in development at our institution [95], which includes real-time MRI-guided treatment verification. Hence, this paper focuses on the development of a method for real-time HDR brachytherapy source tracking using MRI.

By developing an automatic MRI based HDR source localization method, two aims can be achieved for both the current and the future robotic treatment. First, it provides real-time HDR source dwell position verification during the treatment, enabling a more detailed verification of the delivered dose in real time. Second, with the employment of a dummy source, the source localization can be conducted to automatically detect the source dwell positions after catheter insertion. This may replace the currently applied manual catheter reconstruction procedure, improving the workflow and avoiding reconstruction errors.

In recent years, considerable research has been conducted on techniques for either guidance or verification of HDR brachytherapy treatments, e.g., in vivo dosimetry with detectors [124, 125], fluoroscopy [126], electromagnetic tracking (EMT) [56–58] or fiber Bragg gratings (FBG)-based sensing [59]. These techniques have their limitations. For example, in the case of in vivo dosimetry, the dose is measured only in single points instead of a 3D volume and, in all mentioned techniques, a registration is needed with an anatomical dataset obtained using an additional imaging modality (ultrasound imaging, CT or MRI). Due to their limitations, these methods are currently not commercially available and, therefore, not clinically applied [55].

Additionally, other groups also explored MRI for guidance of an HDR brachytherapy procedure, to perform visualization or tracking of the catheters during insertion [19, 34]. However, these groups used MRI particularly for guidance during catheter insertion, whereas they have not explored real-time MRI-guided treatment verification. In general, the techniques for MR-based tracking of interventional devices can be divided into two groups: passive tracking and active tracking. Passive tracking depends on variations in signal intensities created by the interventional device, which can be either positive contrast due to modification of the MR sequence or image processing [81, 82, 84–86], or negative contrast relying on visualization of a device using the signal void or artifact [79, 80]. A passive tracking technique explored in our institution involves detection of an HDR brachytherapy source position, but its temporal resolution is not sufficient for real-time application (i.e. a temporal resolution of 4 s) [83]. On the other hand, active tracking techniques are inherently faster, but involve small coils embedded into the device to collect a signal for tracking, separately from the receiver coils, or to locally enhance the signal to visualize the position of the device [90–92].

The application of MRI for HDR source localization has unique challenges due to artifacts induced by the magnetic susceptibility of the paramagnetic materials used in HDR brachytherapy (e.g. the steel encapsulation of the HDR source). These susceptibility artifacts are caused by distortion of the static magnetic field: strong field gradients are present in the area surrounding the (para)magnetic object. These local magnetic field distortions cause intravoxel dephasing, and thus signal losses, and geometric distortions [71, 64]. Besides, two important requirements are imposed on real-time HDR source localization during an MRI-guided intervention. First, an accurate automatic determination of the source position coordinates in 3D is necessary, rather than only demonstrating a typical contrast in the MR image. Second, fast MR image acquisition/reconstruction and processing with low latency are needed to be able to verify the dwell positions in real time, including the positions with the shortest dwell times in the order of 0.3 s.

Instead of viewing the MR artifacts induced by the HDR source as a detrimental effect, the artifacts can be exploited to determine the source position. Wachowicz *et al* performed this by modeling the artifacts around a low-dose-rate (LDR) brachytherapy seed (using an iterative algorithm), and employing this information in a normalized cross-correlation to find the positions of the seeds placed in the prostate [76]. Alternatively, direct forward simulation, based on the magnetic susceptibility distribution and its field disturbance, is a more straightforward method for simulation of the steady state signal of a gradient echo sequence [78]. In this paper, we present a method based on this type of simulation in combination with a phase correlation algorithm [127], to automatically localize the HDR source.

This paper describes the simulation of the complex-valued MR signal representing the artifact around an HDR brachytherapy source, employed to find the source position by matching the experimental MR data to the simulated data using a phase correlation technique. MR acquisition using a 2D gradient echo sequence, with a short TE and TR, enabled imaging with short dynamic scan times. For real-time localization in 3D, two intersecting slices were acquired interleaved. For the purpose of obtaining even higher temporal resolutions, two techniques were introduced to accelerate: the acquisition of images with lower spatial resolutions combined with subpixel source localization and the application of parallel imaging (sensitivity encoding). Furthermore, the accuracy and precision of the method were investigated by a comparison with the source position on CT, serving as the gold standard.

3.2 Methods

3.2.1 Simulations

Simulation of the MR artifacts, induced by the magnetic susceptibility of the HDR brachytherapy source, was implemented in Matlab (The Mathworks, Natick, Massachusetts, United States). This section (3.2.1) explains the separate steps of the simulation process.

Geometry model

A cross-section of the geometric design of the Flexisource Ir-192 HDR source (Elekta NL, Veenendaal, The Netherlands), is shown in figure 3.1a. A 3D geometry model of the source, $G(x, y, z)$, was generated, on a cubic grid with 0.1 mm isotropic resolution. The source was defined as a cylinder of iridium (radius = 0.30 mm, length = 3.55 mm), surrounded by a steel capsule (radius = 0.45 mm, length = 4.4 mm), connected to a steel cable (radius = 0.25 mm, infinite length), schematically depicted in figure 3.1b. The borders of the cylinders were smoothed, to take into account partial volume voxels. The model was generated in a 3D Cartesian coordinate system, with the static magnetic field, $\vec{B}_0$, pointing along the positive z-axis. The orientation of the long axis of the source with respect to $\vec{B}_0$ was described by the angles θ (angle about the x-axis) and φ (angle about the y-axis), indicated in figures 3.1c and 3.1d.

Susceptibility distribution

Based on the geometry model, the susceptibility distribution, $\chi(x, y, z)$, was defined by assigning a susceptibility value to each material: $\chi_{iridium}$ = 3.66×10^{-5} [63], χ_{water} = -9.05×10^{-6} [62], and χ_{steel} = 1.2×10^{-2}. Here, the source was assumed to be surrounded by water, and the susceptibility of the steel parts was empirically determined by varying χ_{steel} and searching for the best match between the simulated and the acquired MR artifact, as the actual susceptibility of the concerned steel type was not provided.

Magnetic field perturbation

From the susceptibility distribution, the induced magnetic field perturbation, $\Delta B_0(x, y, z)$, was obtained using a forward calculation of the susceptibility induced field shift, applying a Fourier-based convolution method in combination with virtual zero-padding [69]. This calculation involves a convolution between the 3D susceptibility distribution and a dipole kernel (defined as the Green's function), followed by a subtraction of the aliasing field disturbance.

MR signal

To be able to simulate the MR signal in the vicinity of the perturbing source, a 3D matrix of the signal generating proton distribution, $\rho(x, y, z)$, was introduced (based on the model $G(x, y, z)$), where:

$$\begin{aligned} \rho(x, y, z) &= 1, \text{ for voxels containing water,} \\ 1 > \rho(x, y, z) &> 0, \text{ for partial volume voxels, and} \\ \rho(x, y, z) &= 0, \text{ for voxels containing the source.} \end{aligned} \tag{3.1}$$

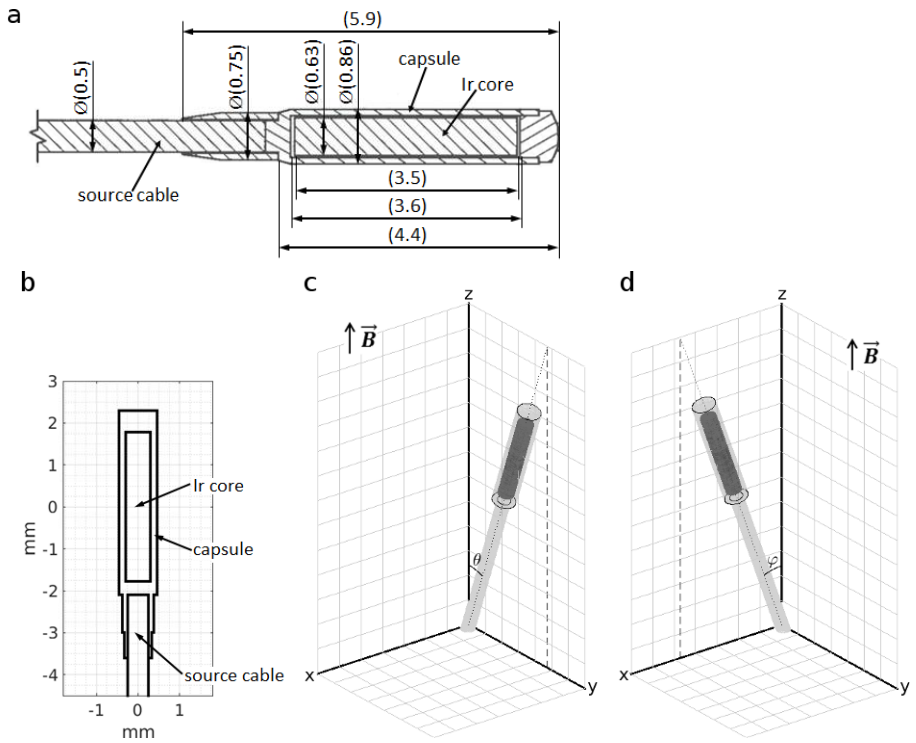

Figure 3.1 Cross-sections of **(a)** the geometric design of the Flexisource Ir-192 HDR source (dimensions given in mm) and **(b)** the simplified geometry model of the Ir-192 source, functioning as a base for the simulation of the MR signal. The source was modeled as a cylinder of iridium (diameter = 0.6 mm, length = 3.55 mm), surrounded by a steel capsule (diameter = 0.9 mm, length = 4.4 mm), and connected to a steel cable (diameter = 0.5 mm, infinite length). The source orientation in the 3D coordinate system was described by the angles θ and φ, where **(c)** shows the angle θ about the x-axis (here: $\theta = 20°$, $\varphi = 0°$), and **(d)** shows the angle φ about the y-axis (here: $\theta = 0°$, $\varphi = 20°$), and $\vec{B}_0$ pointed along the positive z-axis.

Furthermore, the slice location was described by the slice thickness and the angles θ_{slice} (angle about the x-axis) and φ_{slice} (angle about the y-axis), allowing the definition of coronal and sagittal slices with any desired orientation. The effects of the induced field perturbation on the slice excitation process were neglected, since these are small in the case of a large slice thickness. The matrices $\rho(x, y, z)$ and $\Delta B_0(x, y, z)$ were then rotated through the angles $-\theta_{slice}$ and $-\varphi_{slice}$, to align the calculation grid with the slice orientation. This enabled inclusion of signal variations over time along the readout direction. Intravoxel phase dispersion was taken into account by the fact that the computation was performed on an input matrix with a higher resolution (0.1 mm isotropic resolution) than that of the final simulated MR image.

The next step involved the actual simulation of the steady state MR signal. The local field inhomogeneity causes in-plane and through-plane signal losses due to intravoxel phase dispersion, and it gives rise to shifts in k-space, causing geometric distortion in the read-out direction [71]. In the case of a steady state signal, these effects can be simulated by calculating the relative signal changes over time during sampling, which involve spatially varying phase evolutions of the excited spin population. In other words, with the presence of a strong field inhomogeneity, the signal phase changes considerably during the short sampling time, which is an essential aspect for simulation of the artifact. Three main components contribute to the phase evolution, namely the local field perturbation, T_2 decay and the frequency encoding gradient. Because of the short echo times, the effect of T_2 decay was neglected. The change of the signal was then computed from the matrices $\rho(x, y, z)$ and $\Delta B_0(x, y, z)$, while taking into account scan parameters of the MR sequence, i.e. the echo time, TE, the field of view, FOV, and the sampling interval, Δt. For a readout direction along x, the signal for each k_x (at a certain time point during sampling), $S(k_x, y, z)$, was calculated as the sum over all voxels along x, all representing the signal of the voxel at that point in time [71, 78]:

$$S(k_x, y, z) = \sum_{j=1}^{N_x} \rho(x_j, y, z) \cdot \mathrm{e}^{i2\pi\gamma\Delta B_0(x_j,y,z)\cdot(TE+n\Delta t)} \cdot \mathrm{e}^{-i2\pi k_x x_j}, \tag{3.2}$$

where $k_x = \gamma G_R n \Delta t$, γ is the gyromagnetic ratio, G_R is the readout gradient strength defined as $G_R = \frac{1}{\gamma FOV_x \Delta t}$, and $n = -N_x/2...N_x/2 - 1$ with N_x the number of simulated voxels along the x direction (readout direction). The complex-valued MR signal (in image domain), $S(x, y, z)$, was obtained by computing the 1D inverse Fourier transform along the x-direction:

$$S(x, y, z) = \mathcal{F}^{-1}\left(S(k_x, y, z)\right). \tag{3.3}$$

Lastly, the complex summation of multiple adjacent voxels was calculated to resample $S(x, y, z)$ to a 2D image with a larger voxel size, to match the voxel size of the MRI acquisition in all three dimensions and, simultaneously, taking into account intravoxel phase dispersion.

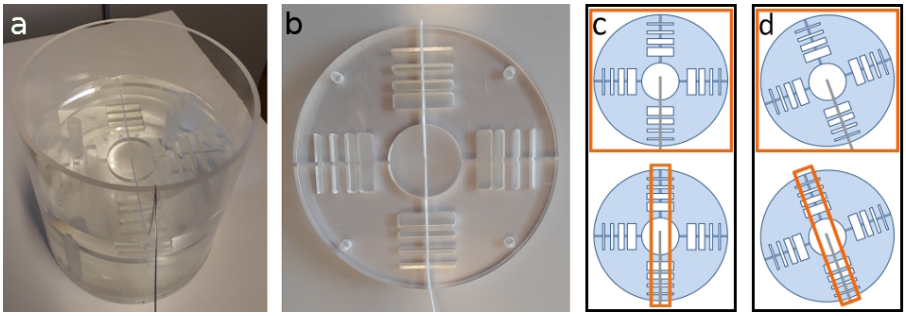

Figure 3.2 (a) The source was positioned in the center of a platform, placed in a cylindrical phantom filled with doped water. **(b)** The platform contained gaps, forming a reference in the MR/CT images. The source was positioned inside a tube in the center of a circle in the center of the platform. **(c-d)** Schematic representations of the slice orientations of the coronal (top image) and sagittal slices (bottom image) by the orange boxes, for angulations of the phantom/source of 0° and 20° respectively (viewed from above).

3.2.2 Experiments

Measurement set-up

In the experimental set-up, a non-active Ir Flexisource was used (Elekta NL, Veenendaal, The Netherlands), schematically depicted in figure 3.1a. A cylindrical phantom was designed, containing a Perspex platform in which a plastic tube was fixed for positioning of the source in the center of the platform, inside the tube (figure 3.2a). The platform was created with a pattern of gaps, see figure 3.2b, forming a reference in the images and facilitating registrations between different data sets. The cylinder was filled with doped water ($\approx$ 25 mg/l $MnCl_2$) and covered to prevent motion artifacts due to water movements.

The orientation of the HDR source with respect to $\vec{B}_0$ was varied by rotating the phantom, as the MR artifact depends on the angle between the source orientation and $\vec{B}_0$. Angles of 0°, 10°, 15°, 20°, 30°, 45°, 60°, 75° and 90° were applied.

MR acquisition

MR imaging was conducted on a 1.5 T Ingenia MRI system (Philips Healthcare, Best, The Netherlands), using a 28-channel anterior/posterior coil. A 2D dynamic spoiled gradient echo sequence was applied, with TE/TR = 2.26/4.60 ms, FOV = 256×256 mm^2, slice thickness = 10 mm, acquisition matrix = 256×256, readout bandwidth = 434 Hz/pixel, flip angle = 30° and 10 dynamics. The readout direction was applied along the feet-head (FH) direction. Two intersecting 2D slices (sagittal and coronal) were acquired, to allow determination of the source position in 3D. The slices were oriented such that the source cable was positioned in-plane. The coronal slice was not angulated and the sagittal slice was angulated

Table 3.1 The scan parameters of the dynamic 2D spoiled gradient echo sequence with spatial resolutions of 1×1 mm^2, 2×2 mm^2, 2.5×2.5 mm^2 and 3×3 mm^2 respectively. The dynamic scan time applies for the acquisition of both slices.

	Spatial resolution (mm^2)			
	1×1	2×2	2.5×2.5	3×3
TE/TR (ms)	2.26/4.60	1.92/3.99	1.76/3.70	1.69/3.60
FOV (mm^2)	256×256	256×256	240×240	240×240
Slice thickness (mm)	10	10	10	10
Flip angle	30°	30°	30°	30°
Readout bandwidth (Hz/pixel)	434	434	479	500
Dynamic scan time (s), SENSE = 1 / 2	2.4/1.2	1.1/0.54	0.75/0.39	0.61/0.32

equal to the rotation of the phantom in each acquisition, see figure 3.2c-d for a schematic representation.

For the purpose of increasing the temporal resolution, the spatial resolution was decreased to 2×2 mm^2, 2.5×2.5 mm^2 and 3×3 mm^2 (besides the resolution of 1×1 mm^2 described above), see Table 3.1 for the scan parameters, including the dynamic scan times. To further increase the temporal resolution, the acquisitions were repeated with the application of the parallel imaging technique sensitivity encoding (SENSE) [128], using a SENSE factor of 2. In total, 800 images were acquired (10 dynamics, 4 spatial resolutions, no SENSE/SENSE=2, and 10 angulations).

To assess the ability to perform subpixel localization, and to assess its precision, an additional series of MR images was acquired (with the source positioned in a tube inside an Agar phantom with ≈25 mg/l $MnCl_2$), where artificial subpixel shifts of the sagittal MR images were applied. This was accomplished by performing subsequent MR acquisitions (with 2 mm spatial resolution, SENSE=2 and 10 dynamics), while shifting the FOV such that the off center changed in steps of exactly 0.1 mm in either AP or FH direction.

CT imaging

To validate the described source localization method, CT images of the phantom were acquired, and care was taken that the source position within the phantom stayed unchanged during the CT and MR acquisitions. CT imaging was performed on a Philips Brilliance Big Bore CT scanner (Philips Healthcare, Best, The Netherlands), with the following settings: 120 kVp, 450 mAs, and voxel size: 0.34×0.34×0.40 mm^3. The images were processed using the O-MAR algorithm for metal artifact reduction. The source position on CT was used as the gold standard.

3.2.3 Post-processing

Source localization

Source localization was conducted by phase correlation [127] on the complex-valued acquired MR data and the complex-valued simulated data. Phase correlation is a cross-correlation, normalized in the frequency domain, that acquires the information of a displacement of two images from the phase of the cross power spectrum. This algorithm is less sensitive to noise than a general cross-correlation. The phase correlation was carried out on the complex images, instead of only the magnitude images, providing more information to the algorithm. It was applied to find the translation between the acquired MR data and the simulated data containing the simulated object at its center. First, the normalized cross power spectrum, $P(k_x, k_y)$ was calculated:

$$P(k_x, k_y) = \frac{I_{MR}(k_x, k_y) \cdot I^*_{sim}(k_x, k_y)}{|I_{MR}(k_x, k_y) \cdot I^*_{sim}(k_x, k_y)|}, \tag{3.4}$$

where $I_{MR}(k_x, k_y)$ is the 2D discrete Fourier transform of the acquired complex MR data and $I^*_{sim}(k_x, k_y)$ is the complex conjugate of the 2D discrete Fourier transform of the simulated complex data. To create subpixel accuracy, Fourier interpolation was implemented by zero-padding $P(k_x, k_y)$ in k-space, with a factor needed to create a spatial resolution of 0.1×0.1 mm^2 in image domain. The phase correlation, $p(x, y)$, was then obtained by the 2D inverse discrete Fourier transform of the zero-padded $P(k_x, k_y)$:

$$p(x, y) = \mathrm{FFT}^{-1} \left(P(k_x, k_y)_{\text{zero-padded}} \right). \tag{3.5}$$

The HDR source position was obtained from the location of the maximum absolute value in the interpolated phase correlation image.

The source localization algorithm was applied to all MR images and their corresponding simulated images (with corresponding source and slice angulations), see figure 3.3a.

Registration

The coronal and sagittal MR images were registered to the CT data set (figure 3.3b). For each angulation of the phantom and source, a registration was conducted, i.e. one registration (based on 1 mm resolution and no SENSE) for all dynamic series with equal angulations, to prevent errors due to the registration. The registration (translation) of the coronal images was performed using the Elastix toolbox [129], employing mutual information. This translation was based on the border of the circle in the center of the phantom platform. A translational registration was sufficient, as the source was positioned in the center of the circle which would not change due to a rotation. This minimized errors due to registration. Regarding the sagittal images, the MR images were manually registered (translation) to the CT data set.

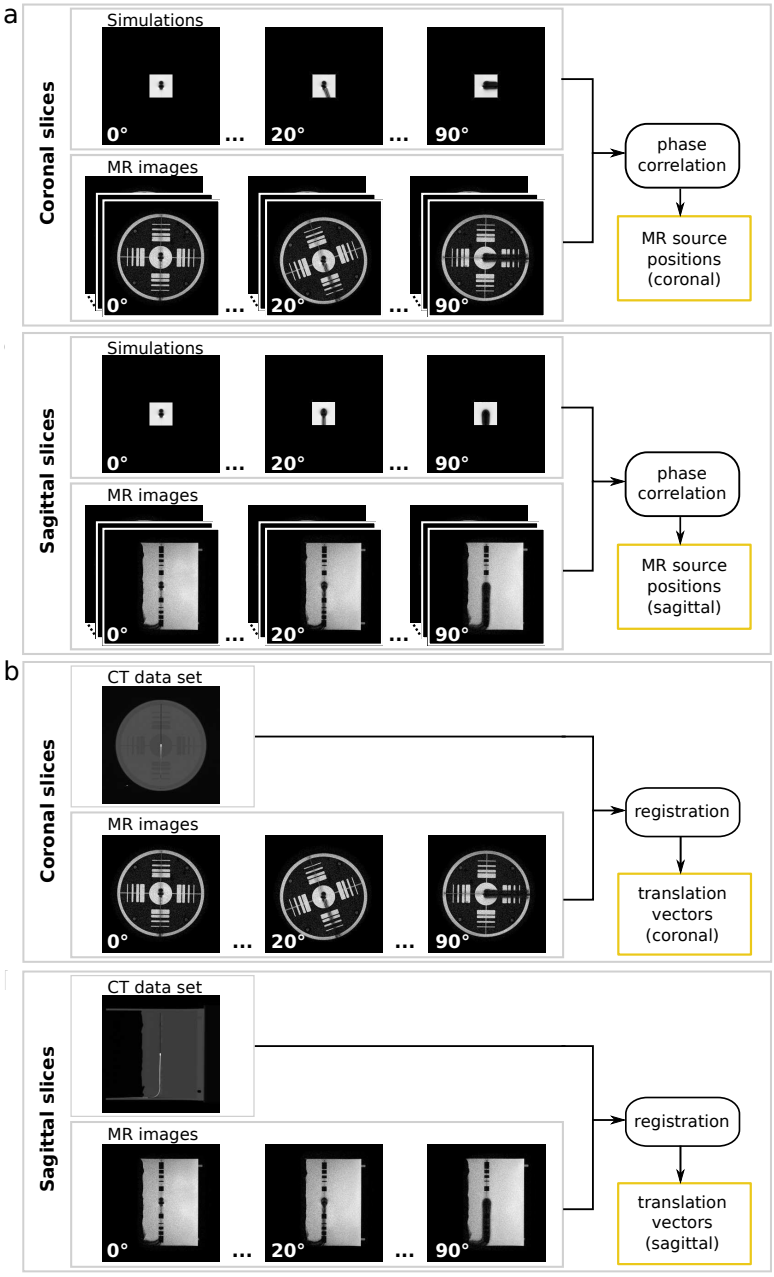

Figure 3.3 (a) The subpixel phase correlation localization algorithm was applied to each MR image and its corresponding simulated image (corresponding orientation and resolution) to determine the source position in the MR image. **(b)** The coronal and sagittal MR images were registered to the coronal and sagittal CT images obtained from the 3D CT data set. A translation vector was determined for each angulation of the phantom.

The translation vectors were applied to the HDR source positions obtained from the localization algorithm. Next, the translated HDR source positions from the coronal and sagittal images were combined to a 3D position of the HDR source on MRI (RL and FH position from the coronal slice and AP position from the sagittal slice).

3.2.4 Validation: accuracy and precision

To analyze the accuracy of the HDR source localization, the source positions determined from MR were compared to the source position on CT (i.e. the gold standard). For each combination of resolution, SENSE factor and angulation, the mean Euclidean distance between the positions from MR and CT was calculated:

$$\text{Mean distance} = \frac{1}{n}\sum_{i=1}^{n}\sqrt{(x_{\text{MRI},i}-x_{\text{CT}})^2+(y_{\text{MRI},i}-y_{\text{CT}})^2+(z_{\text{MRI},i}-z_{CT})^2}, \tag{3.6}$$

where n=10 (10 dynamics).

The precision of the method was analyzed as the standard deviation over the Euclidean distances between the positions from MR and CT (over 10 dynamics). Furthermore, the MR data where the FOV was shifted on submillimeter scales in subsequent acquisitions also indicated the precision.

3.3 Results

3.3.1 Simulations

The magnitude, real, imaginary and phase images of the simulations and the acquired MR data are presented in figure 3.4. The simulated images were in close agreement with the MR images for the range of angulations of the source with respect to $\vec{B}_0$, of which three examples are presented here: (I) an angulation of 0° (figure 3.4a), (II) an angulation of 20° (coronal and sagittal slices in figures 3.4b and 3.4c respectively), and (III) an angulation of 90° (coronal and sagittal slices in figures 3.4d and 3.4e respectively). This proved that the described method allows simulation of the MR artifact induced by the HDR brachytherapy source.

Additionally, as extensively described by others [71, 64], the magnitude presented a large signal void due to off-resonance effects in the region surrounding the source. Consequently, detection of the brachytherapy source position based on solely the magnitude signal void is difficult, since the signal void can overlap with signal voids caused by other mechanisms, such as a bleeding or the presence of arteries. Here, the full complex data were simulated, as demonstrated in figure 3.4, which enabled to provide more information to the phase correlation algorithm (instead of simply using the magnitude images), for an increased robustness.

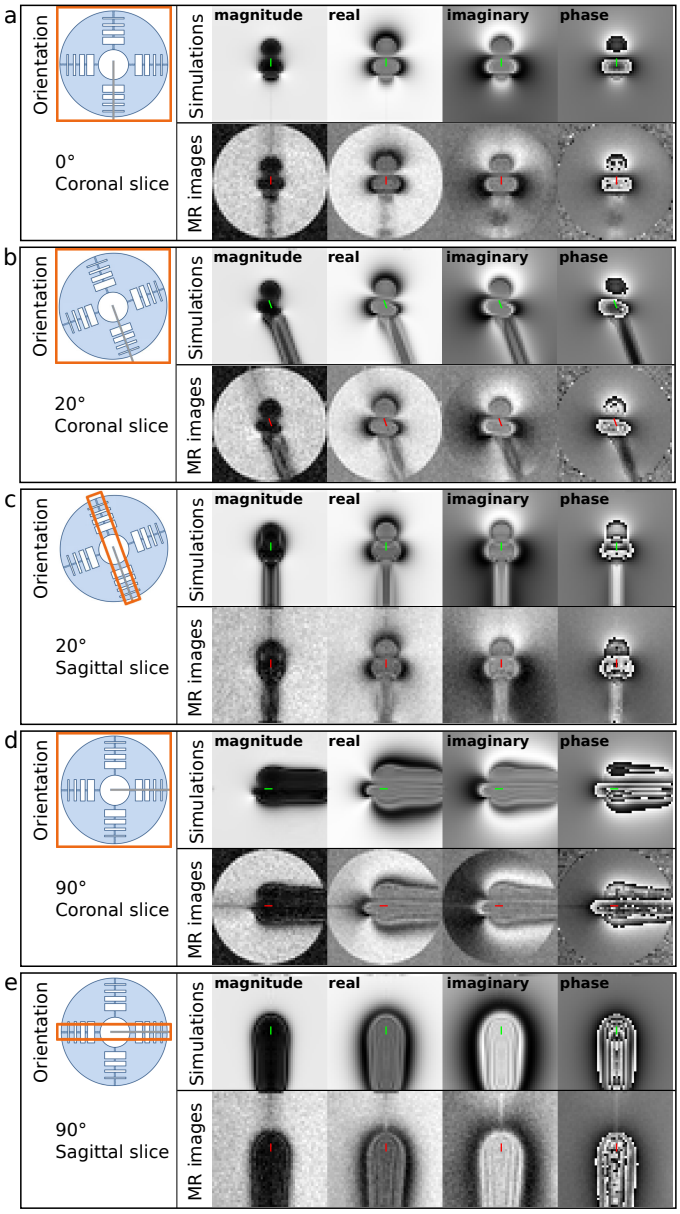

Figure 3.4 The magnitude, real, imaginary and phase representations (from left to right) of the simulations (top rows) and the acquired MR artifact (bottom rows) (resolution = 1 mm, no SENSE). The images represent **(a)** a coronal slice with a source angulation of 0°, **(b-c)** a coronal and sagittal slice respectively with a source angulation of 20°, and **(d-e)** a coronal and sagittal slice respectively with a source angulation of 90°. The orange boxes (first column) schematically represent the slice orientation with respect to the phantom/source. The simulated and detected source positions are overlaid in green and red respectively.

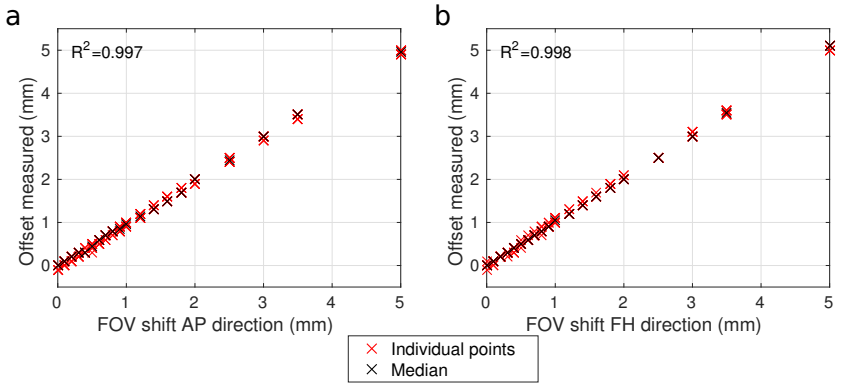

Figure 3.5 The measured offsets versus the actual shifts applied **(a)** in AP direction, and **(b)** in FH direction, when the FOV/off center position was shifted on submillimeter scales. The individual measurement points (in red, n=10) and the median (in black) are presented, for the MR acquisition with a spatial resolution of 2×2 mm^2 and SENSE=2.

3.3.2 Source localization

The HDR source could be localized in the MR images, using the simulated images, demonstrated in figure 3.4. The figures show examples of the HDR source positions detected from the MR images, overlaid in red on the images (bottom rows of figures 3.4a-3.4e). These positions of the source with respect to the MR artifacts, corresponded well with the simulated source positions with respect to the simulated artifacts, indicated in green in the top row images of figure 3.4. This was observed for the situation where the source was aligned parallel with $\vec{B}_0$ (figure 3.4a) as well as for the coronal and sagittal slices of the investigated angulations (examples in figures 3.4b-3.4e). These results demonstrated the ability to determine the source position using MR artifact simulation in combination with the described localization algorithm.

Figure 3.5 demonstrates the offsets measured when the FOV was shifted in either the AP direction (Figure 3.5a) or the FH direction (Figure 3.5b). The measured offsets corresponded closely to the actual shifts of the FOV that were applied in the scan parameters, for both the AP and FH directions (R^2 = 0.997 and R^2 = 0.998 respectively). Accordingly, this proved the ability to determine the source position on a subpixel scale.

3.3.3 Dynamic scan time optimization

The study with the purpose to increase the temporal resolution demonstrated that the source position could be determined on a subpixel scale, independent of the spatial resolutions of 1×1 mm^2, 2×2 mm^2, 2.5×2.5 mm^2 and 3×3 mm^2, see figure 3.6. Moreover, a SENSE factor of 2 could be applied without decreasing the ability to localize the source on a subpixel scale, shown in the bottom row of figure 3.6. Accordingly, the dynamic scan time could be

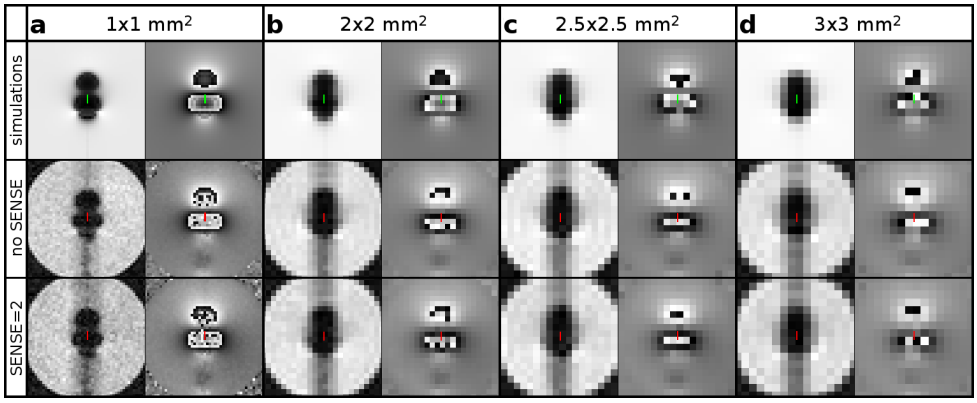

Figure 3.6 The magnitude (left) and phase (right) representations of the susceptibility artifact induced by the HDR source, where the spatial resolution was varied: **(a)** 1×1 mm^2, **(b)** 2×2 mm^2, **(c)** 2.5×2.5 mm^2 and **(d)** 3×3 mm^2. The top row shows the simulations, the middle row the acquired MR artifact without SENSE and the bottom row shows the acquired MR artifact with SENSE=2. The simulated source position is overlaid in green and the detected source positions are overlaid in red on the images.

highly decreased without substantially affecting the accuracy of the HDR source localization procedure. For example, a dynamic scan time of 0.54 s (0.27 s per image) for 2 mm resolution and SENSE=2, and a dynamic scan time of 0.39 s (0.19 s per image) for 2.5 mm resolution and SENSE=2, were obtained. When the resolution was further decreased to 3×3 mm^2 (and SENSE=2), the dynamic scan time was even decreased to only 0.32 s (0.16 s per image). These outcomes are favorable for the perspective of proceeding towards a real-time application.

3.3.4 Validation

Accuracy

The mean distances between the HDR source positions found on MR and CT, calculated to validate the described method, are provided in table 3.2. Each value represents the mean distance for the specific combination of resolution, SENSE factor and source angulation (over 10 dynamics). For the 1 mm and 2 mm resolution images, all distances were below or equal to 0.5 mm for angulations up to 45° and below or equal to 0.8 mm for the higher angulations. The distances increased as the image resolution decreased. Besides, larger distances were found with an increasing source angulation. However, up to the 3×3 mm^2 resolution images and a SENSE factor of 2, the distance never exceeded 1.0 mm, which is always smaller than the pixel resolution and which is clinically acceptable. Overall, the validation resulted in mean accuracies of 0.4-0.6 mm.

Table 3.2 The mean distances (in mm) between the HDR source positions from MRI and CT, for the different combinations of spatial resolution, SENSE factor and angulation (calculated over 10 dynamic images). All standard deviations were $\leq$0.1 mm.

Resolution (mm)	SENSE factor	Angle										
		0°	5°	10°	15°	20°	30°	45°	60°	75°	90°	Mean
1	-	0.4	0.3	0.3	0.3	0.3	0.4	0.4	0.7	0.7	0.7	0.4
1	2	0.4	0.3	0.3	0.3	0.3	0.4	0.4	0.7	0.7	0.7	0.4
2	-	0.5	0.4	0.3	0.5	0.5	0.4	0.5	0.5	0.7	0.7	0.5
2	2	0.5	0.4	0.3	0.4	0.4	0.4	0.5	0.5	0.8	0.8	0.5
2.5	-	0.6	0.5	0.5	0.7	0.5	0.5	0.7	0.6	0.7	0.8	0.6
2.5	2	0.7	0.5	0.5	0.7	0.4	0.5	0.7	0.6	0.8	0.8	0.6
3	-	0.7	0.5	0.5	0.6	0.5	0.5	0.5	0.6	0.8	0.9	0.6
3	2	0.7	0.5	0.5	0.5	0.5	0.4	0.5	0.5	1.0	1.0	0.6

Precision

Almost no variations were found between the source positions that were obtained for the 10 dynamic images of each series (i.e. each combination of resolution, SENSE factor and angulation). This resulted in standard deviations very close to 0, namely below or equal to 0.1 mm. The low standard deviations, together with the high correlations between the applied and the measured FOV shifts (shown in figure 3.5), proved a particularly high precision of the method ($\leq$0.1 mm).

3.4 Discussion

The goal of this paper was the development of a method for MR-based tracking of an HDR brachytherapy source with high spatial and temporal resolutions. This has been the first study to our knowledge to approach a real-time treatment verification by MRI guidance. The usage of MRI for HDR source tracking provides the significant benefit that one imaging modality can be employed for both anatomical imaging as well as detection of the HDR source position, both in the same coordinate system. Furthermore, MR-guided source tracking might fulfill two important aims during an HDR brachytherapy treatment. First, it enables real-time treatment verification, which has not been applied in the current clinical treatments. Second, when employing a dummy source, it provides an automatic detection of the source dwell positions, to replace a manual catheter reconstruction. This last aspect would provide a significant improvement over the current treatment workflow, as manual catheter reconstruction introduces inaccuracies (catheter tip is often difficult to distinguish), and it is an extra manual interaction as well as a time consuming operation.

The artifacts induced by the source were simulated. The simulated images have demonstrated

that simulation of the artifact due to the HDR source was feasible, for the range of examined angulations of the source and slices with respect to $\vec{B}_0$. This indicated that the simulations are valid for all potential angulations of the source and slice. In this study, the MR acquisitions were conducted with certain angulations of the source and slices and, based on these angles, the simulations were carried out. When moving towards a clinical situation, a workflow can be designed where a library of simulated images is built and where during the treatment, for each acquired MR image, the best matching simulated image would be selected before applying the localization algorithm.

Localization of the source was performed by a phase correlation algorithm. The HDR source position could be determined with an accuracy higher than the voxel size. This position determination on a subpixel basis, combined with lower spatial resolution images, has resulted in reduced dynamic scan times. Parallel imaging (SENSE) was applied to further reduce the scan times. While the scan time decreased, the processing of extensive matrices (created after zeropadding with large factors) increased computational complexity and this may compromise the gain in efficiency. A remedy for this could be to first determine the point of maximum correlation of the phase correlation applied without zeropadding, and then select a smaller area around this point as an input for the phase correlation algorithm with zeropadding to determine the subpixel source position.

The HDR source localization method was validated by comparison with CT, serving as the gold standard, and has proven to be highly accurate (0.4-0.6 mm) and precise ($\leq$0.1 mm). The case most plausible for practical application (2 mm resolution and SENSE=2) resulted in an accuracy of 0.5 mm, which is slightly higher than the accuracy of 0.7 mm for the current catheter reconstruction tools for HDR prostate brachytherapy [130]. Furthermore, the results proved a high precision of $\leq$0.1 mm, meaning a high repeatability of the determined source positions for the consecutive dynamics of each series of MR images. This was also confirmed by the high correlation between the measured offsets and the actual shifts applied when the FOV was shifted on a subpixel scale, shown in figure 3.5. The high accuracy and precision make the described HDR source localization method highly valuable for both treatment verification and reconstruction of the source dwell positions.

Regarding the future goal of real-time treatment verification, fast acquisition/reconstruction and processing with a low latency are required to be able to verify the source dwell positions in real time. A reduction of the dynamic scan time was obtained by subvoxel source localization in combination with lower spatial resolution imaging and the application of SENSE. MR images could be acquired with the short dynamic scan time of, for example, 0.27 s per image for a spatial resolution of 2 mm and SENSE=2. Additionally, reconstruction can be performed fast, since it concerns a basic 2D SENSE reconstruction, which is feasible in real time employing dedicated hardware [131, 132]. Also the post-processing is a fast procedure, as the phase correlation is calculated as a multiplication in k-space. Besides, as already mentioned above, the post-processing time could be decreased by applying phase correlation with zeropadding to a smaller section of the image. Altogether, a high temporal resolution and a low latency (on the order of a few hundred milliseconds) might be expected, indicating that the time scales are on the order of a real-time process, which would enable to verify the HDR

source position in real time.

For now, this work has showed the ability to determine the HDR source position in a phantom study. Future investigations will focus on applying the described method *in* vivo (using a dummy source). Furthermore, ideally, the HDR source tracking procedure would be applied in combination with anatomy tracking to simultaneously track the organs and determine the HDR source position with respect to the positions of the organs and the tumor. This would enable an even more valuable treatment verification.

The current limitation for a clinical application of the described method for real-time HDR source tracking is concerned with MR safety of the equipment used in HDR brachytherapy. HDR source tracking during the treatment requires the afterloader to be positioned in the MRI scanner room at the moment of MR acquisition. However, with the current afterloading system, MR acquisition is not possible when the afterloader is positioned inside the scanner room due to RF noise. This demands for an MR-conditional afterloader, which is currently in development [133].

Regarding the aim of automatic detection of the source dwell positions in the treatment planning process, the first steps towards applying the described method in a clinical situation can already be made. We are planning to test our method for an automatic determination of the dwell positions using an adjusted dummy source (MR conditional) or marker. This could replace a manual catheter reconstruction, leading to a more straightforward and faster workflow with less manual operations and a higher accuracy. Accordingly, reconstruction errors could be avoided.

The two main requirements imposed on real-time HDR source tracking using MRI are (I) an accurate automatic source position determination in 3D, and (II) fast image acquisition/reconstruction and a low latency. These requirements have been met as described above. For the HDR brachytherapy treatment, this means that treatment verification would become possible and that source dwell positions could be determined automatically after catheter insertion. For both the current HDR brachytherapy treatment as well as future robotic treatments, the accuracy and practical workflow of the treatment could be considerably improved by implementation of real-time HDR source tracking.

3.5 Conclusion

This paper has demonstrated the development of a method for MR-based localization of an HDR brachytherapy source. We have described the simulation of the MR artifact induced around an Ir-192 HDR brachytherapy source, applied to a phase correlation localization algorithm to find the HDR source position. This resulted in determination of the source position with a high, subvoxel accuracy (0.4-0.6 mm) and a high precision ($\leq$0.1 mm) at high temporal resolutions (0.15-1.2 s per slice). Accordingly, the described method enables real-time treatment verification for HDR brachytherapy as well as an automatic detection of the source dwell positions, which could replace a manual catheter reconstruction. This shows that the

proposed method is highly valuable for clinical application for MR-guided HDR brachytherapy.

Acknowledgments

This research was funded by the Eurostars Programme, ITEA3, project name: System of Real-Time Systems (SoRTS), project number: 12026.

Chapter 4

Development and testing of an MR conditional afterloader for source tracking in MRI-guided HDR brachytherapy

The following chapter is based on:

Ellis Beld, Peter R. Seevinck, Jeroen Schuurman, Max A. Viergever, Jan J.W. Lagendijk and Marinus A. Moerland

International Journal of Radiation Oncology, Biology, Physics (2018) 102: 960–968

Abstract

For the purpose of magnetic resonance imaging (MRI)-guided high-dose-rate (HDR) brachytherapy, a prototype magnetic resonance (MR) conditional afterloader was developed. This study demonstrates the development and testing of the prototype, while operating simultaneously with MRI. In combination with an MR-based method for HDR source localization, this development enables treatment verification of HDR brachytherapy. Additionally, this allows a direct reconstruction of the source dwell positions after catheter insertion (when using a dummy source) and introduction of a clinical workflow where the patient remains in the same position during dwell position reconstruction, treatment planning and irradiation. A prototype MR conditional afterloader was developed by providing radiofrequency (RF) shielding and a plastic source cable containing a dummy source. Simultaneous functioning of the afterloader and MRI acquisition was tested in an experimental setting where the afterloader was placed next to the scanner and programmed to send the source to predefined positions within a phantom, while acquiring MR images. The HDR source positions were determined using MR artifact simulation and matching of the MR images to the simulated artifact. Additionally, the impact of the presence and use of the afterloader on the MRI performance was investigated by assessment of RF interference, signal-to-noise ratio (SNR), and B_0 field homogeneity. The experiments demonstrated that the prototype MR conditional afterloader and the MRI scanner fully functioned while operating simultaneously, without influencing the other system. The step sizes between the source positions obtained from the MR images corresponded with the afterloader settings. Besides, the MRI performance tests demonstrated no deterioration due to the presence or functioning of the afterloader next to the scanner. This research has demonstrated the feasibility of simultaneous MR acquisition and employment of an MR conditional afterloader. This development enables real-time HDR source localization for treatment verification of MRI-guided HDR brachytherapy using an MR conditional afterloader.

4.1 Introduction

In high-dose-rate (HDR) brachytherapy, image guidance is crucial for accurate and safe dose delivery. Magnetic resonance imaging (MRI) is the imaging modality preferred for guidance of the treatment, as it provides high soft tissue contrasts as well as the ability of guidance of interventional procedures and detection of interventional devices [20, 22, 134]. Accordingly, we have been working on the development of magnetic resonance (MR)-guided HDR brachytherapy in recent years. We have demonstrated that MRI can be applied to localize an HDR brachytherapy source for the purpose of treatment verification [135], which would highly improve treatment safety and accuracy. Additionally, MR-based source localization allows a direct reconstruction of the source dwell positions after catheter reconstruction when employing a dummy source. This might enable the realization of an improved clinical workflow where the patient stays in the same position during dwell position reconstruction, treatment planning, and the irradiation process. However, a practical application of this MR-based source localization method involves employment of the brachytherapy afterloader in the MRI room near the patient, and thus near the MR bore, simultaneously with MRI acquisition. This demands for an MR conditional afterloader.

Real-time treatment verification of HDR brachytherapy would lead to a large improvement of the current clinical practice. High doses are delivered in short periods of time, especially in single fraction treatments, and errors in source positioning during the treatment can have an enormous impact on the delivered dose because of the steep dose gradients. Due to the large number of manual operations, HDR brachytherapy is involved with relatively high chances on errors/incidents (eg, reconstruction errors, wrong catheter/indexer length, catheter mislabeling, or incorrect afterloader connection [36, 37]. Other sources of errors, not related to human errors, include afterloader malfunction and applicator displacements. Several MRI studies of HDR brachytherapy have demonstrated the occurrence of substantial catheter displacements and anatomical changes during one to three hours following catheter insertion [39, 42]. To prevent or detect these errors or changes, treatment verification is highly valuable.

Various techniques for HDR brachytherapy treatment verification have been investigated, for example, in vivo dosimetry with detectors [51, 124, 125], electromagnetic tracking [52, 57, 136, 137], fluoroscopy [126], source tracking with a flat panel detector [138], and fiber Bragg gratings-based sensing [59]. However, none of these techniques has actually been applied in current clinical practice[55]. MRI has been applied for guidance during catheter insertion or catheter reconstruction [19, 34, 35, 139]. However, this requires movements of the patient in and out of the MR bore, leading to possible catheter displacements or anatomy changes between the catheter reconstruction and the actual dose delivery. In a treatment set-up where MRI is employed for treatment verification in combination with an MR conditional afterloader, MR-based source localization can be applied for a direct reconstruction of the source positions using a dummy source [135] and after treatment planning the dose can be delivered, while the patient stays in the MR bore during all consecutive steps. Additionally, MRI guidance is significantly beneficial as a single imaging modality is utilized for anatomical imaging as well as detection of the HDR source position.

Real-time treatment verification by MRI guidance is not possible with the current types of afterloaders for several reasons. First, MR imaging is impossible when the afterloader is positioned in the MR room. The afterloader generates radiofrequency (RF) signals that might interfere with the RF signals emitted by the nuclear spins, hampering the signal encoding process. Furthermore, the data cable that connects the afterloader with the treatment control station is a source of RF leakage into the MRI room. Second, a correct functioning of the afterloader might be affected by RF signals generated by the MRI scanner. These signals should be prohibited from entering the afterloader to guarantee reliability and a correct functioning of the afterloader. Furthermore, the afterloader's electronic system contains parts that are hampered by the strong magnetic field. Third, the current source cables made of steel would act as an RF antenna from the inside of the afterloader into the MR bore. Additionally, the steel cable poses safety risks of RF induced heating and torques. Accordingly, this defines the need for an MR conditional afterloader to prevent interference of RF signals in both directions and to ensure safety.

This paper focuses on the development and testing of a prototype MR conditional afterloader. In combination with a recently developed method for MR-based HDR brachytherapy source localization, the feasibility of real-time HDR source tracking for dwell position reconstruction and treatment verification was investigated. The paper describes the design of the prototype MR conditional afterloader and the tests conducted to evaluate simultaneous functioning of the afterloader and MRI acquisition. Additionally, the impact on the MRI performance was investigated by assessment of RF interference, signal-to-noise ratio (SNR) and B_0 field homogeneity.

4.2 Methods and Materials

4.2.1 MR conditional afterloader

A prototype MR conditional afterloader, type Flexitron (Elekta NL, Veenendaal, The Netherlands), was developed. All parts of the afterloader, including the cover, were provided with a copper/aluminum coating for RF shielding. The data cable, that is the connection with the treatment control station outside the MRI room, was shielded with a conductive hose and brought in contact with the Faraday cage of the MRI room. Hence, transmission of RF signals from the afterloader to the scanner was prevented. One condition of the prototype afterloader that needs to be fulfilled is that it should stay outside the 20 mT line, to guarantee functioning of certain magnetic switches. Furthermore, the steel source cable was replaced by a plastic test cable containing a piece of steel at its tip that served as a dummy source. This test cable was longer than the original cable (i.e., 2.65 m instead of 1.40 m), enabling to send the source to the scanner's isocenter while the afterloader stays at a sufficient distance.

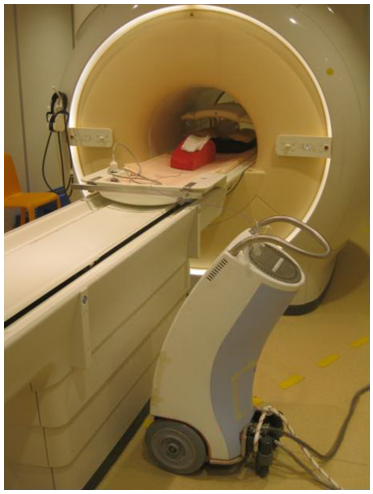

Figure 4.1 The prototype MR conditional afterloader, provided with RF shielding, positioned next to the MRI scanner at 2.1 m from the isocenter. The afterloader was connected to a plastic catheter that was inserted into a phantom.

4.2.2 Simultaneous MRI acquisition and afterloader employment

Experimental set-up

Measurements were conducted using a 1.5 T MRI scanner inside an MRI brachytherapy suite, where the current HDR brachytherapy treatments of our institute take place. This bunker is suitable for a future treatment set-up where MRI guidance is applied during the actual dose delivery for treatment verification. The prototype afterloader was placed next to the MRI scanner at 2.1 m from the isocenter (see Fig. 1). The measurements were performed utilizing a cylindrical Agar phantom (doped with $MnCl_2$), that contained a plastic catheter to which the afterloader was connected via a prototype plastic transfer tube. Two tests with different programmed source positions and dwell times were performed:

1. 10 source positions, 10 mm step size and 10 s per position;
2. 20 source positions, 5 mm step size and 0.5 s per position.

MRI acquisition

MR imaging was conducted on a 1.5 T Ingenia MRI system (Philips Healthcare, Best, The Netherlands). A 2D dynamic spoiled gradient echo sequence was applied, with interleaved scanning of two intersecting slices (coronal and sagittal). The imaging parameters were as follows: TR/TE: 2.2/1.03 ms, FOV: 192×192 mm^2, matrix size: 96×96, slice thickness: 10 mm, flip angle: 20°, readout bandwidth: 1915 Hz/pixel and SENSE = 2.

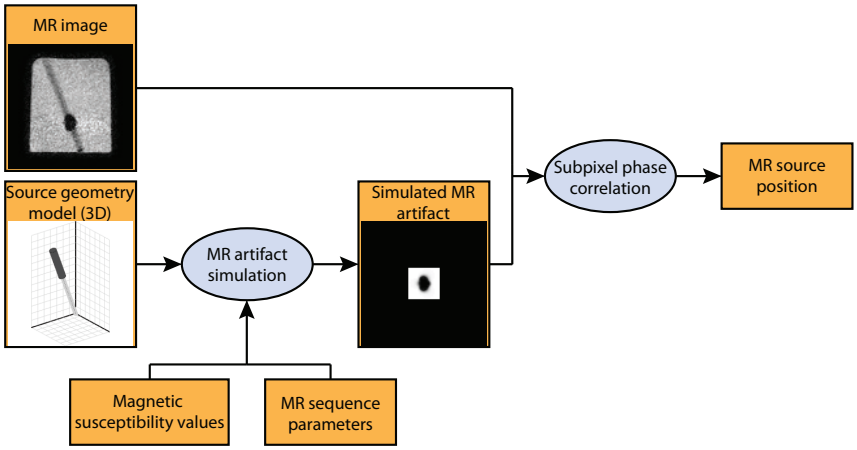

Figure 4.2 Workflow diagram that demonstrates the actions performed in the artifact simulation and the source localization. The input data consists of the MR image, a 3D source geometry model, the magnetic susceptibility values of the materials, and the MR sequence parameters. The output is the source position in the MR image.

HDR source localization

Localization of the dummy source was performed by the authors' method proposed for MR-based HDR source localization using MR artifact simulation and a phase correlation localization algorithm. A detailed description of the source localization method can be found elsewhere [135]. The dummy source was modeled as a cylinder (0.3 mm diameter and 4 mm length), and a magnetic susceptibility value ($\Delta\chi$) of 0.57 was assigned based on an optimization of the correspondence between the simulated artifact and the measured MR artifact. By adapting this geometry model to the applied source type (Ir-192 or dummy source), the simulations could be adapted to any desired type of source with known dimensions and materials. This model was employed for simulation of the MR artifact (complex-valued) induced by the dummy source. The simulated artifact was applied in a subpixel phase correlation algorithm, where the MR artifact was matched to the simulated artifact, to find the position of the dummy source in the MR image. Figure 2 presents the actions performed in the simulation and localization. The localization was carried out for the coronal and sagittal MR images. The two 2D positions were combined into a 3D position of the dummy source.

Analysis

The simultaneous functioning of the afterloader and MRI scanner was analyzed by localization of the dummy source (as described in the section *HDR source localization*) in the acquired MR images. The distances of the determined source positions with respect to the first position were calculated. Additionally, the step sizes were calculated as the distance

between each successive pair of source positions. The mean step sizes (±standard deviation) were compared to the step sizes of the afterloader settings.

4.2.3 MRI performance tests

The influence of the afterloader on the MR image quality was investigated, by the assessment of possible RF interference, SNR and B_0 homogeneity. The MRI performance tests described in this section were conducted for four different situations:

(i) Baseline measurement: no afterloader inside MRI room;

(ii) Afterloader present and powered, but not connected to the treatment control system;

(iii) Afterloader present, powered, and connected to the treatment control system;

(iv) Afterloader active (i.e., sending source to source positions).

As an exception, the B_0 homogeneity measurements were performed solely for situations (i) and (ii).

RF interference

A spurious signals test was conducted to check for possible RF signals generated by the afterloader and received by the MRI scanner. The MRI bore was empty (i.e., no phantom) except for a 1.75 m mains cable to receive and conduct possible signals. Scanning was performed using a pre-installed protocol (provided by the vendor) which applied five consecutive TSE sequences with shifted center frequencies and a bandwidth of 180 Hz/pixel (Δf_0 = 0, ±170 kHz, ±340 kHz, where f_0 = 63.87 MHz), with disabled gradients and RF power reduced to a minimum. Basically, the MRI system was used as a receiver only. The sequence parameters were: TR/TE: 581/256 ms, TSE factor: 32, acq. matrix: 1024×1024, flip angle: 1°. The resulting images represented the data with frequency along the x-axis and time along the y-axis. In the analysis, the signal intensities along the y-axis were averaged to obtain a mean signal intensity for each frequency. For each situation, the ratio of the mean signal to the baseline signal was calculated to assess the presence of signals of certain frequencies.

SNR

SNR measurements were conducted using a water bottle phantom to investigate the influence of the presence and use of the afterloader on the MRI signals. The SNR was defined as the ratio of the mean value to the standard deviation of the signal intensity of a single voxel over time in repeated identical acquisitions [140]. A 2D dynamic spoiled gradient echo sequence (similar to the sequence for the source localization) was applied with the following parameters: TR/TE: 2.5/1.3 ms, FOV: 192×192 mm^2, acq. matrix: 96×96, slice thickness: 10 mm, flip angle: 30°, readout bandwidth: 1573 Hz/pixel, 100 dynamics.

The SNR of each pixel was calculated as [140]:

$$SNR(\vec{r}) = \frac{\underset{k=1...K}{\text{mean}}(S_N(\vec{r},k))}{\underset{k=1...K}{\text{stddev}}(S_N(\vec{r},k))}, \tag{4.1}$$

where mean() and stddev() denote the mean and standard deviation of the signal $S_N(\vec{r},k)$ of a single pixel at position $\vec{r}=(x,y)$ over time in repetition $k=1...K$.

To compute an average SNR for comparison of the SNRs in the different situations, an ROI of 11×11 pixels was drawn. The average SNR of the region of interest (ROI) was calculated as:

$$SNR_{ROI} = \underset{\vec{r}\in ROI}{\text{mean}}(SNR(\vec{r})), \tag{4.2}$$

with a standard deviation equal to stddev($SNR(\vec{r})$), assuming a negligible spatial signal variation within the ROI.

B_0 homogeneity

The influence of the presence of the afterloader on the main magnetic field was investigated by assessment of the B_0 homogeneity in a water bottle phantom. B_0 field maps were calculated using the phase images of a dual-echo 3D spoiled gradient echo sequence, with parameters equal to: TR/TE_1/TE_2: 40/10/15 ms, FOV: 192×192×64 mm^3, acq. matrix: 128×128×64, flip angle: 30°, readout bandwidth: 434 Hz/pixel, automatic shimming. The phase difference, $\Delta\varphi(\vec{r})$, between the two images acquired at two different echo times was defined as [60, 141]:

$$\Delta\varphi(\vec{r}) = \gamma\Delta B_0(\vec{r})TE_2 - \gamma\Delta B_0(\vec{r})TE_1 = \gamma\Delta B_0(\vec{r})\Delta TE, \tag{4.3}$$

where γ is the gyromagnetic ratio and $\Delta B_0(\vec{r})$ the field perturbation at position $\vec{r}=(x,y,z)$. To avoid the introduction of extra phase wraps, the phase difference maps were obtained from the product between the complex valued first image and the complex conjugate of the second image [142, 143]. The B_0 field maps, $\Delta B_0(\vec{r})$, were obtained from the phase difference maps, via:

$$\Delta B_0(\vec{r}) = \frac{\Delta\varphi(\varphi)}{\gamma\Delta TE}. \tag{4.4}$$

The homogeneity in the B_0 field maps (in ppm) was assessed and B_0 difference maps were calculated as the subtraction of the B_0 field of situation (i) from the B_0 field of situation (ii).

4.3 Results

4.3.1 Simultaneous MRI acquisition and afterloader employment

MRI acquisition was possible simultaneously with functioning of the prototype MR conditional afterloader. MR images were obtained, demonstrating no signs of detriment by visual inspection. Figure 3 demonstrates examples of both acquired slices for the two test cases of the afterloader. The figures present the MR artifact induced by the dummy source as well as the determined source position (overlaid in red). The other source positions found are also indicated in the presented images (overlaid in yellow), showing all detected source positions at regularly spaced distances along a straight line, in both cases. The distances of the source positions with respect to the first position are plotted in Figures 3c and 3f, also demonstrating that the determined source positions were found at regularly spaced distances. The average step sizes between the detected 3D positions for cases I and II were 9.9±0.2 mm and 4.9±0.2 mm respectively. These values corresponded with the applied step size settings of 10.0 mm and 5.0 mm. This confirmed that the afterloader was able to send the dummy source to the predefined dwell positions through the catheter with a fixed step size, simultaneously with MRI acquisition.

4.3.2 MRI performance

RF interference

The signals measured in the spurious signals tests are plotted in Figure 4 as the ratio of the average signal to the average baseline signal for all frequency ranges measured. Little differences were observed between the average signal and the baseline signal for the case where the afterloader was present and powered, but not connected to the treatment control system (blue in Fig. 4). When the afterloader was present and connected and when the afterloader was active, several peaks of increased signals were observed (red and yellow respectively in Fig. 4). However, maximum ratios of 1.2, 1.5 and 1.9 were obtained for situations (ii), (iii) and (iv) respectively. Accordingly, all peaks were below a ratio of 2, demonstrating maximum increases of received signals of less than twofold. This would not disturb the MR signal encoding process when a subject would be positioned in the scanner, since these signals received due to the afterloader are negligible (around noise level) compared to typical MRI signals (typical SNR values in MRI scans are around 30-100 depending on sequence parameters, field strength and tissue properties).

SNR

The images representing the SNR values for the four investigated situations are presented in Figure 5. The average SNR values (±standard deviation) of the ROIs were: Baseline:

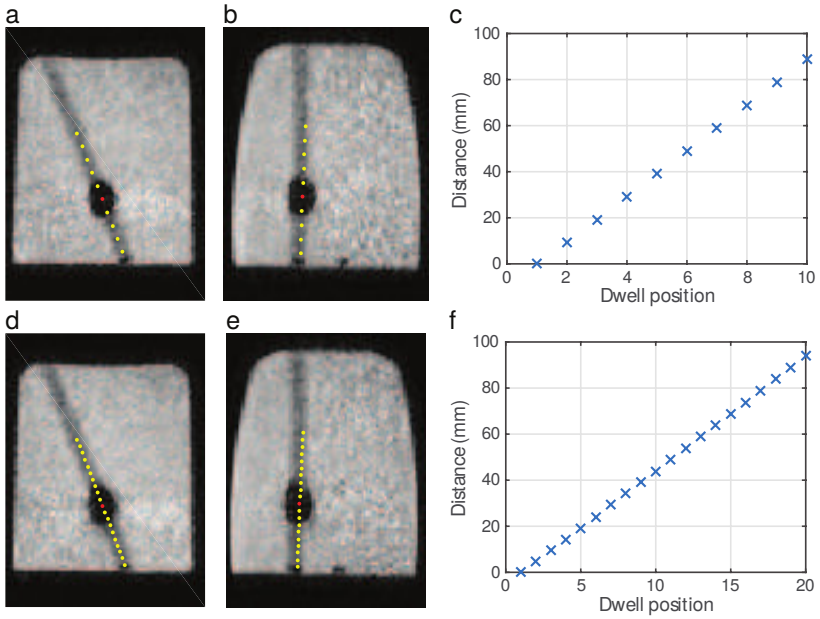

Figure 4.3 Examples of a sagittal slice in **(a)** and **(d)** and a coronal slice in **(b)** and **(e)** displaying the MR artifacts induced by the source for the case where the afterloader sent the source to 10 dwell positions with a 10 mm step size **(a-c)**, and to 20 dwell positions with a 5 mm step size **(d-f)**. The determined source positions for the depicted situations (position 5 in a-b and position 10 in d-e) are overlaid in red and the other positions found are overlaid in yellow. Figures **(c)** and **(f)** present the distances between the found positions and the first position (average step sizes of 9.9$\pm$0.2 mm and 4.9$\pm$0.2 mm respectively).

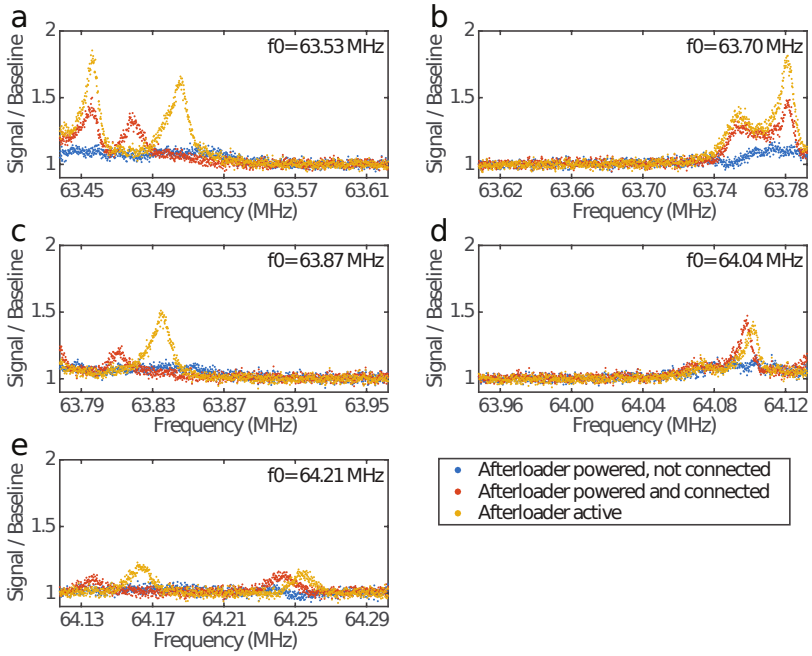

Figure 4.4 The ratio of the mean signal to the baseline signal versus frequency, for the five consecutive scans with different center frequencies: **(a)** f_0 = 63.53 MHz, **(b)** f_0 = 63.70 MHz, **(c)** f_0 = 63.87 MHz, **(d)** f_0 = 64.04 MHz, and **(e)** f_0 = 64.21 MHz. The graphs show the signals of the three investigated situations compared to the baseline signal without afterloader.

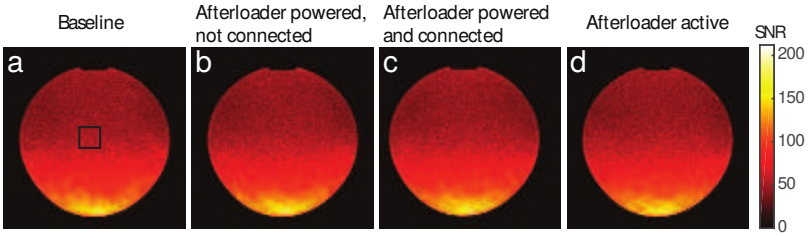

Figure 4.5 The SNR values for four different situations: **(a)** Baseline (no afterloader); **(b)** Afterloader powered, not connected; **(c)** Afterloader powered and connected to the treatment control system; **(d)** Afterloader active. Additionally, the baseline image **(a)** shows the position of the ROI (11×11 pixels) for calculation of average SNRs to compare the situations.

53.8 (±4.4); Afterloader powered, but not connected: 53.5 (±5.3); Afterloader powered and connected: 54.4 (±4.7); Afterloader active: 53.4 (±5.6). The SNR values presented in Figure 5 and the SNR values of the ROIs demonstrated that the SNR was not affected by the presence or functioning of the afterloader.

B_0 homogeneity

Figure 6 presents the B_0 maps obtained for the baseline situation without afterloader and for the situation where the afterloader was positioned next to the scanner. The images presented here were representative for all acquired slices. The B_0 maps showed no areas of distinct B_0 inhomogeneities. Furthermore, the B_0 difference maps showed no distinctions between the field maps with and without the afterloader (differences <0.1 ppm). Hence, the afterloader induced no significant distortions of the B_0 magnetic field that would disturb the MRI performance.

4.4 Discussion

This paper describes the testing of a prototype MR conditional HDR brachytherapy afterloader simultaneously with MR imaging. This has demonstrated the simultaneous functioning of both systems. MR imaging was possible while the afterloader sent the source to the dwell positions. Vice versa, the afterloader functioned correctly while acquiring MR images. The MRI performance tests proved that the MRI performance was not degraded by the afterloader. Accordingly, no deterioration of either system was discovered. These results have provided the evidence of a successful RF shielding in both directions.

This development of MR-guided HDR brachytherapy using an MR conditional afterloader enables large improvements of the clinical workflow. In current MR-guided HDR brachytherapy workflows, MRI has been incorporated into the processes of diagnosis, treatment planning, and/or pre- and post-irradiation imaging [19, 20, 22, 34, 35, 144, 145]. However, these

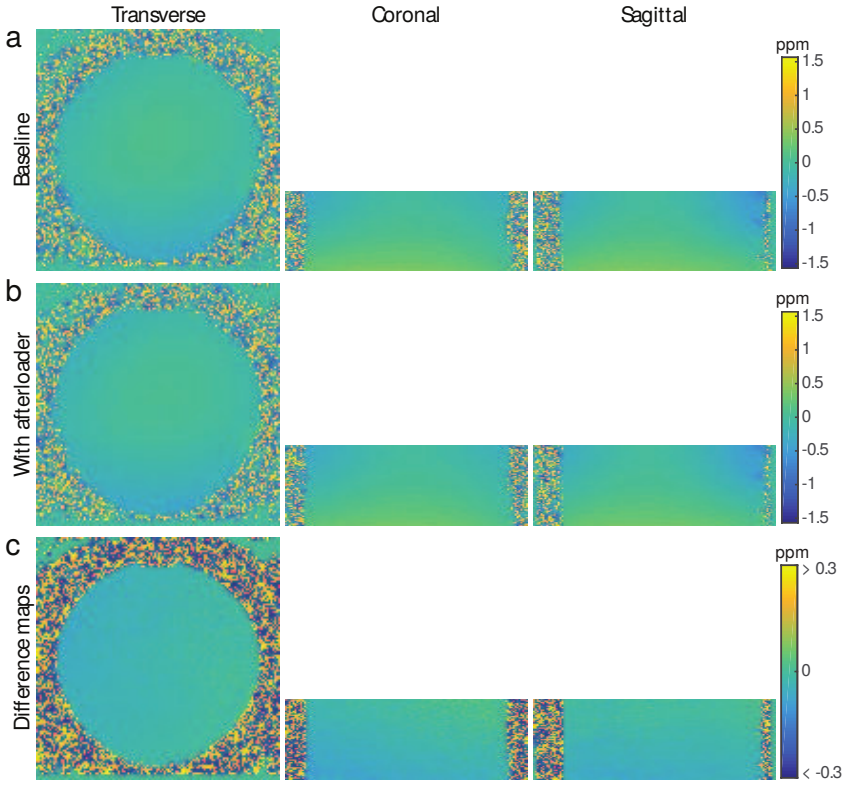

Figure 4.6 B_0 maps acquired in the center part of the phantom (left: transverse orientation, middle: coronal orientation, right: sagittal orientation) for two different situations: **(a)** Baseline (no afterloader); **(b)** Afterloader present. **(c)** Difference maps representing the subtraction of the B_0 field of the baseline situation from the B_0 field of the situation where the afterloader was present next to the scanner.

workflows necessarily require displacements of the patient between imaging/treatment planning and radiation delivery. On the other hand, when employing an MR conditional afterloader, the patient can stay inside the MR bore for the entire duration of anatomical imaging, reconstruction of the source positions, treatment planning and the actual dose delivery including treatment verification. No extra movements of the patient are necessary between reconstruction of the source positions and the irradiation process. Furthermore, reconstruction of the source positions can be automated employing a dummy source and an automatic source localization method as described here. The source positions found can then directly be used for treatment planning. These elements lead to an easier and faster workflow with less human interactions and a higher accuracy. Additionally, possible anatomy changes or errors can be detected such that the treatment can be interrupted if necessary.

In this study, the feasibility of an MR conditional afterloader has been tested. This afterloader is a prototype that needs adaptations before application in a clinical setting. A dummy source on a plastic cable, specifically made for testing purposes, was employed in this prototype. The current limitation to clinical introduction and the next step in the development process is to develop an MR conditional source cable. The requirements for an MR conditional source cable are that the material should be MR compatible, it should be flexible, strong, and stiff to send the source out to the correct position with a reliability at least equal to that of the steel cable, and the material should be resistant to the radiation emitted by the source. Furthermore, additional MR safety tests should be conducted to definitely exclude any possible safety risks.

This has been the first study to our knowledge that has focused on MR-based treatment verification of HDR brachytherapy and the consequential development of an MR conditional afterloader. This paper has demonstrated the feasibility of an MR conditional afterloader, facilitating the equipment to perform MR-based source localization. MR-based source localization using an MR conditional afterloader would highly improve the clinical workflow of HDR brachytherapy and it enables treatment verification, which currently has not been performed in clinical practice. Accordingly, this development might have an enormous impact on clinical practice.

4.5 Conclusion

The prototype MR conditional afterloader developed in this study and a commercial 1.5 T MRI scanner have been demonstrated to fully function while operating simultaneously. Neither system deteriorated functioning of the other system. In combination with a recently developed MR-based HDR source localization method, this enables real-time HDR source position verification for MR-guided HDR brachytherapy. This has shown the proof of concept of MR-based treatment verification of HDR brachytherapy.

Acknowledgments

The authors thank Sascha Krueger (Philips, Hamburg, Germany) for help with the spurious signals tests. This research was funded by the Eurostars Programme, ITEA3, project name: System of Real-Time Systems (SoRTS), project number: 12026.

Chapter 5

MRI artifact simulation for clinically relevant MRI sequences for guidance of prostate HDR brachytherapy

The following chapter is based on:

Ellis Beld, Marinus A. Moerland, Jochem R.N. van der Voort van Zyp, Max A. Viergever, Jan J.W. Lagendijk and Peter R. Seevinck

Submitted

Abstract

For the purpose of magnetic resonance imaging (MRI) guidance of prostate high-dose-rate (HDR) brachytherapy, this paper presents a study on the potential of clinically relevant MRI sequences to facilitate tracking or localization of brachytherapy devices (HDR source/titanium needle), and which could simultaneously be used to visualize the anatomy. The tracking or localization involves simulation of the MRI artifact in combination with a template matching algorithm. Simulations of the MRI artifacts induced by an HDR brachytherapy source and a titanium needle were implemented for four types of sequences: spoiled gradient echo, spin echo, balanced steady-state free precession (bSSFP) and bSSFP with spectral attenuated inversion recovery (SPAIR) fat suppression. A phantom study was conducted in which mentioned sequences (in 2D) as well as the volumetric MRI sequences of the current clinical scan protocol were applied to obtain the induced MRI artifacts for an HDR source and a titanium needle. Localization of the objects was performed by a phase correlation based template matching algorithm. The simulated images demonstrated high correspondences with the acquired MR images, and allowed localization of the objects. A comparison between the object positions obtained for all applied MRI sequences showed deviations (from the average position) of 0.2-0.3 mm, proving that all MRI sequences were suitable for localization of the objects, irrespective of their 2D or volumetric nature. This study demonstrated that the MRI artifact induced by an HDR source or a titanium needle could be simulated for the four investigated types of MRI sequences (spoiled gradient echo, spin echo, bSSFP and bSSFP-SPAIR), valuable for real-time object localization in clinical practice. This leads to more flexibility in the choice of MRI sequences for guidance of HDR brachytherapy and allows simultaneous object localization and visualization of the anatomy using a single MRI sequence.

5.1 Introduction

High-dose-rate (HDR) brachytherapy has developed into an effective treatment for prostate cancer [3–5]. Single-fraction HDR brachytherapy might become the treatment of choice for low and intermediate-risk disease [16] and has shown favorable results for salvage treatment of radiorecurrent prostate cancer [17, 18]. Magnetic resonance imaging (MRI) is the preferred and recommended imaging modality for guidance of high-dose-rate (HDR) brachytherapy [19–22]. MRI guidance is especially important because of the high dose delivered in a single fraction. MRI can be employed for either visualization or localization of interventional devices and brachytherapy tools as well as for providing good imaging contrasts of the patient's anatomy [25, 83, 134, 146]. Localization of an HDR source (or other paramagnetic devices) is possible by applying a method based on MRI artifact simulation combined with template matching between the simulated artifact and the MR image, where the location of the HDR source follows from the point of highest correlation [135]. However, the paper describing this method focused solely on detection of the source position and not on imaging of the surrounding structures. For clinical relevance, localization of the HDR source or an interventional needle should be possible simultaneously with providing good contrasts of the anatomy, ideally in a single MRI scan such that the HDR source and the anatomy are both imaged in the same frame of reference and without motion between imaging of both. Therefore, this paper focuses on the simulation of MRI artifacts for clinically relevant MRI sequences, intended for a template matching based object localization.

In the past years, considerable research has been conducted on MRI guidance for HDR brachytherapy or other interventions, e.g. the application of MRI-guided catheter insertion [19, 34]. Several groups investigated passive tracking techniques depending on signal intensity variations (either positive or negative contrasts) created by the interventional device [80–82, 84–86]. However, these techniques predominantly provide visualization of the objects in the MR images, but lack accurate localization of the object. Other groups have been working on active tracking techniques [90–92], but these techniques require substantial hardware adaptations and cause additional safety concerns.

To be able to perform automatic localization leading to an accurate position of the HDR brachytherapy source, we have been working on MR-based source localization using MRI artifact simulation combined with a template matching algorithm. The MRI sequence that has been applied for MR-based HDR source localization was a spoiled gradient echo sequence [135]. Gradient echo sequences are generally fast and therefore suitable for source or needle tracking. Furthermore, the simulation of the MRI artifact was known for this type of sequences. However, the T1-weighted contrast of a spoiled gradient echo sequence with a short echo time (TE) and a short repetition time (TR) provides no sufficient contrast for a detailed visualization and delineation of the prostate. In current clinical practice, a multiparametric MRI exam is utilized for delineation of the volumes for pre-treatment planning. During the interventional procedure, after catheter insertion, a T2-weighted scan is made using a turbo spin echo sequence for delineation of the anatomy at that moment, see Figure 5.1a for an example image. This type of sequence provides a good contrast to distinguish

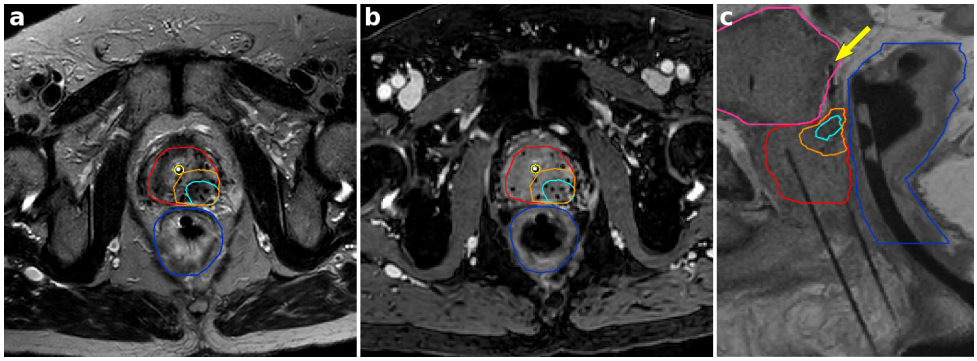

Figure 5.1 MR images of the prostate acquired after catheter insertion using the MRI sequences currently provided in the clinical scan protocol: **(a)** a T2-weighted turbo spin echo sequence, **(b)** a bSSFP-SPAIR sequence and **(c)** a T1-weighted turbo spin echo sequence. The brachytherapy catheters are visible as signal voids, and the delineations indicate the prostate (red), the gross tumor volume (GTV, light blue), the clinical target volume (CTV, orange), the urethra (yellow), the rectum (dark blue), and the bladder (pink). The yellow arrow in c points at an example of a catheter tip outside the prostate tissue, generally better visible on the T1-weighted scan than with the contrast of a bSSFP sequence.

the prostate with its different zonal areas, and frequently the tumor and critical structures can be visualized as well [25]. On the contrary, T2-weighted spin echo sequences are less valuable for visualization of the brachytherapy catheters. Accordingly, an additional balanced steady state free precession sequence with fat suppression (spectral attenuated inversion recovery, SPAIR) is applied during the treatment, to provide sufficient contrast to visualize the prostate as well as the positions of the brachytherapy catheters inserted into the prostate, see Figure 5.1b. Lastly, a T1-weighted turbo spin echo sequence is applied to visualize and check the tips of catheters that end in the tissue outside the prostate, see Figure 5.1c. These catheter tips are generally more difficult to reconstruct accurately with the contrast of a bSSFP scan. The T1-weighted scan provides a better contrast between the catheter and tissue, while the contrast between different tissue types is rather low.

In this paper, the potential of simulation of the MRI artifacts induced by an HDR brachytherapy source or needle was investigated for several types of clinically relevant MRI sequences. The simulated MRI artifacts serve to be applied in a template matching algorithm for localization of the source or needle. The aim is to obtain MRI sequences which facilitate both real-time tracking or localization of brachytherapy devices as well as visualization of the anatomy, for application during the interventional procedure of HDR brachytherapy. This generates flexibility in the choice of an MRI sequence for guidance of HDR brachytherapy. A spoiled gradient echo sequence, a spin echo sequence, and a balanced steady-state free precession (bSSFP) sequence were taken into account, as well as the effect of including a fat suppression technique in the bSSFP sequence. The paper describes the simulation of the MRI artifacts for these four types of sequences for two objects used in HDR brachytherapy: an HDR brachytherapy source and a titanium needle. A phantom study was performed to

acquire the MRI artifacts for the HDR source and the needle. Next, the simulated images are evaluated qualitatively by visual comparison with the MR images. For a quantitative evaluation, the simulated images are exploited in the template matching algorithm for object localization and the results are evaluated by a comparison of the obtained object positions for all applied MRI sequences.

5.2 Methods

5.2.1 Simulations

All simulations were performed in Matlab (The Mathworks, Natick, Massachusetts, United States). The simulations were performed as also explained in Beld *et al* [135]. The steps in this simulation involve simulation of the object geometry, definition of the susceptibility distribution, calculation of the induced magnetic field perturbation and, lastly, the inclusion of the MRI sequence (with its corresponding MRI signal equation) and k-space sampling. More details on the separate steps are given in the paragraphs below.

Object simulation

Two objects used in HDR brachytherapy were simulated: an HDR brachytherapy source and a titanium needle (more information is given below). 3D geometry models of the objects were generated on a cubic grid with 0.1 mm isotropic resolution. Each part of the object was assigned the susceptibility value corresponding with the material. The borders of the objects were smoothed, to take into account partial volume voxels. The objects were simulated inside an environment of water, which was assigned a susceptibility value of χ_{water} = -9.1 ppm [62].

HDR source A 3D model of a Flexisource Ir-192 HDR source (Elekta NL, Veenendaal, The Netherlands) was constructed. The source was modeled as a cylinder of iridium (radius = 0.30 mm, length = 3.55 mm), surrounded by a steel capsule (radius = 0.45 mm, length = 4.4 mm), connected to a steel cable (radius = 0.25 mm, infinite length), schematically depicted in figures 5.2a and 5.2b. The susceptibility values assigned were: χ_{steel} = $1.2{\cdot}10^4$ ppm for steel (empirically derived), and $\chi_{iridium}$ = 36.6 ppm for iridium [63].

Needle A simplified model of the needle (a 1.9 mm diameter trocar needle; Elekta NL, Veenendaal, The Netherlands) was generated, see figures 5.2c and 5.2d. In this model, the tip was simplified as a cone shape instead of the three flattened surfaces of the actual needle geometry. Between the cone-shaped tip and the hollow tube, the needle contains a solid part of titanium, which is important to note as this affects the shape of the MRI artifact. The needle had an outer radius of 0.95 mm and an inner radius of 0.75 mm. The susceptibility values assigned were: $\chi_{titanium}$ = 182 ppm for titanium and χ_{air} = 0.36 ppm for air [62].

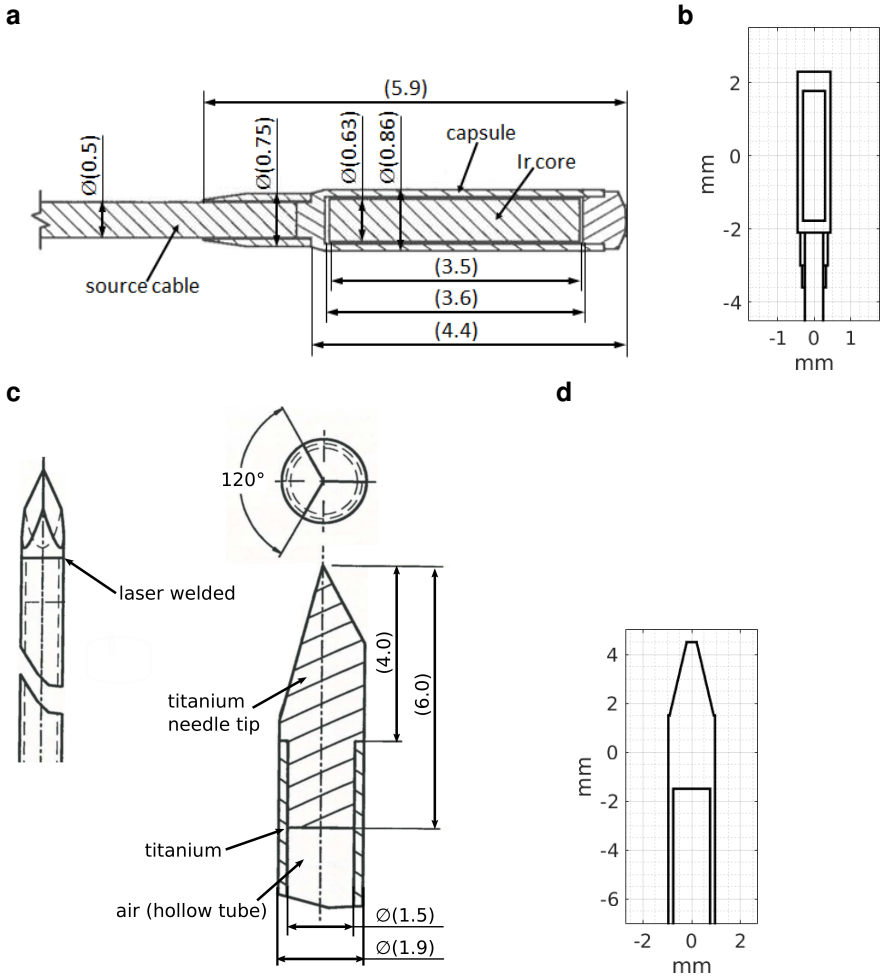

Figure 5.2 (a) Drawing (cross-section) of the Flexisource Ir-192 HDR source (dimensions in mm), and **(b)** the geometry model (cross-section) of the HDR source as implemented in the MR artifact simulations. **(c)** Drawing (dimensions in mm) and **(d)** geometry model (cross-section) of the tip of the titanium needle.

Magnetic field perturbation

The magnetic field perturbation (ΔB_0) was calculated based on the susceptibility distribution obtained by assigning the susceptibility values to the parts of the modeled object. This calculation was accomplished by a forward calculation of the susceptibility induced field shift, applying a Fourier-based convolution method in combination with virtual zero-padding [69]. This involves a convolution between the 3D susceptibility distribution and a dipole kernel (defined as the Green's function), followed by a subtraction of the aliasing field disturbance.

MRI sequence

The last step of the simulations involves the inclusion of the MRI sequence and k-space sampling. Four types of MRI sequences were taken into account: a spoiled gradient echo sequence, a spin echo sequence, a bSSFP sequence and a bSSFP sequence including SPAIR fat suppression. Simulation of a spoiled gradient echo sequence was performed as also described earlier [78, 135]. Here, the equation for the simulation of a gradient echo type of sequence was regarded as the basic equation, and modifications to this equation were made to simulate the other types of sequences.

Spoiled gradient echo sequence Simulation of a spoiled gradient echo sequence involves the simulation of the off-resonance effects inducing the susceptibility artifact in the MR image, related to differences in phase evolution of the individual spins. Two main components contribute to the differences in phase evolution of the spins: the local field inhomogeneity and the frequency encoding gradient. In the presence of a strong field inhomogeneity, the phase of the individual spins changes considerably over time during the sampling time as well as spatially within a voxel. These effects induce signal shifts along the readout direction and intravoxel dephasing respectively.

To simulate the MRI artifact, the spin distribution, $\rho(x, y, z)$, the magnetic field perturbation, $\Delta B_0(x, y, z)$, and the following scan parameters of the MR sequence were taken into account: the echo time, TE, the field of view, FOV, and the sampling interval, Δt. Multiple isochromats per voxel were simulated, e.g. 10·10·100=10^4 isochromats per voxel for an image with 1 mm in-plane resolution and a slice thickness of 10 mm. The effect of T2 decay was neglected since this has no spatially varying impact. For a readout direction along x, the signal for each k_x (at a certain time point during sampling), $S(k_x, y, z)$, was calculated as the sum over all spin isochromats along x, all representing the signal of the spin at that point in time [71, 78, 135]:

$$S(k_x, y, z) = \sum_{j=1}^{N_x} \rho(x_j, y, z) \cdot \mathrm{e}^{i2\pi\gamma\Delta B_0(x_j,y,z)\cdot(TE+n\Delta t)} \cdot \mathrm{e}^{-i2\pi k_x x_j}, \tag{5.1}$$

where $k_x = \gamma G_R n \Delta t$, γ is the gyromagnetic ratio, G_R is the readout gradient strength defined as $G_R = \frac{1}{\gamma FOV_x \Delta t}$, and $n = -N_x/2...N_x/2 - 1$ with N_x the number of spin

isochromats along the x direction (readout direction). The complex-valued MR signal in image domain, $S(x, y, z)$, was calculated as the 1D inverse Fourier transform along the x-direction:

$$S(x, y, z) = \mathcal{F}^{-1}(S(k_x, y, z)). \tag{5.2}$$

The final step was the complex summation of multiple isochromats to resample $S(x, y, z)$ to a 2D image or 3D volume with a larger voxel size matching with the voxel size of the MRI acquisition, and to take into account intravoxel phase dispersion.

Equation 5.1 consists of three main terms: the magnetization/spin distribution, $\rho(x_j, y, z)$, a field inhomogeneity term, $\mathrm{e}^{i2\pi\gamma\Delta B_0(x_j,y,z)\cdot(TE+n\Delta t)}$, and a term for spatial encoding, $e^{-i2\pi k_x x_j}$. The field inhomogeneity term in its turn contains two effects: spatial dephasing due to off-resonance effects in a gradient echo sequence, $e^{i2\pi\gamma\Delta B_0(x_j,y,z)\cdot TE}$, and phase evolution over time during sampling in the readout process, $e^{i2\pi\gamma\Delta B_0(x_j,y,z)\cdot n\Delta t}$. The other types of sequences were simulated by modifying parts of equation 5.1 as described in the paragraphs below.

Spin echo sequence To simulate the MRI artifact for a spin echo sequence, a modification to the field inhomogeneity term of equation 5.1 was made to account for the basic difference between a gradient echo type of sequence and a spin echo type of sequence. This basic difference is the fact that a spin echo sequence applies a 180° refocusing pulse that will rephase the spins dephased due to off-resonance effects, while a gradient echo sequence shows severe dephasing effects due to off-resonance spins. In the field inhomogeneity term, the dephasing effect of a gradient echo sequence was removed such that the field inhomogeneity term only accounted for the phase evolution over time during the sampling process: $e^{i2\pi\gamma\Delta B_0(x_j,y,z)\cdot n\Delta t}$ [71]. Then, the signal for each k_x, $S(k_x, y, z)$, for a spin echo sequence is equal to:

$$S(k_x, y, z) = \sum_{j=1}^{N_x} \rho(x_j, y, z) \cdot \mathrm{e}^{i2\pi\gamma\Delta B_0(x_j,y,z)n\Delta t} \cdot \mathrm{e}^{-i2\pi k_x x_j}. \tag{5.3}$$

Balanced steady-state free precession For the simulation of a bSSFP sequence, the first term of equation 5.1 was modified, i.e. the magnetization/spin distribution term, $\rho(x, y, z)$. While the transverse magnetization gets spoiled in a spoiled gradient echo sequence, no spoiling is applied in a bSSFP sequence and each RF pulse acts on both the remaining transverse and longitudinal magnetization. In a multi-pulse sequence, the magnetization approaches a steady state after sufficient RF pulses. The steady state magnetization in a bSSFP sequence is spatially dependent on ΔB_0 due to off-resonance effects and, therefore, the steady state magnetization should be included in the signal equation for simulation of the MRI artifact. The steady state magnetization at each TR of a balanced sequence has been described by a series of equations [147], starting by decomposing the equation for the transverse magnetization M_{xy} into its x and y components (M_x and M_y):

$$M_{xy}(x, y, z) = M_x(x, y, z) + iM_y(x, y, z). \tag{5.4}$$

These x and y components of the magnetization are described by:

$$M_x(x,y,z) = M_0(1-E_1)\frac{\sin\alpha(1-E_2\cos\beta)}{d}, \tag{5.5}$$

and

$$M_y(x,y,z) = M_0(1-E_1)\frac{E_2\sin\alpha\sin\beta}{d}, \tag{5.6}$$

where the following definitions hold:

$$E_1 = \mathrm{e}^{-TR/T_1}, \tag{5.7}$$

$$E_2 = \mathrm{e}^{-TR/T_2}, \tag{5.8}$$

$$d = (1-E_1\cos\alpha)(1-E_2\cos\beta) - E_2(E_1-\cos\alpha)(E_2-\cos\beta), \tag{5.9}$$

where M_0 is the equilibrium magnetization, α is the flip angle (in radians), β is the resonance offset angle (in radians), and TR is the repetition time. The resonance offset angle β is described as:

$$\beta = 2\pi(\delta_{CS} + \gamma\Delta B_0(x,y,z))\cdot TR - \phi_{RF}, \tag{5.10}$$

where δ_{CS} is the chemical shift (in hertz) which is equal to zero for water/tissue, $\gamma\Delta B_0$ is the off-resonance (in hertz), and ϕ_{RF} is the RF phase increment (in radians) in successive TRs ($\phi_{RF} = \pi$ was the default setting for a bSSFP sequence as applied in this study). Thus, ΔB_0 has an impact in the β term (the resonance offset angle) of the steady state signal equation of a bSSFP sequence.

To simulate the MRI artifact for the bSSFP sequence, the spin distribution $\rho(x,y,z)$ was replaced by the bSSFP steady state signal, $M_{xy}(x,y,z)$, described above (equation 5.4):

$$S(k_x,y,z) = \sum_{j=1}^{N_x} M_{xy}(x_j,y,z)\cdot \mathrm{e}^{i2\pi\gamma\Delta B_0(x_j,y,z)\cdot(TE+n\Delta t)}\cdot \mathrm{e}^{-i2\pi k_x x_j}. \tag{5.11}$$

Balanced steady-state free precession with SPAIR For a bSSFP sequence that includes SPAIR fat suppression, equation 5.11 for the simulation of the MRI artifact of a bSSFP sequence was implemented and the effect of an inversion recovery pulse at the fat frequency was taken into account. This was accomplished by selecting the spins with a frequency within the bandwidth of the adiabatic inversion pulse, and setting these spins to zero in the matrix representing the steady-state signal, $M_{xy}(x,y,z)$. This meant that the spins between -1.8 and -5.2 ppm (i.e. -3.5±1.7 ppm) were set to zero in case of a SPAIR pulse with a frequency offset of 110 Hz as applied in this study.

Table 5.1 The scan parameters for the spoiled gradient echo sequence, the spin echo sequence, the bSSFP sequence and the bSSFP-SPAIR sequence that were applied (all 2D sequences).

	Spoiled gradient echo	Spin echo	bSSFP	bSSFP-SPAIR
TE/TR (ms)	2.26/4.60	10.0/100.0	2.3/4.5	1.9/3.8
FOV (mm^2)	256×256	256×256	256×256	256×256
Slice thickness (mm)	10.0	10.0	10.0	10.0
Acquisition matrix	256×256	256×256	256×256	256×256
Flip angle	30°	90°	20°	30°
Readout bandwidth (Hz/pixel)	434	158.8	434	775

5.2.2 MRI acquisition

Phantom measurements

A non-active Ir Flexisource (Elketa NL, Veenendaal, The Netherlands) and a 1.9 mm diameter titanium trocar needle (Elekta NL, Veenendaal, The Netherlands) were used in a phantom experiment, see figures 5.2a and 5.2c for schematic depictions of both objects. Phantom measurements were conducted using a water phantom (doped with $MnCl_2$) in which the object to be scanned (either the HDR source or the needle) was affixed on a platform, where the tip of the object was positioned in the center of a circular gap in the platform such that the object was surrounded by signal generating molecules. In the case of the HDR source, a plastic tube was affixed on the platform in which the HDR source was inserted.

MR imaging was performed on a 1.5 T Ingenia MRI system (Philips Healthcare, Best, The Netherlands), using a 28-channel anterior/posterior coil. Two imaging approaches were distinguished: (I) fast 2D imaging sequences for (real-time) tracking, and (II) clinically applied 3D/volumetric imaging sequences for robust object localization and position verification. The following types of 2D MRI sequences were applied: a spoiled gradient echo sequence, a spin echo sequence, a bSSFP sequence, and a bSSFP sequence including SPAIR fat suppression, see Table 5.1 for the sequence parameters. In each case, two intersecting 2D slices were scanned to be able to obtain the 3D object position. Regarding the 3D/volumetric imaging, the MRI sequences currently provided in the clinical scan protocol of the prostate HDR brachytherapy intervention were applied. These sequences involve a 3D bSSFP-SPAIR sequence, a T2-weighted and a T1-weighted turbo spin echo sequence (both multi-slice 2D), see Table 5.2 for the sequence parameters.

During MRI acquisition, the phantom was subsequently positioned at two different angulations in the MRI scanner such that the long axis of HDR source or needle was oriented in two different orientations, as follows:

(i) Parallel with the main magnetic field $\vec{B}_0$, i.e. at an angle of 0°,

(ii) At an angle of 20° with respect to $\vec{B}_0$.

Table 5.2 The scan parameters for the 3D bSSFP-SPAIR sequence, the multi-slice 2D T2-weighted turbo spin echo (T2w spin echo) sequence and the multi-slice 2D T1-weighted turbo spin echo (T1w spin echo) sequence that were applied (as provided in the current clinical scan protocol for prostate HDR brachytherapy).

	bSSFP-SPAIR	T2w spin echo	T1w spin echo
TE/TR (ms)	1.76/3.52	110.0/7126.5	37.4/2000.0
FOV (mm^3)	256×256×120	200×200×119	224×224×70
Reconstructed resolution (mm^3)	1.0×1.0 ×1.0	0.5×0.5×3.0	1.0×1.0×2.0
Flip angle	30°	90°	90°
Readout bandwidth (Hz/pixel)	935.9	194.5	539.1

5.2.3 Evaluation

For a qualitative evaluation of the simulations, the simulated MRI artifacts were compared with the acquired MR images by visual inspection. The similarity between the simulated and the acquired MRI artifacts was assessed by visual inspection. This was conducted for all applied sequences, for both objects and object orientations.

For a quantitative evaluation of the simulations and their value for object localization, a template matching procedure [127] was performed to determine the object position. This template matching was based on a subpixel phase correlation algorithm as previously described [135] for the 2D MRI acquisitions. For the 3D data sets (either 3D or multi-slice 2D), the subpixel phase correlation algorithm was extended to a 3D algorithm. Due to the large memory required for the 3D subpixel template matching (large matrices), a smaller volume within the full 3D data set (the central area of the phantom) was selected before applying the phase correlation algorithm.

The simulated and the obtained object positions were overlaid on the simulated and acquired MR images respectively to visually evaluate the quality of the template matching. To obtain absolute object positions (with respect to the MRI scanner's isocenter), the positions were corrected for the offcenter position of the FOV of the MRI acquisition, allowing a comparison between the positions obtained from different MRI sequences. Additionally, the average object position (of seven obtained positions) and the mean deviation from this average were calculated to quantify the variation between the object positions found. The comparison of the obtained object positions was utilized as a means to evaluate the value of each applied MRI sequence for localization of the object.

5.3 Results

5.3.1 Simulations

The simulated MRI artifacts (magnitude and phase images) obtained by simulating a gradient echo sequence, a spin echo sequence, a bSSFP sequence and a bSSFP sequence with SPAIR fat suppression are presented in figures 5.3, 5.4, 5.5 and 5.6 respectively for an HDR brachytherapy source and a titanium needle (with the object positions overlaid on the images). Besides the simulations, these figures also present the acquired MR images. A qualitative comparison (i.e. visual inspection) demonstrated that the simulated images highly corresponded with the acquired MR images for the investigated sequences, except for a few small variations in the phase images. These variations were observed mainly for the bSSFP and the bSSFP-SPAIR sequence, and might be caused by either B_0 variations or the fact that the simulation of the fat suppression was implemented as an ideal situation. However, these variations were not considered as a severe hurdle that would prevent or deteriorate localization of the objects. This demonstrated that the MRI artifacts for the different types of MR sequences could be simulated as described in this paper for both the HDR brachytherapy source and the titanium needle.

5.3.2 Object localization

Besides the simulation results, figures 5.3, 5.4, 5.5 and 5.6 also present the determined object positions obtained by the phase correlation algorithm (object contours overlaid in red on the MR images). Visual inspection indicated that the obtained object positions within the artifacts corresponded to the simulated object positions (object contours overlaid in yellow on the simulated images).

Table 5.3 provides the object positions in the MRI scanner coordinate system (in mm) obtained for the four different cases (two objects and two angulations) for all seven MRI sequences applied (four types of 2D MRI acquisitions, one 3D acquired volume and two volumetric multi-slice 2D acquired volumes). This showed that object localization in all assessed MRI sequences led to nearly identical object positions in all cases. Additionally, Table 5.3 reports the mean deviation of the object positions from the average position. The mean deviations of 0.2-0.3 mm confirmed that small subvoxel variations were found between the object positions for the varying MRI sequences. This proved that the artifacts of the source and needle could be simulated for all investigated MRI sequences and applied for determination of the object position using a phase correlation template matching algorithm. Accordingly, these results demonstrated that all investigated MRI sequences were suitable for localization of the objects.

Table 5.3 The obtained object positions for the HDR brachytherapy source (top part) and the titanium needle (bottom part) at angulations of 0° and 20°. The positions are provided as coordinates in right-left (RL), feet-head (FH) and anterior-posterior (AP) directions (in mm). In each case, a position is provided for the four 2D MRI sequences applied, the 3D bSSFP-SPAIR sequence and the multi-slice 2D T2 weighted (T2w) and T1 weighted (T1w) spin echo sequences. The bottom row of each part shows the mean deviation (and range) in mm from the average position.

HDR source		**0°**			**20°**		
Matching type	Sequence type	RL (mm)	FH (mm)	AP (mm)	RL (mm)	FH (mm)	AP (mm)
2D	Gradient echo	1.2	-1.3	25.2	0.9	-0.9	25.2
	Spin echo	1.1	-1.4	25.3	0.8	-0.7	25.3
	bSSFP	1.1	-1.5	25.2	0.9	-1.0	25.2
	bSSFP-SPAIR	1.2	-1.4	25.2	0.9	-1.0	25.2
3D	bSSFP-SPAIR	1.0	-1.3	25.2	0.7	-1.0	25.2
	T2w spin echo	1.1	-1.1	25.3	0.7	-1.1	25.4
	T1w spin echo	1.2	-1.1	25.1	0.6	-0.6	25.1
	Mean deviation	0.2 (0.1-0.2)			0.2 (0.1-0.4)		
Needle		**0°**			**20°**		
Matching type	Sequence type	RL (mm)	FH (mm)	AP (mm)	RL (mm)	FH (mm)	AP (mm)
2D	Gradient echo	4.1	-14.9	20.8	3.3	-15.3	20.6
	Spin echo	4.1	-14.6	20.6	3.1	-15.1	20.7
	bSSFP	4.2	-14.8	20.7	3.3	-15.1	20.5
	bSSFP-SPAIR	4.1	-14.9	20.5	3.2	-15.3	20.6
3D	bSSFP-SPAIR	4.3	-14.8	20.6	3.4	-15.2	20.7
	T2w spin echo	3.9	-15.2	20.2	3.3	-15.1	20.2
	T1w spin echo	4.2	-15.1	20.9	3.3	-15.1	20.7
	Mean deviation	0.3 (0.1-0.6)			0.2 (0.1-0.4)		

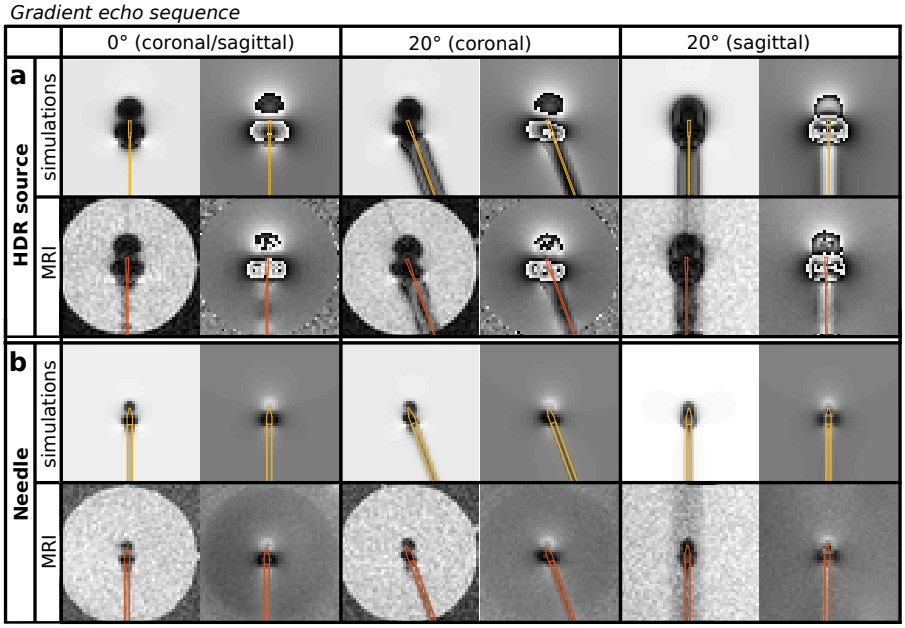

Figure 5.3 The simulated images (top rows) and the acquired MR images (bottom rows) of a spoiled gradient echo sequence for **(a)** the HDR brachytherapy source and **(b)** the titanium needle. The images present the magnitude (left) and phase (right) representations. The left column shows an angulation of 0°, and the middle and right column show the coronal and sagittal slices respectively for an angulation of 20°. The contours of the simulated and acquired object positions are overlaid in yellow and red respectively.

5.4 Discussion

This paper has demonstrated the feasibility of localization of an HDR source or needle for fast 2D MRI sequences as well as for clinically applied volumetric MRI sequences. The simulation of the MRI artifacts induced by an HDR source or needle was proposed for a gradient echo sequence, a spin echo sequence and a bSSFP sequence (either with or without SPAIR fat suppression). These simulations are valuable for localization of the object using a phase correlation based template matching. The results have demonstrated that all investigated MRI sequences were suitable for object localization in this phantom study, where mean deviations from the average object position of 0.2-0.3 mm were found. Additionally, current clinical practice has shown that bSSFP-SPAIR and T2-weighted spin echo sequences provide detailed images visualizing the prostate and its surrounding anatomy, on which the radiation oncologist is able to delineate the target and organs at risk. Therefore, this research has proven the feasibility of localization of an HDR source or needle using MRI sequences for which clinical results have shown that the prostate and the organs at risk can be visualized. The next step required is to confirm these results in a patient study by investigating both aims

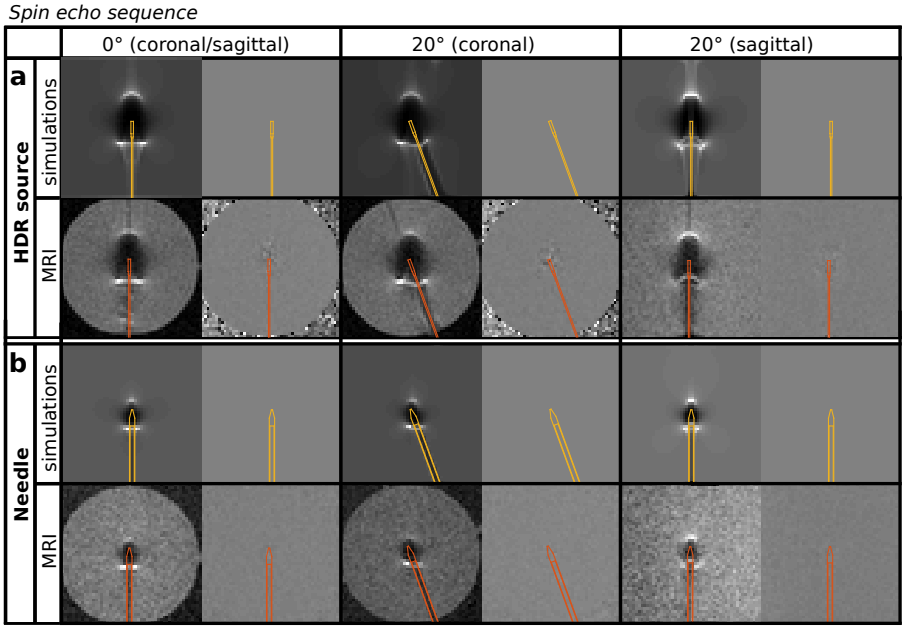

Figure 5.4 The simulated images (top rows) and the acquired MR images (bottom rows) of a spin echo sequence for **(a)** the HDR brachytherapy source and **(b)** the titanium needle. The images present the magnitude (left) and phase (right) representations. The left column shows an angulation of 0°, and the middle and right column show the coronal and sagittal slices respectively for an angulation of 20°. The contours of the simulated and acquired object positions are overlaid in yellow and red respectively.

simultaneously in one scan: localization of an HDR source or needle as well as visualization of the prostate.

The inclusion of different types of MRI sequences in the simulation of the MRI artifacts is of high importance for a clinical application of localization/tracking of HDR brachytherapy interventional objects by a template matching approach. In previous studies, the simulation of the MRI artifacts was described for a spoiled gradient echo sequence [78, 135]. However, a spoiled gradient echo sequence provides no sufficient contrasts for a clear visualization of the anatomy and for delineation of the tumor and organs at risk. This would mean that two separate scans would be required: one scan for visualization of the anatomy and one scan for localization of the interventional object. When determining the object position in a separate scan from the scan on which the delineations are being made, motion could lead to changes of the prostate and object positions in the time between the acquisitions of the two scans. This motion corrupts the treatment planning or dose calculations for treatment verification. The major advantage of the results presented here is the ability to simulate the MRI artifacts for clinically relevant MRI sequences, which enables localization of an HDR source or needle as well as visualization of the anatomy (for delineation or tracking) in a single MRI scan.

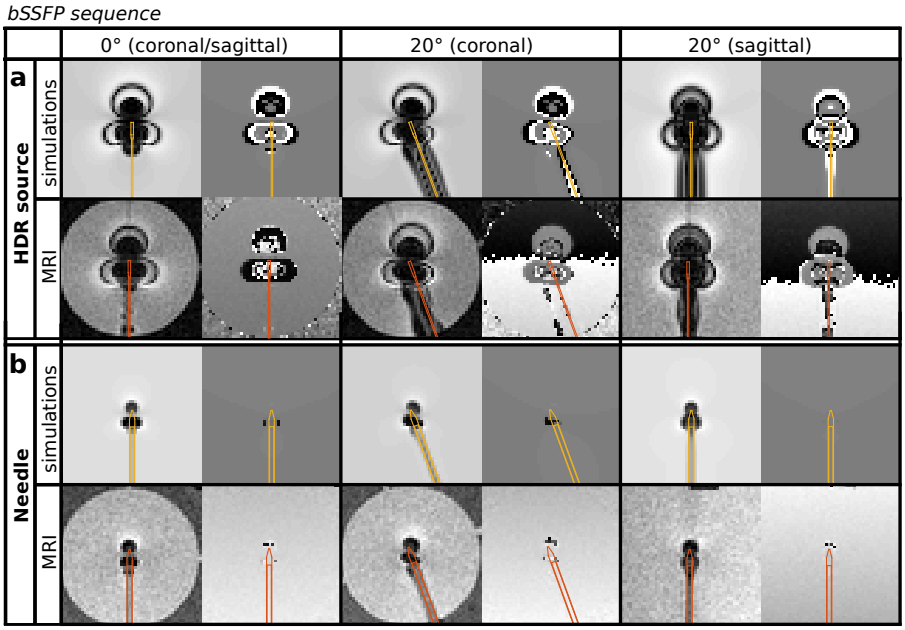

Figure 5.5 The simulated images (top rows) and the acquired MR images (bottom rows) of a bSSFP sequence for **(a)** the HDR brachytherapy source and **(b)** the titanium needle. The images present the magnitude (left) and phase (right) representations. The left column shows an angulation of 0°, and the middle and right column show the coronal and sagittal slices respectively for an angulation of 20°. The contours of the simulated and acquired object positions are overlaid in yellow and red respectively.

Accordingly, the object position can be determined with respect to the position of the prostate and the tumor, which is necessary to achieve a clinical impact.

The simulations demonstrated in this paper are valuable for the development of (real-time) MRI guidance of HDR brachytherapy. Two important applications are source position reconstruction for treatment planning and source localization for real-time treatment verification. This can be realized when combined with an MR compatible afterloader allowing simultaneous dose delivery and MR imaging [148]. Additionally, a robot for robotic MRI-guided needle insertion is in development in our department [95]. Also this is an important application where the simulations described here might play an essential role in real-time tracking of the needle during insertion. Lastly, a potential application outside the scope of HDR brachytherapy is to use the proposed simulations in combination with the phase correlation algorithm for the localization of gold fiducial markers for an accurate patient positioning in external beam radiotherapy, as has also been described for spoiled gradient echo sequences solely [149]. For these applications, the ability to simulate different types of MRI sequences facilitates an easier practice of object localization by not being restricted to the use of a spoiled gradient echo sequence. Hence, this work provides flexibility in the choice of MRI sequences during

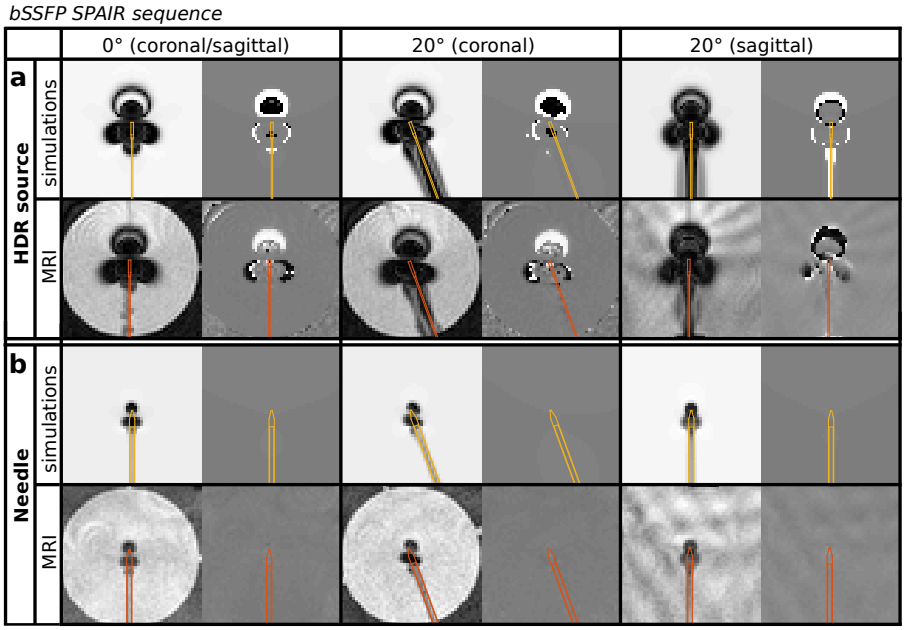

Figure 5.6 The simulated images (top rows) and the acquired MR images (bottom rows) of a bSSFP sequence with SPAIR fat suppression for **(a)** the HDR brachytherapy source and **(b)** the titanium needle. The images present the magnitude (left) and phase (right) representations. The left column shows an angulation of 0°, and the middle and right column show the coronal and sagittal slices respectively for an angulation of 20°. The contours of the simulated and acquired object positions are overlaid in yellow and red respectively.

an MRI-guided HDR brachytherapy procedure where tracking of an HDR source or needle is desired.

5.5 Conclusion

This paper has demonstrated the simulation of the MRI artifacts induced by an HDR brachytherapy source as well as a titanium needle for a spoiled gradient echo sequence, a spin echo sequence, a bSSFP sequence and a bSSFP sequence including SPAIR fat suppression. These simulations, in combination with a template matching algorithm, enable localization of an HDR source and a titanium needle for fast 2D MRI sequences as well as for clinically applied volumetric MRI sequences. This shows the feasibility of localization of HDR brachytherapy interventional devices for clinically relevant MRI sequences, enabling object localization and visualization the prostate and organs at risk (for delineation or tracking) on a single MRI scan. Hence, this paper has paved the way towards: (1) real-time device tracking (2) for a range of clinically relevant MRI sequences, and (3) simultaneously visualizing the target and critical structures.

Acknowledgments

This research was funded by the Eurostars Programme, ITEA3, project name: System of Real-Time Systems (SoRTS), project number: 12026.

Chapter 6

Summary & general discussion

6.1 Summary

MR imaging provides superior tissue contrast and is therefore applied in HDR brachytherapy. MRI is currently applied for manual catheter reconstruction and treatment planning. However, techniques for real-time treatment verification are not clinically available. MRI may be an ideal imaging modality for real-time guidance and verification of the treatment, as it allows visualization of the anatomy as well as visualization/detection of interventional devices. We have proposed an MR-guided HDR brachytherapy workflow in which we apply MR-based source localization for reconstruction of the source dwell positions and for real-time treatment verification. This required an investigation of the impact of the magnetic field on the dose distribution, the development of an MR conditional afterloader and a method for MR-based source tracking/object localization and simultaneous visualization of the anatomy. This thesis has described the main technical developments necessary for real-time MRI guided HDR brachytherapy.

In a situation where real-time treatment verification is applied, the patient needs to be positioned inside the MRI scanner at the moment of irradiation. In **Chapter 2**, the impact of the MRI scanner's magnetic field on the dose distribution was investigated. A magnetic field causes deflection of electrons in the plane perpendicular to the magnetic field, and leads to less lateral scattering along the direction parallel with the magnetic field. Monte Carlo simulations were conducted to investigate the influence of the magnetic field on the dose distribution around an HDR brachytherapy source (Ir-192) for magnetic field strengths of 1.5 T, 3 T and 7 T. The results demonstrated that the dose distribution was nearly unaffected by the magnetic field for all considered field strengths, with differences below or around the level of the statistical error (i.e. around 1.7% at 10 mm from the source). However, careful attention should be paid to dose perturbation in the case of air pockets near the source. In conclusion, from a dose perspective, HDR brachytherapy can be performed safely inside an MRI scanner, with no need to take into account the magnetic field for dose calculations.

Chapter 3 has described a method for real-time MR-based source localization with high spatial and temporal resolution as required in HDR brachytherapy. The main aim of MR-based localization of an HDR brachytherapy source is twofold. First, it enables determination of the source dwell positions during irradiation for real-time treatment verification. Second, when employing a dummy source, it allows automatic source dwell position reconstruction after catheter insertion, necessary for treatment planning. The method involves simulation of the MRI artifact induced by the HDR source, followed by a phase correlation localization algorithm applied to the simulated and the acquired MRI artifact to determine the position of the HDR source in the MR image. To increase the temporal resolution during MR imaging, the spatial resolution was decreased and a subpixel localization operation was introduced. To additionally decrease the dynamic scan time, parallel imaging (sensitivity encoding) was applied. A validation study was performed by a comparison with CT, and the accuracy and precision of the method were assessed. This resulted in localization of the HDR source with a high accuracy (0.4-0.6 mm) and a high precision ($\leq$0.1 mm), at high temporal resolutions (0.15-1.2 s per slice). The proposed method for MR-based source localization would enable

real-time treatment verification as well as automatic detection of the source dwell positions.

Real-time treatment verification using MR-based source localization demands for the development of an MR conditional afterloader, which has been presented in **Chapter 4**. Putting MR-based source localization into practice requires the patient to be positioned inside the MRI scanner during irradiation. Hence, the afterloader should be positioned directly next to the MRI scanner, and both systems should allow functioning simultaneously. A prototype MR conditional afterloader was developed and simultaneous functioning of this prototype and a 1.5 T MRI system was tested in an experimental setting. The afterloader was positioned next to the scanner and the source was sent to predefined source positions in a catheter inside a phantom, while acquiring MR images. The method for MR-based source localization was applied to evaluate functioning of both systems. Furthermore, the influence of the presence and use of the afterloader on the MRI performance was studied by assessment of RF interference, signal-to-noise (SNR) ratio and B_0 field homogeneity. Both systems have been demonstrated to function adequately while operating simultaneously, and the step sizes between the obtained source positions corresponded with the afterloader settings. Furthermore, the MRI performance tests demonstrated no deterioration due to the presence or functioning of the afterloader next to the scanner. This has demonstrated the feasibility of simultaneous MRI acquisition and employment of an MR conditional afterloader.

Chapter 5 has provided more flexibility for putting MR-based object localization in practice, by simulating the MRI artifacts induced by an HDR brachytherapy source as well as a titanium needle for clinically relevant MRI sequences. The purpose was to investigate the potential of several clinically relevant MRI sequences to facilitate tracking/localization of brachytherapy devices, which could simultaneously be used for visualization of the anatomy. Four types of MRI sequences were included in the simulations: spoiled gradient echo, spin echo, balanced steady state free precession (bSSFP) and bSSFP with a spectral attenuated inversion recovery (SPAIR) fat suppression. A phantom study was performed to acquire the MR images, using two imaging approaches: (I) four fast 2D MRI sequences for real-time tracking, and (II) clinically applied 3D/volumetric MRI sequences for robust object localization and position verification. The results have demonstrated that the simulated MRI artifacts corresponded with the acquired MRI artifacts, and allowed object localization for all considered MRI sequences. The mean deviations from the average object position were 0.2-0.3 mm for all applied sequences. Accordingly, this has demonstrated that the MRI artifact simulations are valuable for real-time device tracking for a range of clinically relevant MRI sequences, which allow simultaneous visualization of the anatomy.

6.2 General discussion

The work presented in this thesis has demonstrated the feasibility and the main advances in the development of a fully MRI-guided HDR brachytherapy workflow. We proposed an MR-guided HDR brachytherapy workflow where an MR-based source localization method is applied for reconstruction of the source dwell positions and for treatment verification, employ-

ing an MR conditional afterloader. While MRI has been applied for catheter reconstruction and treatment planning, many steps may be taken in the near future towards the employment of MRI in all processes of the treatment improving the quality and workflow efficiency.

6.2.1 Clinical workflow

The work presented in this thesis may considerably contribute to an improved clinical workflow of the prostate HDR brachytherapy treatment. All parts have contributed in a different manner. From a dose perspective, the HDR brachytherapy treatment can safely be performed while the patient is being positioned inside the MRI scanner bore, as has been proven in Chapter 2. Treatment planning can remain unchanged, as the Monte Carlo simulations have proven no need to account for the magnetic field. Next, we presented a method for MR-based HDR source (or needle) localization, based on MRI artifact simulation and template matching between the MR image and the simulated artifact (Chapters 3 and 5). Furthermore, the development of the MR conditional afterloader (Chapter 4) has shown the practical feasibility of MR-based source tracking by simultaneous application of the afterloader to send the source to the planned dwell positions and the MRI scanner to acquire the MR images. Lastly, our institution possesses an HDR brachytherapy MRI suite: a bunker that contains a 1.5 T MRI system, suitable for a future treatment set-up with MRI guidance during dose delivery. When combining all aspects mentioned above, this demonstrates the feasibility of performing an HDR brachytherapy treatment while the patient is positioned inside the MR bore. Consequently, we propose an MR-guided HDR brachytherapy treatment set-up where the patient remains in the MR bore (and thus in the same position) during the complete process of source dwell position reconstruction, treatment planning and irradiation while MR images are acquired to guide the process.

Figure 6.1a presents a workflow diagram of the actions performed clinically in our department. Next, Figure 6.1b presents a newly proposed workflow of an MR-guided treatment based on the work in this thesis, where HDR source localization is applied for automatic dwell position reconstruction and real-time treatment verification. This workflow eliminates most manual interactions (manual catheter reconstruction and visual catheter positions check) and eliminates repeated movements of the patient table in/out of the MR bore. The proposed treatment set-up offers expected advantages important for the treatment quality and the practical clinical workflow. The patient remains in the same position during MR imaging/source position reconstruction, treatment planning and irradiation. The treatment is more accurate (direct source position reconstruction, less motion) and less time-consuming (more automated steps). A decreased number of manual interactions leads to a decreased chance of errors and a more straightforward workflow. Lastly, possible errors could be detected, such that the treatment can be interrupted when necessary.

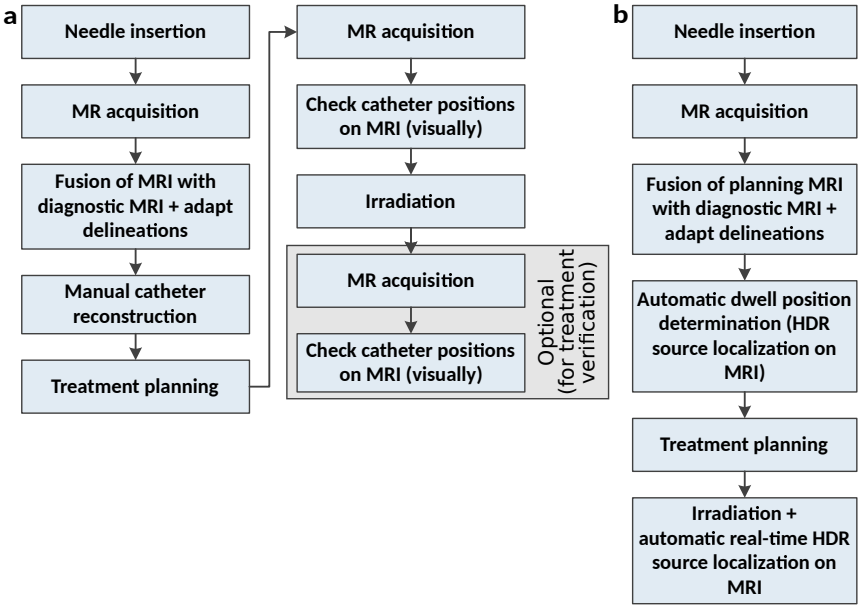

Figure 6.1 (a) The actions performed in current clinical practice of the HDR brachytherapy treatment in our department. **(b)** The proposed workflow diagram of the MR-guided HDR brachytherapy treatment, where MR-based HDR source localization is applied for an automatic determination of the source dwell positions and for real-time HDR source localization during irradiation.

6.2.2 Object localization

In this thesis, object localization has been demonstrated for an HDR brachytherapy source and a titanium needle by MRI artifact simulation in combination with template matching between the MR images and the simulated artifacts. The proposed method has shown excellent results (Chapter 3). However, all experiments were conducted solely in phantom studies. Before introducing the method into clinical applications, the ability and correctness of the object localization algorithm needs to be confirmed for *in vivo* cases for an HDR source and a needle. We need to investigate if the artifacts will look identically in *in vivo* situations where conditions might vary, for example a B_0 offset or gradient. Other studies have demonstrated the feasibility of a similar object localization *in vivo* for gold fiducial markers in the prostate [149] and for low-dose-rate (LDR) brachytherapy seeds [32]. However, in case of HDR brachytherapy, an additional challenge is posed by bleedings due to the needle insertion, as the localization method is applied during an intraoperative procedure. Additionally, in case of the titanium needle, a study should be performed to explore if the artifacts induced by the tip of the titanium needle are sufficiently large and characteristic to be localized in an *in vivo* situation instead of in a homogeneous phantom. Therefore, the next phase will be to apply the object localization algorithm in a patient study where a marker or dummy source will be brought into a catheter implanted into the prostate, to test localization of this marker

in an *in vivo* situation.

Besides application of the object localization method for HDR brachytherapy purposes, the object localization might also be a valuable tool for marker detection for position verification in external beam therapy. In external beam therapy of prostate cancer, generally three or four gold fiducial markers are implanted into the prostate, and their positions are determined and used for accurate patient positioning. Since gold has a magnetic susceptibility value of χ = -34 ppm, these markers also induce susceptibility artifacts, which we can simulate as described in chapter 5 and exploit for localization. This has been demonstrated for spoiled gradient echo sequences [149], but also for this purpose, bSSFP (SPAIR) sequences may be highly valuable for a simultaneous visualization of the anatomy and marker detection. This might replace the currently manually performed marker detection by an automated marker localization, important for an MR-only workflow.

6.2.3 Treatment verification

While other groups have been attempting to achieve treatment verification by methods such as in vivo dosimetry, EM tracking or FBG-based sensing, MR-based source localization might be a more direct manner of treatment verification. MR-based source localization allows a direct and real-time detection of the source dwell positions during irradiation, while MRI simultaneously allows visualization and tracking of the anatomy. Hence, tracking of the source as well as the anatomy takes place in one coordinate system, so the positions of both are in a direct relation with each other; no additional registration and calibration steps are necessary. The other techniques for treatment verification are hampered by challenges related to coordinate systems and anatomy tracking. For example, during in vivo dosimetry, the dose is measured in one or several points near the target area [124, 125]. This dose subsequently should be reconstructed to the dose that was delivered to the tumor. Since the dosimeter measures the dose in an area subjected to a steep dose gradient, a small deviation in the dose measurement might lead to large errors of the dose reconstruction. Moreover, another challenge is posed by determining the position of the dosimeter with respect to the tumor position, which may change due to patient motion. Techniques as EM tracking and FBG-based sensing allow detection of a catheter, but include no real-time verification during irradiation [56–59]. Additionally, these techniques provide no anatomical information and, thus, always require combination with a certain imaging modality followed by a registration step. Accordingly, MR-based source localization might be a more direct manner of treatment verification as it provides real-time tracking of the source, while simultaneously allowing visualization and tracking of the anatomy directly in the same coordinate system.

In this thesis, source localization has been conducted offline in a post-processing step. When implementing the subpixel source localization algorithm on the MRI scanner software or a server in direct connection with the scanner, localization of the source may be performed online in a real-time setting. Simultaneously, tracking of the anatomy may be included by introducing an anatomy tracking algorithm, for example optical flow tracking [150], Evolution [151] or online soft tissue tracking [152]. Furthermore, in HDR brachytherapy, the

delivered dose can be obtained directly from the source dwell positions and dwell times (as provided in the treatment plan) in combination with the anatomy. Hence, the combination of real-time source tracking and anatomy tracking allows real-time treatment verification and real-time dose-reconstruction.

A first step towards the application of real-time treatment verification may be to introduce a means for interruption of the irradiation when an error is detected. During the interruption time, an adaptation to the detected error and possibly a new resuming treatment plan may be made, after which the treatment can continue. When moving further towards real-time dose reconstruction, the source and anatomy tracking information may be combined with information from the afterloader and from the treatment planning system. When also adding an adaptive treatment planning strategy [153], a full feedback loop for adaptive HDR brachytherapy can be built. In such a feedback loop, changes due to motion might be taken into account and acted upon by directly adapting the treatment plan and changing the dwell times and dwell positions to be sent to the afterloader. This creates a real-time adaptive treatment under MRI guidance. A practical implementation of such an adaptive feedback loop requires more work to be carried out to combine all separate parts into one workflow and to implement the necessary software in a planning system for continuous updates of the MR images, the HDR source position and the dose distribution.

6.2.4 Source position reconstruction

While MR-based source localization for real-time treatment requires significant and complex software solutions to combine all parts needed to create the full adaptive feedback loop, MR-based source localization for automatic source position reconstruction in the treatment planning process is closer in reach and an easier scenario to implement. As a first step, automatic detection of the source dwell positions can be fulfilled by the use of markers brought into the catheters during MR imaging and application of the subpixel localization algorithm to determine the positions of the markers, and thus the catheters. This might also be applied when using catheters, which contain markers secured into the catheter walls for localization of the catheters instead of a marker inside the catheter. A more elaborate and accurate application of the source position reconstruction method includes the use of the MR conditional afterloader and a dummy source. This involves the afterloader to send the dummy source to the dwell positions within the catheters, while also acquiring MR images, followed by a determination of the source positions from the MR images using the source localization algorithm. Accordingly, this scenario fulfills a fully automatic reconstruction of the source dwell positions. Moreover, while most methods focus on reconstruction of the catheter tracks, the proposed technique direcly provides the source dwell positions, which is most accurate for treatment planning as it most closely resembles the situation during irradiation. For example, a technique that reconstructs the catheter tracks requires an additional calculation step, and more importantly another calibration, to determine the source dwell positions within the catheter tracks.

Regarding the current clinical workflow, the proposed automatic source position reconstruc-

tion may provide excellent solutions for the main challenges. In current clinical workflow, the catheters are reconstructed based on a manual definition of the position of the catheter tip and the entry point in a 3D MRI (bSSFP SPAIR) scan, based on the signal voids. One of the main challenges is the catheter reconstruction in cases where the catheter tip is positioned in an area outside the prostate, because of lower signal intensities, or in an area of calcifications or a bleeding. In these cases, the signal void due to the catheter is hard to distinguish. Another difficulty is posed by situations where catheters cross each other in the MR images, which harms reconstruction of the separate catheter tracks. The proposed automatic source localization solves these difficulties, since it reconstructs the source positions along the full track and does not only depend on the tip of the catheter. Furthermore, an automated detection of the source positions allows elimination of the manual catheter reconstruction, which might save time and reduces the chances on human errors. Lastly, the method for source position localization has demonstrated a high accuracy of 0.4-0.6 mm, presented in Chapter 3, which is slightly higher than the accuracy of 0.7 mm for the currently available catheter reconstruction tools for HDR prostate brachytherapy [130].

6.2.5 MR conditional afterloader

One of the main limitations that currently prevents the MR conditional afterloader from being introduced in clinics is the source cable. The source cables in clinical HDR brachytherapy afterloaders are made of steel. However, the steel cable poses safety risks, such as heating and torques. Furthermore, the steel cable would serve as an antenna transferring RF signals from the afterloader which deteriorate the MR images. Consequently, the steel cable can not be used inside an MRI scanner and, therefore, an MR compatible source cable should be developed. The requirements for an MR compatible source cable are that it should be flexible, strong and stiff to send the source out to the correct position with a reliability at least equal to that of the steel cable. Additionally, the material should be MR compatible and resistant to the radiation emitted by the source, and a reliable connection between the source and source cable is crucial.

Furthermore, the use of MRI for treatment verification using an MR conditional afterloader demands for an adapted treatment room. The HDR brachytherapy MRI suite in our institution is a unique treatment room: an HDR brachytherapy bunker that contains a 1.5 T MRI scanner. Such a bunker is required when introducing an HDR brachytherapy workflow that applies real-time MRI guided treatment verification. Few institutions have an MR scanner in the brachytherapy suite, which might be a limitation for widespread introduction of MRI guided HDR brachytherapy with an MR conditional afterloader. However, many centers will soon have access to an MR-linac system, which needs to be positioned inside a treatment bunker as well. The MR conditional afterloader might be used in combination with the MRI scanner in an MR-linac treatment bunker.

6.2.6 Real-time aspect

Chapter 3 has stressed the need for MR-based source localization with a high temporal resolution. To be able to detect the HDR source positions for dose verification, fast imaging and post-processing are needed. The dwell times in HDR brachytherapy are typically between 1 and 30 s, with minimum values of around 0.3 s. Consequently, we defined a temporal resolution of 0.3 s as the threshold for real-time determination of the source position. In other words, the maximum latency allowed for real-time source localization is 0.3 s. We can define the latency for source localization as the time between the moment the source has a certain physical position and the time of detection of that position from the reconstructed MR image and the localization algorithm. This latency has contributions due to the acquisition time, data transfer and reconstruction time, and post processing time.

Chapter 3 has focused on decreasing the dynamic scan time in the MRI acquisition, obtained by applying a fast 2D sequence with decreased spatial resolution combined with a subpixel localization and the application of SENSE. Dynamic scan times between 0.3 and 2.4 s were obtained, depending on the FOV and resolution. Whereas latency was not considered in this thesis, a decreased latency may be obtained when a *high-low* phase encode ordering is applied during the MR acquisition [154]. Additionally, reconstruction can be performed fast, since it concerns a basic 2D SENSE reconstruction (when applying 2D imaging with two 2D slices), which is feasible in real time employing dedicated hardware [131, 132]. Furthermore, the phase correlation localization is a fast algorithm, since it consists of a multiplication in k-space, followed by zeropadding and an inverse Fourier transform. In this thesis, the processing was performed offline in Matlab in the order of a few hundreds of milliseconds. We expect this might be accelerated by at least a factor 10 using dedicated programming optimized for speed. Considering these processes contributing to the latency altogether, we might expect a time scale on the order of real-time source localization.

To be able to perform the complete source localization in real time, a system is required to implement the software for real-time processing. The future goal is to cooperate with the developments for the MR-linac and to share the system architecture needed for real-time applications.

6.2.7 Robotic MRI guided HDR brachytherapy

A device for robotic MRI guided prostate HDR brachytherapy has been in development in our institution [95]. In current clinical practice, MRI guided needle insertion is not possible due to space restrictions in the closed MR bore. The development of a robotic device might solve this problem by robotically inserting a needle into the prostate under MRI guidance. The device can be placed between the legs of the patient inside the MR bore. The robot contains a single titanium needle which can be tapped into the tissue from a single rotation point just beneath the perineal skin in a divergent pattern. During such a robotic procedure of needle insertion, a method for real-time needle tracking is desired. Chapter 5 has demonstrated that we are able to localize a titanium needle by MRI artifact simulation together with a

phase correlation localization algorithm. The goal for the near future is to introduce the robot in a patient study in a clinical setting, and to apply the method for object localization presented in this thesis to track the titanium needle during the insertion. Once the needle is inserted, the localization algorithm will provide the final needle position which can then be used for treatment planning. After irradiation from the first needle position, the needle will be retracted and inserted into the next position, and this will proceed until the planned dose has been given from all planned needle positions. Certainly, the future goal will be to combine this robotic treatment set-up with the MR-based source localization method for treatment verification, such that the full HDR brachytherapy treatment will be under MRI guidance.

Chapter 7

Bibliography

Bibliography

[1] Khan F M. *The physics of radiation therapy*. Lippincott Williams & Wilkins, third edition, 2003.

[2] Podgorsak E B. *Radiation oncology physics: a handbook for teachers and students*. International Atomic Energy Agency, 2005.

[3] Demanes D J and Ghilezan M I. High-dose-rate brachytherapy as monotherapy for prostate cancer. *Brachytherapy*, 13:529–541, 2014.

[4] Hauswald H, Kamrava M R, Fallon J M, Wang P C, Park S J, Van T, Borja L, Steinberg M L and Demanes D J. High-dose-rate monotherapy for localized prostate cancer: 10-year results. *Int. J. Radiat. Oncol. Biol. Phys.*, 94:667–674, 2016.

[5] Yoshioka Y, Suzuki O, Isohashi F, *et al*. High-dose-rate brachytherapy as monotherapy for intermediate- and high-risk prostate cancer: Clinical results for a median 8-year follow-up. *Int. J. Radiat. Oncol. Biol. Phys.*, 94:675–682, 2016.

[6] Maenhout Metha, Peters Max, Moerland Marinus A., Meijer Richard P., Bosch van den Maurice A.A.J., Frank Steven J., Nguyen Paul L., Vulpen van Marco and van der Voort van Zyp Jochem R.N. MRI guided focal HDR brachytherapy for localized prostate cancer: Toxicity, biochemical outcome and quality of life. *Radiotherapy and Oncology*, 129(3):554–560, 2018.

[7] Prada P J, Cardenal J, Blanco A G, Anchuelo J, Ferri M, Fernández G, Arrojo E, Vázquez A, Pacheco M and Fernández J. High-dose-rate interstitial brachytherapy as monotherapy in one fraction for the treatment of favorable stage prostate cancer: Toxicity and long-term biochemical results. *Radiother. Oncol.*, 119:411–416, 2016.

[8] Demanes D J, Martinez A A, Ghilezan M, Hill D R, Schour L, Brandt D and Gustafson G. High-dose-rate monotherapy: safe and effective brachytherapy for patients with localized prostate cancer. *Int. J. Radiat. Oncol. Biol. Phys.*, 81:1286–1292, 2011.

[9] Yoshioka Y, Konishi K, Sumida I, *et al*. Monotherapeutic high-dose-rate brachytherapy for prostate cancer: five-year results of an extreme hypofractionation regimen with 54 Gy in nine fractions. *Int. J. Radiat. Oncol. Biol. Phys.*, 80:469–475, 2011.

[10] Barkati M, Williams S G, Foroudi F, Tai K H, Chander S, Van Dyk S, See A and Duchesne G M. High-dose-rate brachytherapy as a monotherapy for favorable-risk prostate cancer: A phase II trial. *Int. J. Radiat. Oncol. Biol. Phys.*, 82:1889–1896, 2012.

[11] Hoskin P, Rojas A, Lowe G, Bryant L, Ostler P, Hughes R, Milner J and Cladd H. High-dose-rate brachytherapy alone for localized prostate cancer in patients at moderate or high risk of biochemical recurrence. *Int. J. Radiat. Oncol. Biol. Phys.*, 82:1376–1384, 2012.

[12] Ritter M. Rationale, conduct, and outcome using hypofractionated radiotherapy in prostate cancer. *Semin. Radiat. Oncol.*, 18:249–256, 2008.

[13] Mavroidis P, Milickovic N, Cruz W F, Tselis N, Karabis A, Stathakis S, Papanikolaou N, Zamboglou N and Baltas D. Comparison of different fractionation schedules toward a single fraction in high-dose-rate brachytherapy as monotherapy for low-risk prostate cancer using 3-dimensional radiobiological models. *Int. J. Radiat. Oncol. Biol. Phys.*, 88:216–223, 2014.

[14] Morton G, Chung H T, McGuffin M, *et al*. Prostate high dose-rate brachytherapy as monotherapy for low and intermediate risk prostate cancer: Early toxicity and quality-of life results from a randomized phase II clinical trial of one fraction of 19 Gy or two fractions of 13.5 Gy. *Radiother. Oncol.*, 122:87–92, 2017.

[15] Krauss D J, Martinez A A, Ye H, Wallace M, Marvin K, Ghilezan M and Gustafson G S. Highly favorable preliminary clinical and toxicity outcomes for low-and intermediate-risk prostate cancer patients treated with high-dose-rate brachytherapy in a single fraction of 19 Gy. *Int. J. Radiat. Oncol. Biol. Phys.*, 93:S122, 2015.

[16] Morton G C and Hoskin P J. Brachytherapy: current status and future strategies - Can high dose rate replace low dose rate and external beam radiotherapy? *Clin. Oncol.*, 25:474–482, 2013.

[17] Zamboglou C, Rischke H C, Meyer P T, Knobe S, Volgeova-Neher N, Kollefrath M, Jilg C A, Grosu A L, Baltas D and Kroenig M. Single fraction multimodal image guided focal salvage high-dose-rate brachytherapy for recurrent prostate cancer. *J. Contemp. Brachytherapy*, 8:241–248, 2016.

[18] Maenhout M, Peters M, Van Vulpen M, Moerland M A, Meijer R P, Van den Bosch M A A J, Nguyen P L, Frank S J and Van der Voort van Zyp J R N. Focal MRI-guided salvage high-dose-rate brachytherapy in patients with radiorecurrent prostate cancer. *Technology in Cancer Research and Treatment*, 16:1194–1201, 2017.

[19] Ménard C, Susil R C, Choyke P, *et al*. MRI-guided HDR prostate brachytherapy in standard 1.5T scanner. *Int. J. Radiat. Oncol. Biol. Phys.*, 59:1414–1423, 2004.

[20] Atalar E and Ménard C. MR-guided interventions for prostate cancer. *Magn. Reson. Imaging Clin. N. Am.*, 13:491–504, 2005.

[21] Zangos S, Eichler K, Thalhammer A, Schoepf J U, Costello P, Herzog C, Mack M G and Vogl T J. MR-guided interventions of the prostate gland. *Minim. Invasive Ther. Allied Technol.*, 16:222–229, 2007.

[22] Tanderup K, Viswanathan A N, Kirisits C and Frank S J. Magnetic resonance image guided brachytherapy. *Semin. Radiat. Oncol.*, 24:181–191, 2014.

[23] Barentsz J O, Richenberg J, Clements R, Choyke P, Verma S, Villeirs G, Rouviere O, Logager V and Fütterer J J. ESUR prostate MR guidelines 2012. *Eur. Radiol.*, 22:746–757, 2012.

[24] Pugh T J, Frank S J, Achim M, Kuban D A, Lee A K, Hoffman K E, McGuire S E, Swanson D A, Kudchadker R and Davis J W. Endorectal magnetic resonance imaging for predicting pathologic T3 disease in Gleason score 7 prostate cancer: Implications for prostate brachytherapy. *Brachytherapy*, 12:204–209, 2013.

[25] McLaughlin P W, Troyer S, Berri S, Narayana V, Meirowitz A, Roberson P L and Montie J. Functional anatomy of the prostate: Implications for treatment planning. *Int. J. Radiat. Oncol. Biol. Phys.*, 63:479–491, 2005.

[26] Marcus D M, Rossi P J, Nour S G and Jani A B. The impact of multiparametric pelvic magnetic resonance imaging on risk stratification in patients with localized prostate cancer. *Urology*, 84:132–137, 2014.

[27] Lawrence E M, Gallagher F A, Barrett T, Warren A Y, Priest A N, Goldman D A, Sala E and Gnanapragasam V J. Preoperative 3-T diffusion-weighted MRI for the qualitative and quantitative assessment of extracapsular extension in patients with intermediate- or high-risk prostate cancer. *Am. J. Roentgenol.*, 203:W280–W286, 2014.

[28] Jie C, Rongbo L and Ping T. The value of diffusion-weighted imaging in the detection of prostate cancer: a meta-analysis. *Eur. Radiol.*, 24:1929–1941, 2014.

[29] Hoskin P J, Colombo A, Henry A, Niehoff P, Paulsen Hellebust T, Siebert F A and Kovacs G. GEC/ESTRO recommendations on high dose rate afterloading brachytherapy for localised prostate cancer: An update. *Radiother. Oncol.*, 107:325–332, 2013.

[30] D'Amico A V, Cormack R, Tempany C M, Kumar S, Topulos G, Kooy H M and Coleman C N. Real-time magnetic resonance image-guided interstitial brachytherapy in the treatment of select patients with clinically localized prostate cancer. *Int. J. Radiat. Oncol. Biol. Phys.*, 42:507–515, 1998.

[31] Ohashi T, Momma T, Yamashita S, Nagatsuma K, Kanai K, Kitagawa K, Takahashi S, Hanada T, Yorozu A and Shigematsu N. Impact of MRI-based postimplant dosimetric assessment in prostate brachytherapy using contrast-enhanced T1-weighted images. *Brachytherapy*, 11:468–475, 2012.

[32] Zijlstra F, Moerland M A, Van der Voort van Zyp J R N, Noteboom J L, Viergever M A and Seevinck P R. Challenges in MR-only seed localization for postimplant dosimetry in permanent prostate brachytherapy. *Med. Phys.*, 44:5051–5060, 2017.

[33] Nguyen P L, Chen M H, Zhang Y, Tempany C M, Cormack R A, Beard C J, Hurwitz M D, Suh W W and D'Amico A V. Updated results of magnetic resonance imaging guided partial prostate brachytherapy for favorable risk prostate cancer: Implications for focal therapy. *J. Urol.*, 188:1151–1156, 2012.

[34] Wang W, Viswanathan A N, Damato A L, *et al*. Evaluation of an active magnetic resonance tracking system for interstitial brachytherapy. *Med. Phys.*, 42:7114–7121, 2015.

[35] Ricke J, Thormann M, Ludewig M, Jungnickel K, Grosser O, Wybranski C, Peters N, Hass P, Bunke J and Fischbach F. MR-guided liver tumor ablation employing open high-field 1.0T MRI for image-guided brachytherapy. *Eur. Radiol.*, 20:1985–1993, 2010.

[36] Thomadsen B, Lin S W, Laemmrich P, Waller T, Cheng A, Caldwell B, Rankin R and Stitt J. Analysis of treatment delivery errors in brachytherapy using formal risk analysis techniques. *Int. J. Radiat. Oncol. Biol. Phys.*, 57:1492–1508, 2003.

[37] Wilkinson D A and Kolar M D. Failure modes and effects analysis applied to high-dose-rate brachytherapy treatment planning. *Brachytherapy*, 12:382–386, 2013.

[38] Bus S J E A, Leus N G, Oosterveld B J, Van Gellekom M P R, Van de Loop G J M and Van der Steen-Banasik E M. An evaluation of our experience in position verification of catheters used for interstitial high-dose-rate brachytherapy of solitary bladder tumors. *Brachytherapy*, 17:24–30, 2018.

[39] Buus S, Lizondo M, Hokland S, Rylander S, Pedersen E M, Tanderup K and Bentzen L. Needle migration and dosimetric impact in high-dose-rate brachytherapy for prostate cancer evaluated by repeated MRI. *Brachytherapy*, 17:50–58, 2018.

[40] Van den Ende R P J, Rijkmans E C, Kerkhof E M, Nout R A, Ketelaars M, Laman M S, Marijnen C A M and Van der Heide U A. Benefit of adaptive CT-based treatment planning in high-dose-rate endorectal brachytherapy for rectal cancer. *Brachytherapy*, 17:78–85, 2018.

[41] Zoberi J E, Garcia-Ramirez J, Hedrick S, Rodriguez V, Bertelsman C G, Mackey S, Hu Y, Gach H M, Rao P K and Grigsby P W. MRI-based treatment planning and dose delivery verification for intraocular melanoma brachytherapy. *Brachytherapy*, 17:31–39, 2018.

[42] Maenhout M, van der Voort van Zyp J R N, Borot de Battisti M, Peters M, Van Vulpen M, Van den Bosch M and Moerland M A. The effect of catheter displacement and anatomical variations on the dose distribution in MRI-guided focal HDR brachytherapy for prostate cancer. *Brachytherapy*, 17:68–77, 2018.

[43] Anagnostopoulos G, Baltas D, Geretschlaeger A, Martin T, Papagiannis P, Tselis N and Zamboglou N. In vivo thermoluminescence dosimetry dose verification of transperineal192Ir high-dose-rate brachytherapy using CT-based planning for the treatment of prostate cancer. *Int. J. Radiat. Oncol. Biol. Phys.*, 57:1183–1191, 2003.

[44] Jaselske E, Adliene D, Rudžianskas V, Urbonavičius B G and Inčiura A. In vivo dose verification method in catheter based high dose rate brachytherapy. *Phys. Med.*, 44:1–10, 2017.

[45] Haughey A, Coalter G and Mugabe K. Evaluation of linear array MOSFET detectors for in vivo dosimetry to measure rectal dose in HDR brachytherapy. *Australas. Phys. Eng. Sci. Med.*, 34:361–366, 2011.

[46] Reniers B, Landry G, Eichner R, Hallil A and Verhaegen F. In vivo dosimetry for gynaecological brachytherapy using a novel position sensitive radiation detector: Feasibility study. *Med. Phys.*, 39:1925–1935, 2012.

[47] Mason J, Mamo A, Al-Qaisieh B, Henry A M and Bownes P. Real-time in vivo dosimetry in high dose rate prostate brachytherapy. *Radiother. Oncol.*, 120:333–338, 2016.

[48] Kertzscher G, Andersen C E, Siebert F A, Nielsen S K, Lindegaard J C and Tanderup K. Identifying afterloading PDR and HDR brachytherapy errors using real-time fiber-coupled Al2O3:C dosimetry and a novel statistical error decision criterion. *Radiother. Oncol.*, 100:456–462, 2011.

[49] Tien C, Ebeling R, Hiatt J R, Curran B and Sternick E. Optically stimulated luminescent dosimetry for high dose rate brachytherapy. *Front. Oncol.*, 2:91, 2012.

[50] Sharma R and Jursinic P A. In vivo measurements for high dose rate brachytherapy with optically stimulated luminescent dosimeters. *Med. Phys.*, 40:071730, 2013.

[51] Johansen J G, Rylander S, Buus S, Bentzen L, Hokland S B, Søndergaard C S, With A K M, Kertzscher G and Tanderup K. Time-resolved in vivo dosimetry for source tracking in brachytherapy. *Brachytherapy*, 17:122–132, 2018.

[52] Carrara M, Cutajar D, Alnaghy S, *et al*. Semiconductor real-time quality assurance dosimetry in brachytherapy. *Brachytherapy*, 17:133–145, 2018.

[53] Smith R L, Taylor M L, McDermott L N, Haworth A, Millar J L and Franich R D. Source position verification and dosimetry in HDR brachytherapy using an EPID. *Med. Phys.*, 40:111706, 2013.

[54] Fonseca G P, Podesta M, Bellezzo M, Van den Bosch M R, Lutgens L, Vanneste B G L, Voncken R, Limbergen E J Van, Reniers B and Verhaegen F. Online pretreatment verification of high-dose rate brachytherapy using an imaging panel. *Phys. Med. Biol.*, 62:5440–5461, 2017.

[55] Tanderup K, Ménard C, Polgar C, Lindegaard J C, Kirisits C and Pötter R. Advancements in brachytherapy. *Adv. Drug Deliv. Rev.*, 109:15–25, 2017.

[56] Zhou J, Sebastian E, Mangona V and Yan D. Real-time catheter tracking for high-dose-rate prostate brachytherapy using an electromagnetic 3D-guidance device: A preliminary performance study. *Med. Phys.*, 40:021716, 2013.

[57] Poulin E, Racine E, Binnekamp D and Beaulieu L. Fast, automatic, and accurate catheter reconstruction in HDR brachytherapy using an electromagnetic 3D tracking system. *Med. Phys.*, 42:1227–1232, 2015.

[58] Boutaleb S, Racine E, Fillion O, Bonillas A, Hautvast G, Binnekamp D and Beaulieu L. Performance and suitability assessment of a real-time 3D electromagnetic needle tracking system for interstitial brachytherapy. *J. Contemp. Brachytherapy*, 7:280–289, 2015.

[59] Borot de Battisti M, Denis de Senneville B, Maenhout M, Lagendijk J J W, Van Vulpen M, Hautvast G, Binnekamp D and Moerland M A. Fiber Bragg gratings-based sensing for real-time needle tracking during MR-guided brachytherapy. *Med. Phys.*, 43:5288–5297, 2016.

[60] Brown R W, N Cheng Y C and M Haacke E. *Magnetic resonance imaging: physical principles and sequence design*. John Wiley & Sons, Inc., 2014.

[61] Patton J A. MR imaging instrumentation and image artifacts. *Radiographics*, 14:1083–1096, 1994.

[62] Schenck J F. The role of magnetic susceptibility in magnetic resonance imaging: MRI magnetic compatibility of the first and second kinds. *Medical Physics*, 23:815–850, 1996.

[63] Lide D. *Handbook of Chemistry and Physics*. 84 edition, 2004.

[64] Hargreaves B A, Worters P W, Butts Pauly K, Pauly J M, Koch K M and Gold G E. Metal-induced artifacts in MRI. *Am. J. Roentgenol.*, 197:547–555, 2011.

[65] Bhagwandien R, Moerland M A, Bakker C J G, Beersma R and Lagendijk J J W. Numerical analysis of the magnetic field for arbitrary magnetic susceptibility distributions in 2D. *Magn. Reson. Imaging*, 10:299–313, 1992.

[66] Bhagwandien R, Moerland M A, Bakker C J G, Beersma R and Lagendijk J J W. Numerical analysis of the magnetic field for arbitrary magnetic susceptibility distributions in 3D. *Magn. Reson. Imaging*, 12:101–107, 1994.

[67] Jenkinson M, Wilson J L and Jezzard P. Perturbation method for magnetic field calculations of nonconductive objects. *Magn. Reson. Med.*, 52:471–477, 2004.

[68] Marques J P and Bowtell R. Application of a Fourier-based method for rapid calculation of field inhomogeneity due to spatial variation of magnetic susceptibility. *Concepts Magn. Reson. Part B*, 25:65–78, 2005.

[69] Bouwman J G and Bakker C J G. Alias subtraction more efficient than conventional zero-padding in the Fourier-based calculation of the susceptibility induced perturbation of the magnetic field in MR. *Magn. Reson. Med.*, 68:621–630, 2012.

[70] Bakker C J G, Bhagwandien R, Moerland M A and Fuderer M. Susceptibility artifacts in 2DFT spin-echo and gradient-echo imaging: the cylinder model revisited. *Magn. Reson. Imaging*, 11:539–548, 1993.

[71] Bakker C J G, Bhagwandien R, Moerland M A and Ramos L M P. Simulation of susceptibility artifacts in 2D and 3D Fourier transform spin-echo and gradient-echo magnetic resonance imaging. *Magn. Reson. Imaging*, 12:767–774, 1994.

[72] Balac S, Caloz G, Cathelineau G, Chauvel B and De Certaines J D. Integral method for numerical simulation of MRI artifacts induced by metallic implants. *Magn. Reson. Med.*, 45:724–727, 2001.

[73] Salomir R, Denis de Senneville B and Moonen C T W. A fast calculation method for magnetic field inhomogeneity due to an arbitrary distribution of bulk susceptibility. *Concepts Magn. Reson. Part B*, 19:26–34, 2003.

[74] Muller-Bierl B, Graf H, Lauer U, Steidle G and Schick F. Numerical modeling of needle tip artifacts in MR gradient echo imaging. *Med. Phys.*, 31:579–587, 2004.

[75] Benoit-Cattin H, Collewet G, Belaroussi B, Saint-Jalmes H and Odet C. The SIMRI project: a versatile and interactive MRI simulator. *Journal of Magnetic Resonance*, 173:97–115, 2005.

[76] Wachowicz K, Thomas S D and Fallone B G. Characterization of the susceptibility artifact around a prostate brachytherapy seed in MRI. *Med. Phys.*, 33:4459–4467, 2006.

[77] Lagerburg V, Moerland M A, Seppenwoolde J H and Lagendijk J J W. Simulation of the artefact of an iodine seed placed at the needle tip in MRI-guided prostate brachytherapy. *Phys. Med. Biol.*, 53:N59–N67, 2008.

[78] Zijlstra F, Bouwman J G, Braškute I, Viergever M A and Seevinck P R. Fast Fourier-based simulation of off-resonance artifacts in steady-state gradient echo MRI applied to metal object localization. *Magn. Reson. Med.*, 78:2035–2041, 2017.

[79] Bakker C J, Hoogeveen R M, Hurtak W F, Van Vaals J J, Viergever M A and Mali W P. MR-guided endovascular interventions: susceptibility-based catheter and near-real-time imaging technique. *Radiology*, 202:273–276, 1997.

[80] Rothgang E, Gilson W D, Wacker F, Hornegger J, Lorenz C H and Weiss C R. Rapid freehand MR-guided percutaneous needle interventions: An image-based approach to improve workflow and feasibility. *J. Magn. Reson. Imaging*, 37:1202–1212, 2013.

[81] Seppenwoolde J H, Viergever M A and Bakker C J G. Passive tracking exploiting local signal conservation: the white marker phenomenon. *Magn. Reson. Med.*, 50:784–790, 2003.

[82] Seevinck P R, De Leeuw H, Bos C and Bakker C J G. Highly localized positive contrast of small paramagnetic objects using 3D center-out radial sampling with off-resonance reception. *Magn. Reson. Med.*, 65:146–156, 2011.

[83] De Leeuw H, Moerland M A, Van Vulpen M, Seevinck P R and Bakker Chris J G. A dual-plane co-RASOR technique for accurate and rapid tracking and position verification of an Ir- 192 source for single fraction HDR brachytherapy. *Phys. Med. Biol.*, 58:7829–7839, 2013.

[84] Campbell-Washburn A E, Rogers T, Xue H, Hansen M S, Lederman R J and Faranesh A Z. Dual echo positive contrast bSSFP for real-time visualization of passive devices during magnetic resonance guided cardiovascular catheterization. *J. Cardiovasc. Magn. Reson.*, 16:88, 2014.

[85] Dong Y, Chang Z, Xie G, Whitehead G and Ji J X. Susceptibility-based positive contrast MRI of brachytherapy seeds. *Magn. Reson. Med.*, 74:716–726, 2015.

[86] Ghose S, Mitra J, Rivest-Hénault D, Fazlollahi A, Stanwell P, Pichler P, Sun J, Fripp J, Greer P B and Dowling J A. MRI-alone radiation therapy planning for prostate cancer: Automatic fiducial marker detection. *Med. Phys.*, 43:2218–2228, 2016.

[87] Omary R A, Unal O, Koscielski D S, Frayne R, Korosec F R, Mistretta C A, Strother C M and Grist T M. Real-time MR imaging-guided passive catheter tracking with use of gadolinium-filled catheters. *J. Vas. Interv. Radiol.*, 11:1079–1085, 2000.

[88] Ratnayaka K, Faranesh A Z, Hansen M S, *et al*. Real-time MRI-guided right heart catheterization in adults using passive catheters. *Eur. Heart J.*, 34:380–388, 2013.

[89] Bock M, Mu S, Zuehlsdorff S, Speier P, Fink C, Hallscheidt P, Umathum R and Semmler W. Active catheter tracking using parallel MRI and real- time image reconstruction. *Magn. Reson. Med.*, 55:1454–1459, 2006.

[90] Wech T, Shea S M, Barbot J, Vij K, Pan L, Lorenz C H and Patil S. Measurement accuracy of different active tracking sequences for interventional MRI. *J. Magn. Reson. Imaging*, 40:490–495, 2014.

[91] Wang W, Dumoulin C L, Viswanathan A N, *et al*. Real-time active MR-tracking of metallic stylets in MR-guided radiation therapy. *Magn. Reson. Med.*, 73:1803–1811, 2015.

[92] Quick H H, Zenge M O, Kuehl H, Kaiser G, Aker S, Massing S, Bosk S and Ladd M E. Interventional magnetic resonance angiography with no strings attached: wireless active catheter visualization. *Magn. Reson. Med.*, 53:446–455, 2005.

[93] Riffe M J, Yutzy S R, Jiang Y, *et al*. Device localization and dynamic scan plane selection using a wireless magnetic resonance imaging detector array. *Magn. Reson. Med.*, 71:2243–2249, 2014.

[94] Rube M A, Holbrook A B, Cox B F, Houston J G and Melzer A. Wireless MR tracking of interventional devices using phase-field dithering and projection reconstruction. *Magn. Reson. Imaging*, 32:693–701, 2014.

[95] Van den Bosch M R, Moman M R, Van Vulpen M, Battermann J J, Duiveman E, Van Schelven L J, De Leeuw H, Lagendijk J J W and Moerland M A. MRI-guided robotic system for transperineal prostate interventions: proof of principle. *Phys. Med. Biol.*, 55:N133–N140, 2010.

[96] Bostick W H. Possible techniques in direct-electron-beam tumor therapy. *Phys. Rev.*, 77:564–656, 1950.

[97] Bielajew A F. The effect of strong longitudinal magnetic fields on dose deposition from electron and photon beams. *Med. Phys.*, 20:1171–1179, 1993.

[98] Nardi E and Barnea G. Electron beam therapy with transverse magnetic fields. *Med. Phys.*, 26:967–973, 1999.

[99] Earl M A and Ma L. Depth dose enhancement of electron beams subject to external uniform longitudinal magnetic fields: A Monte Carlo study. *Med. Phys.*, 29:484–491, 2002.

[100] Chen Y, Bielajew A F, Litzenberg D W, Moran J M and Becchetti F D. Magnetic confinement of electron and photon radiotherapy dose: A Monte Carlo simulation with a nonuniform longitudinal magnetic field. *Med. Phys.*, 12:3810–3818, 2005.

[101] Jette D. Magnetic fields with photon beams: dose calculation using electron multiple-scattering theory. *Med. Phys.*, 27:1705–1716, 2000.

[102] Jette D. Magnetic fields with photon beams: Monte Carlo calculations for a model magnetic field. *Med. Phys.*, 27:2726–2738, 2000.

[103] Reiffel L, Li A, Chu J, Wheatly R W, Naqvi S, Pillsbury R and Saxena A. Control of photon beam dose profiles by localized transverse magnetic fields. *Phys. Med. Biol.*, 45:N177–N182, 2000.

[104] Raaymakers B W, Raaijmakers A J E, Kotte A N T J, Jette D and Lagendijk J J W. Integrating a MRI scanner with a 6 MV radiotherapy accelerator: dose deposition in a transverse magnetic field. *Phys. Med. Biol.*, 49:4109–4188, 2004.

[105] Raaijmakers A J E, Raaymakers B W and Lagendijk J J W. Integrating a MRI scanner with a 6 MV radiotherapy accelerator: dose increase at tissue-air interfaces in a lateral magnetic field due to returning electrons. *Phys. Med. Biol.*, 50:1363–1376, 2005.

[106] Raaijmakers A J E, Raaymakers B W and Lagendijk J J W. Magnetic-field-induced dose effects in MR-guided radiotherapy systems: dependence on the magnetic field strength. *Phys. Med. Biol.*, 53:909–923, 2008.

[107] Lagendijk J J W, Raaymakers B W, Raaijmakers A J E, Overweg J, Brown K J, Kerkhof E M, Van der Put R W, Hårdemark B, Van Vulpen M and Van der Heide U A. MRI/linac integration. *Radiother. Oncol.*, 86:25–29, 2008.

[108] Raaymakers B W, Lagendijk J J W, Overweg J, *et al*. Integrating a 1.5 T MRI scanner with a 6 MV accelerator: proof of concept. *Phys. Med. Biol.*, 54:N229–N237, 2009.

[109] Kirkby C, Murray B, Rathee S and Fallone B G. Lung dosimetry in a linac-MRI radiotherapy unit with a longitudinal magnetic field. *Med. Phys.*, 37:4722–4732, 2010.

[110] Oborn B M, Metcalfe P E, Butson M J, Rosenfeld A B and Keall P J. Electron contamination modeling and skin dose in 6 MV longitudinal field MRIgRT: Impact of the MRI and MRI fringe field. *Med. Phys.*, 39:874–890, 2012.

[111] NIST Standard Reference Database 124 . ESTAR: Stopping power and range tables for electrons. *NIST Physical Measurement Laboratory*, 2005.

[112] Agostinelli S, Allison J, Amako K, *et al*. GEANT4 - A simulation toolkit. *Nucl. Instrum. Methods Phys. Res. A*, 506:250–303, 2003.

[113] Allison J, Amako K, Apostolakis J, *et al*. Geant4 developments and applications. *IEEE Transactions on Nuclear Science*, 53:270–278, 2006.

[114] Carrier J, Archambault L, Beaulieu L and Roy R. Validation of GEANT4, an object-oriented Monte Carlo toolkit, for simulations in medical physics. *Med. Phys.*, 31:484–492, 2004.

[115] Archambault L, Beaulieu L, Carrier J F, *et al*. Overview of Geant4 applications in medical physics. *IEEE Nuclear Science Symposium Conference Record*, 3:1743–1745, 2003.

[116] Granero D, Pérez-Calatayud J, Casal E, Ballester F and Venselaar J. A dosimetric study on the Ir-192 high dose rate Flexisource. *Med. Phys.*, 33:4578–4582, 2006.

[117] Rivard M J, Granero D, Perez-Calatayud J and Ballester F. Influence of photon energy spectra from brachytherapy sources on Monte Carlo simulations of kerma and dose rates in water and air. *Med. Phys.*, 37:869–876, 2010.

[118] Ababneh E, Dababneh S, Qatarneh S and Wadi-Ramahi S. Enhancement and validation of Geant4 brachytherapy application on clinical HDR 192Ir source. *Radiat. Phys. Chem.*, 103:57–66, 2014.

[119] Raaijmakers A J E, Raaymakers B W and Lagendijk J J W. Experimental verification of magnetic field dose effects for the MRI-accelerator. *Phys. Med. Biol.*, 52:4283–4291, 2007.

[120] Perez-Calatayud J, Ballester F, Das R K, DeWerd L A, Ibbott G S, Meigooni A S, Ouhib Z, Rivard M J, Sloboda R S and Williamson J F. Dose calculation for photon-emitting brachytherapy sources with average energy higher than 50 keV: Report of the AAPM and ESTRO. *Med. Phys.*, 39:2904–2929, 2012.

[121] Baglin C. Nuclear data sheets for A=192. *Nucl. Data Sheets*, 113:1871–2111, 2012.

[122] Nath R, Anderson L L, Luxton G, Weaver K A, Williamson J F and Meigooni A S. Dosimetry of interstitial brachytherapy sources: Recommendations of the AAPM radiation therapy committee task group no. 43. *Med. Phys.*, 22:209–234, 1995.

[123] Raaijmakers A J E. *MR-guided radiotherapy: magnetic field dose effects*. Phd thesis (appendix b.2), Utrecht University, 2008.

[124] Tanderup K, Beddar S, Andersen C E, Kertzscher G and Cygler J E. In vivo dosimetry in brachytherapy. *Med. Phys.*, 40:070902, 2013.

[125] Kertzscher G, Rosenfeld A, Beddar S, Tanderup K and Cygler J E. In vivo dosimetry: trends and prospects for brachytherapy. *Br. J. Radiol.*, 87:20140206, 2014.

[126] Nose T, Chatani M, Otani Y, Teshima T and Kumita S. Real-time verification of a high-dose-rate Iridium 192 source position using a modified C-arm fluoroscope. *Int. J. Radiat. Oncol. Biol. Phys.*, 97:858–865, 2017.

[127] Kuglin C D and Hines D C. The phase correlation image alignment method. *Proc. IEEE Int. Conf. Cybernet. Society*, pages 163–165, 1975.

[128] Pruessmann K P, Weiger M, Scheidegger M B and Boesiger P. SENSE: sensitivity encoding for fast MRI. *Magn. Reson. Med.*, 42:952–962, 1999.

[129] Klein S, Staring M, Murphy K, Viergever M A and Pluim J P W. elastix: A toolbox for intensity-based medical image registration. *IEEE Trans. Med. Imaging*, 29:196–205, 2010.

[130] Kirisits C, Rivard M J, Baltas D, *et al*. Review of clinical brachytherapy uncertainties: Analysis guidelines of GEC-ESTRO and the AAPM. *Radiotherapy and Oncology*, 110:199–212, 2014.

[131] Eggers H, Weiger M, Proksa R, Pruessmann K P and Boesiger P. Real-time reconstruction for sensitivity encoded magnetic resonance imaging. *Proc. Intl. Soc. Mag. Reson. Med.*, 7:1649, 1999.

[132] Hansen M S, Atkinson D and Sorensen T S. Cartesian SENSE and k-t SENSE reconstruction using commodity graphics hardware. *Magn. Reson. Med.*, 59:463–468, 2008.

[133] Beld E, Seevinck P R, Schuurman J, Zijlstra F, Viergever M A, Lagendijk J J W and Moerland M A. Testing an MR-compatible afterloader for MR-based source tracking in MRI guided HDR brachytherapy. *Radiother. Oncol.*, 123:S141–S142, 2017.

[134] Campbell-Washburn A E, Faranesh A Z, Lederman R J and Hansen M S. MR sequences and rapid acquisition for MR guided interventions. *Magn. Reson. Imaging Clin. N. Am.*, 23:669–679, 2015.

[135] Beld E, Moerland M A, Zijlstra F, Viergever M A, Lagendijk J J W and Seevinck P R. MR-based source localization for MR-guided HDR brachytherapy. *Phys. Med. Biol.*, 63:085002, 2018.

[136] Zhou J, Zamdborg L and Sebastian E. Review of advanced catheter technologies in radiation oncology brachytherapy procedures. *Cancer Manag. Res.*, 7:199–211, 2015.

[137] Beaulieu L, Racine E, Han D Y, Vigneault E, Hsu I C and Cunha J A M. Real-time electromagnetic tracking-based treatment platform for high-dose-rate prostate brachytherapy: Clinical workflows and end-to-end validation. *Brachytherapy*, 17:103–110, 2018.

[138] Smith R L, Hanlon M, Panettieri V, Millar J L, Matheson B, Haworth A and Franich R D. An integrated system for clinical treatment verification of HDR prostate brachytherapy combining source tracking with pretreatment imaging. *Brachytherapy*, 17:111–121, 2018.

[139] Wybranski C, Eberhardt B, Fischbach K, *et al*. Accuracy of applicator tip reconstruction in MRI-guided interstitial 192Ir-high-dose-rate brachytherapy of liver tumors. *Radiother. Oncol.*, 115:72–77, 2015.

[140] Dietrich O, Raya G, Reeder S B, Reiser M F and Schoenberg S O. Measurement of signal-to-noise ratios in MR Images: influence of multichannel coils, parallel imaging, and reconstruction filters. *J. Magn. Reson. Imaging*, 26:375–385, 2007.

[141] El-Sharkawy A M, Schär M, Bottomley P A and Atalar E. Monitoring and correcting spatio-temporal variations of the MR scanner's static magnetic field. *Magn. Reson. Mater. Phys. Biol. Med.*, 19:223–236, 2006.

[142] Xiang Q S. Phase-sensitive image reconstruction. In *Proc. Intl. Soc. Magn. Reson. Imaging 21*, Salt Lake City, USA, 2013.

[143] Bernstein M A, King K F and Zhou X J. *Handbook of MRI pulse sequences*. Elsevier Academic Press, 2004.

[144] Frank S J, Mourtada F, Crook J and Ménard C. Use of magnetic resonance imaging in low-dose-rate and high-dose-rate prostate brachytherapy from diagnosis to treatment assessment: Defining the knowledge gaps, technical challenges, and barriers to implementation. *Brachytherapy*, 16:672–678, 2017.

[145] Ménard C, Pambrun J F and Kadoury S. The utilization of magnetic resonance imaging in the operating room. *Brachytherapy*, 16:754–760, 2017.

[146] Yu K K and Hricak H. Imaging prostate cancer. *Radiol. Clin. North Am.*, 38:59–85, 2000.

[147] Lauzon M L and Frayne R. Analytical characterization of RF phase-cycled balanced steady-state free precession. *Concepts Magn. Reson.*, 34A:133–143, 2009.

[148] Beld E, Seevinck P R, Schuurman J, Viergever M A, Lagendijk J J W and Moerland M A. Development and testing of a magnetic resonance (MR) conditional afterloader for source tracking in magnetic resonance imaging-guided high-dose-rate (HDR) brachytherapy. *Int. J. Radiat. Oncol. Biol. Phys.*, 102:960–968, 2018.

[149] Maspero M, Van den Berg C A T, Zijlstra F, Sikkes G G, De Boer H C J, Meijer G J, Kerkmeijer L G W, Viergever M A, Lagendijk J J W and Seevinck P R. Evaluation of an automatic MR-based gold fiducial marker localisation method for MR-only prostate radiotherapy. *Phys. Med. Biol.*, 62:7981–8002, 2017.

[150] Horn B K P and Schunck B G. Determining optical flow. *Artif. Intell.*, 17:185–203, 1981.

[151] Denis de Senneville B, Zachiu C, Ries M and Moonen C. EVolution: an edge-based variational method for non-rigid multi-modal image registration. *Phys. Med. Biol.*, 61:7377–7396, 2016.

[152] Zachiu C, Denis de Senneville B, Moonen C T W, Raaymakers B W and Ries M. Anatomically plausible models and quality assurance criteria for online mono- and multi-modal medical image registration. *Phys. Med. Biol.*, 63:155016, 2018.

[153] Borot de Battisti M, Denis de Senneville, B Maenhout M, Hautvast G, Binnekamp D, Lagendijk J J W, Vulpen M Van and Moerland M A. Adaptive planning strategy for high dose rate prostate brachytherapy - a simulation study on needle positioning errors. *Phys. Med. Biol.*, 61:2177–2195, 2016.

[154] Borman P T S, Tijssen R H N, Bos C, Moonen C T W, Raaymakers B W and Glitzner M. Characterization of imaging latency for real-time MRI-guided radiotherapy. *Phys. Med. Biol.*, 63:155023, 2018.

Chapter 8

Samenvatting

Samenvatting

MRI levert superieur contrast tussen zachte weefsels en wordt daarom toegepast bij HDR brachytherapie. Momenteel wordt MRI toegepast voor handmatige katheter reconstructie en planning van de behandeling. Echter, technieken voor real-time verificatie van de behandeling zijn momenteel niet klinisch beschikbaar. MRI lijkt een ideale beeldvormingstechniek voor real-time geleiding en verificatie van de behandeling, omdat het zowel visualisatie van de anatomie als visualisatie/detectie van interventionele instrumenten mogelijk maakt. Daarom hebben wij een MRI-geleide HDR brachytherapie workflow voorgesteld, waarin we een MRI-gebaseerde lokalisatie van de bron toepassen voor reconstructie van de bron dwell posities en voor real-time verificatie van de behandeling. Dit vroeg om de volgende studies: een onderzoek van de impact van het magnetisch veld op de dosisverdeling, het ontwikkelen van een MR-conditional afterloader en een methode voor MRI-gebaseerde tracking van de bron en het tegelijkertijd visualiseren van de anatomie. Deze thesis beschrijft de belangrijkste technische ontwikkelingen die nodig zijn voor real-time MRI-geleide HDR brachytherapie.

In een situatie waarin real-time verificatie van de behandeling wordt toegepast, moet de patiënt in de MRI scanner gepositioneerd zijn op het moment van bestralen. In **hoofstuk 2** werd de impact van het magnetisch veld van de MRI scanner op de dosisverdeling onderzocht. Een magnetisch veld veroorzaakt afbuiging van elektronen in het vlak loodrecht op het magnetisch veld, en leidt tot een verminderde laterale scattering in de richting parallel met het magnetisch veld. Monte Carlo simulaties werden uitgevoerd om de invloed van het magnetisch veld op de dosisverdeling rondom een HDR brachytherapie bron (Ir-192) te onderzoeken voor magnetische veldsterktes van 1.5 T, 3 T en 7 T. De resultaten lieten zien dat de dosisverdeling nauwelijks beïnvloed werd door het magnetisch veld voor alle onderzochte veldsterktes, waarbij de verschillen lager dan of rond het niveau van de statistische fout lagen (dat wil zeggen rond 1.7% op 10 mm van de bron). Echter, er moet aandacht besteed worden aan dosisafwijkingen in het geval dat er luchtbellen aanwezig zijn dichtbij de bron. Concluderend, vanuit een dosis-perspectief gezien, kan HDR brachytherapie veilig worden uitgevoerd in een MRI scanner, waarbij het magnetisch veld niet meegenomen hoeft te worden in de dosisberekeningen.

In **hoofdstuk 3** is een methode beschreven voor real-time MRI-gebaseerde bron lokalisatie met hoge spatiële en temporele resolutie, zoals benodigd voor HDR brachytherapie. Het doel van MRI-gebaseerde lokalisatie van een HDR brachytherapie bron bestaat uit twee aspecten. Ten eerste, het maakt het mogelijk om de bron dwell posities te bepalen tijdens het bestralen, voor real-time verificatie van de behandeling. Ten tweede, wanneer een dummy bron gebruikt wordt, maakt het automatische reconstructie van de bron dwell posities na het inbrengen van de katheters mogelijk, benodigd voor de dosisplanning. De methode bestaat uit simulatie van het MRI artefact veroorzaakt door de HDR bron, gevolgd door een fase-correlatie lokalisatie algoritme toegepast op het gesimuleerde en het gescande artefact om de positie van de HDR bron in het MRI beeld te bepalen. Om de temporele resolutie tijdens scannen te vergroten werd de spatiële resolutie verkleind en werd een sub-pixel lokalisatie algoritme geïntroduceerd. Om de dynamische scantijd nog verder te verkleinen werd paral-

lel imaging (SENSE) toegepast. Een validatie studie werd uitgevoerd met behulp van een vergelijking met CT, waarbij de nauwkeurigheid en precisie van de methode werden vastgesteld. Dit resulteerde in lokalisatie van de HDR bron met een grote nauwkeurigheid (0.4-0.6 mm) en een grote precisie ($\leq$0.1 mm), bij een hoge temporele resolutie (0.15-1.2 s per slice). De voorgestelde methode voor MRI-gebaseerde bron lokalisatie maakt zowel real-time verificatie van de behandeling als automatische detectie van de bron dwell posities mogelijk.

Real-time verificatie van de behandeling, waarbij gebruik wordt gemaakt van MRI-gebaseerde bron lokalisatie, vraagt om de ontwikkeling van een MR-conditional afterloader, zoals beschreven in **hoofdstuk 4**. Het in de praktijk brengen van MRI-gebaseerde bron lokalisatie vereist dat de patiënt in de MRI scanner gepositioneerd is tijdens het bestralen. Daarom moet de afterloader direct naast de MRI scanner geplaatst worden, waarbij beide systemen tege-lijkertijd correct moeten functioneren. Een prototype MR-conditional afterloader is ontwikkeld en het tegelijkertijd functioneren van dit prototype en een 1.5 T MRI scanner werd getest in een experimentele opstelling. De afterloader werd naast de scanner geplaatst en de bron werd naar vooraf bepaalde bronposities gestuurd in een katheter in een fantoom, terwijl tegelijkertijd MRI beelden werden verkregen. De methode voor MRI-gebaseerde bron lokalisatie werd toegepast om het functioneren van beide systemen te evalueren. Daarnaast werd de invloed van het aanwezig zijn en het gebruik van de afterloader op de werking van de MRI scanner onderzocht door het bepalen van radiofrequente (RF) interferentie, signal-to-noise (SNR) ratio en B_0 veld homogeniteit. Beide systemen functioneerden goed wanneer ze tegelijkertijd in werking waren en de stapgroottes tussen de verkregen bronposities kwamen overeen met de afterloader instellingen. Daarnaast lieten de testen zien dat de MRI beeldkwaliteit niet verminderd was door het aanwezig zijn en/of in werking zijn van de afterloader naast de scanner. Dit heeft de mogelijkheid tot het tegelijkertijd verkrijgen van MRI beelden en gebruik van een MR-conditional afterloader aangetoond.

Hoofdstuk 5 leidt tot meer flexibiliteit om MRI-gebaseerde object lokalisatie in de praktijk te brengen, voor klinisch relevante MRI sequenties. Daarbij is gebruik gemaakt van simulatie van de MRI artefacten die veroorzaakt worden door een HDR brachytherapie bron en een titanium naald. Het doel was om de mogelijkheden van verschillende klinisch relevante MRI sequenties te onderzoeken voor het faciliteren van tracking/lokalisatie van brachytherapie instrumenten, waarbij tegelijkertijd ook de anatomie gevisualiseerd kan worden. Vier typen MRI sequenties werden opgenomen in de simulaties: spoiled gradient echo, spin echo, balanced steady state free precession (bSSFP) en bSSFP met spectral attenuated inversion recovery (SPAIR) vet suppressie. Een fantoomstudie werd uitgevoerd om de MRI beelden te verkrijgen, waarbij twee manieren van aanpak voor afbeelding werden gebruikt: (I) vier snelle 2D MRI sequenties voor real-time tracking en (II) klinisch gebruikte 3D/volumetrische MRI sequenties voor robuuste object lokalisatie en positie verificatie. De resultaten lieten zien dat de gesimuleerde MRI artefacten overeen kwamen met de experimentele MRI artefacten, wat object lokalisatie mogelijk maakte voor alle onderzochte MRI sequenties. De gemiddelde afwijkingen van de gemiddelde object positie waren 0.2-0.3 mm voor alle toegepaste sequenties. Zodoende is aangetoond dat de simulaties van de MRI artefacten waardevol zijn voor real-time tracking van brachytherapie instrumenten voor verschillende klinisch relevante MRI sequenties, die tegelijkertijd visualisatie van de anatomie mogelijk maken.

Chapter 9

List of publications
Dankwoord
Curriculum Vitae

List of publications

Papers in peer-reviewed journals

Published papers

Ellis Beld, Peter R. Seevinck, Jeroen Schuurman, Max A. Viergever, Jan J.W. Lagendijk, Marinus A. Moerland. Development and testing of a magnetic resonance (MR) conditional afterloader for source tracking in magnetic resonance imaging-guided high-dose-rate (HDR) brachytherapy *Int. J. Radiat. Oncol. Biol. Phys.* 102: 960-968, 2018

Ellis Beld, Marinus A. Moerland, Frank Zijlstra, Max A. Viergever, Jan J.W. Lagendijk, Peter R. Seevinck. MR-based source localization for MR-guided HDR brachytherapy *Phys. Med. Biol.* 63: 085002, 2018

Ellis Beld, Peter R. Seevinck, Jan J.W. Lagendijk, Max A. Viergever, Marinus A. Moerland. Monte Carlo study of the impact of a magnetic field on the dose distribution in MRI-guided HDR brachytherapy using Ir-192 *Phys. Med. Biol.* 61: 6791-6807, 2016

Submitted manuscripts

Ellis Beld, Marinus A. Moerland, Jochem R.N. van der Voort van Zyp, Max A. Viergever, Jan J.W. Lagendijk, Peter R. Seevinck. MRI artifact simulation for clinically relevant MRI sequences for guidance of prostate HDR brachytherapy.

Abstracts and conference proceedings

Presented abstracts

Ellis Beld, Peter R. Seevinck, Max A. Viergever, Jan J.W. Lagendijk and Marinus A. Moerland. Towards real-time MR-guided high-dose-rate brachytherapy
- *Oral presentation, 6th MR in RT Symposium, 2018, Utrecht, The Netherlands*

Ellis Beld, Marinus A. Moerland, Max A. Viergever, Jan J.W. Lagendijk and Peter R. Seevinck. Validation study of high framerate source localization for MR-guided HDR brachytherapy
- *E-poster presentation, 26th Annual Meeting ISMRM, 2018, Paris, France*
- *Poster presentation, 10th Annual Meeting ISMRM Benelux Chapter, 2018, Antwerp, Belgium*

Ellis Beld, Marinus A. Moerland, Max A. Viergever, Jan J.W. Lagendijk and Peter R. Seevinck. Accuracy and precision of high frame rate MR-based HDR brachytherapy source localization
- *Oral presentation, 37th ESTRO Conference, 2018, Barcelona, Spain*

Ellis Beld, Marinus A. Moerland, Jeroen Schuurman, Frank Zijlstra, Max A. Viergever, Jan J.W. Lagendijk and Peter R. Seevinck. Simultaneous MR imaging and control of an MR compatible afterloader: feasibility of real-time HDR brachytherapy source tracking
- *E-poster presentation, 25th Annual Meeting ISMRM, 2017, Honolulu, Hawaii, USA*
- *Oral presentation, 9th Annual Meeting ISMRM Benelux Chapter, 2017, Tilburg, The Netherlands*

Ellis Beld, Marinus A. Moerland, Jeroen Schuurman, Frank Zijlstra, Max A. Viergever, Jan J.W. Lagendijk and Peter R. Seevinck. Testing an MR-compatible afterloader for MR-based source tracking in MRI guided HDR brachytherapy
- *Oral presentation, 36th ESTRO Conference, 2017, Vienna, Austria*

Ellis Beld, Marinus A. Moerland, Frank Zijlstra, Jan J.W. Lagendijk, Max A. Viergever and Peter R. Seevinck. Automatic high temporal and spatial resolution position verification of an HDR brachytherapy source using subpixel localization and SENSE
- *E-poster presentation, 24th Annual Meeting ISMRM, 2016, Singapore, Singapore*
- *Poster presentation, 8th Annual Meeting ISMRM Benelux Chapter, 2016, Eindhoven, The Netherlands*

Ellis Beld, Marinus A. Moerland, Job G. Bouwman, Frank Zijlstra, Jan J.W. Lagendijk, Max A. Viergever and Peter R. Seevinck. Localization of an HDR brachytherapy source using MR artifact simulation and phase-only cross correlation
- *E-poster presentation, 23th Annual Meeting ISMRM, 2015, Toronto, Canada*
- *Oral presentation, 7th Annual Meeting ISMRM Benelux Chapter, 2015, Gent, Belgium*

Submitted abstracts

Ellis Beld, Marinus A. Moerland, Max A. Viergever, Jan J.W. Lagendijk and Peter R. Seevinck. MRI artifact simulation for clinically relevant MR sequences for guidance of HDR brachytherapy
- *Oral presentation, 38th ESTRO Conference, 2019, Milan, Italy*

Ellis Beld, Marinus A. Moerland, Max A. Viergever, Jan J.W. Lagendijk and Peter R. Seevinck. MRI artifact simulation for clinically relevant MR sequences for guidance of prostate HDR brachytherapy
- *Submitted, 27th Annual Meeting ISMRM*

Awards

Young investigators award, 6^{th} *MR in RT Conference 2018*, Utrecht, The Netherlands

Elekta Brachytherapy award, 36^{th} *ESTRO Conference 2017*, Vienna, Austria

Dankwoord

Ik zou graag iedereen willen bedanken die, op welke manier dan ook, heeft bijgedragen aan het tot stand komen van mijn promotie en dit proefschrift.

Beste promotoren, Jan en Max, bedankt dat jullie mij de mogelijkheid en vrijheid hebben gegeven om dit onderzoek binnen de afdeling radiotherapie te kunnen doen. Ik heb hier ontzettend veel kunnen leren en heb er met veel plezier gewerkt. Ook wil ik jullie bedanken voor de kansen om naar meerdere internationale congressen te gaan, waar altijd weer veel te leren valt.

Rien en Peter, bedankt voor de prettige samenwerking en dat jullie mij de kans hebben gegeven om aan dit project te werken. Ook wil ik jullie bedanken voor het vertrouwen en de vrijheid die jullie mij hebben gegeven. Onze wekelijkse overleggen waren altijd erg nuttig, en zorgden altijd voor inzichten waarmee ik weer verder kon. Ik heb veel kunnen leren van jullie kritische blik en enthousiasme. Ook tijdens het scannen en bij het schrijven van de artikelen en dit proefschrift was jullie hulp altijd nuttig. Ik kijk er naar uit om nog te blijven samenwerken.

Ik wil alle leden van de beoordelingscommissie bedanken: prof. dr. B.W. Raaymakers, prof. dr. C.T.W. Moonen, Prof. I.H.M. Borel Rinkes, prof. dr. M. Hoogeman en dr. J. Lapre. Hartelijk bedankt voor het beoordelen van dit proefschrift.

Ik wil graag iedereen bedanken die betrokken is geweest bij het SoRTS project en bij het Starlit project. Dit heeft het mogelijk gemaakt dat ik het onderzoek kon doen dat in deze thesis beschreven staat.

Ik wil graag iedereen binnen Elekta waarmee ik binnen dit project contact heb gehad en heb samengewerkt bedanken; Jeroen, Yury, Bob, Hugo, en iedereen die heeft bijgedragen aan het ontwikkelen van de MR-conditional afterloader en iedereen die heeft geholpen met de testen die we hebben uitgevoerd met de MR-conditional afterloader.

Frank, bedankt voor de samenwerking voor de simulaties van de MRI artefacten. Zonder jouw kennis en hulp hadden we de simulaties niet op deze manier kunnen doen en was lokalisatie van de HDR bron en de naald niet op deze manier tot stand gekomen.

Bedankt aan alle collega's, alle OIO's/post-docs; Filipa, Anna, Maxence, Maureen, Matteo, Bjorn, Tom, Michaela, Tim, Markus, Charis, Tristan, Stefano, Jean-Paul, Pim, Robin, Maarten, Stefan, Soraya, Federico, Mark, Sophie, Hans, Joris, Daan, Mick, Jorine, Sanam, Dennis, Yulia, Anneloes en iedereen die ik nog vergeet. Dankjewel voor alle hulp, input en discussies tijdens meetings en bedankt voor de gezelligheid, de OIO-uitjes, pauzes, etentjes, borrels, concerten, gezelligheid tijdens de congressen, en de tripjes voor en na de congressen. Ook bedankt voor alle sportactiviteiten die we samen hebben gedaan: fietsen (o.a. de gave Elfstedentocht), hardlopen, spinning en tenniswedstrijdjes. Zonder al deze sportactiviteiten zou ik geen werk kunnen doen waarbij je zoveel stil zit achter de computer.

A special thanks to the colleagues in our room in Q2. Filipa, Maureen, Anna and Maxence. Thanks for being roommates in Q2 and for all the fun that we had inbetween the working hours. Thanks for sharing so much time together, for the help when needed and the discussions that we had. Your company made the office a very nice place to spend the working days.

Merel, Bob, Heleen, Kris, Eva, Jesper, Moniek en Hugo, bedankt dat we na de middelbare school nog altijd vrienden/vriendinnen zijn gebleven en dat we elkaar nog altijd blijven opzoeken, ook al wonen we verspreid door het land. Onze vakanties, weekendjes weg en de vele keren dat we afspreken zijn altijd weer als vanouds. Bedankt voor jullie openheid, interesse en gezelligheid; deze vriendschap is zo veel waard.

Lieve meiden van Leone Rode, waarbij ik vooral de Utrecht(+) clan wil bedanken: Martina, Ellen, Janneke, Marjolein, Janine, Mette, Karin, Annemarieke en Margoleen. Bedankt voor alle avonden die we afspreken om samen te eten, alle spelletjes dagen/avonden, alle drankjes in de stad, wielrenritjes en alle andere dingen die we nog samen ondernemen. En verder wil ik alle andere meiden van LR bedanken voor de activiteiten die er ook na onze studententijd nog voor zorgen dat we elkaar nog regelmatig blijven zien.

Nicole, Mariska en Hannelore. We hebben elkaar leren kennen tijdens onze stages bij de radiotherapie afdeling. En hoewel jullie deze afdeling hebben verlaten, zijn we elkaar nog regelmatig blijven zien en is het altijd weer even gezellig. Zo leuk om te merken hoeveel dingen we samen delen omdat we alle vier ongeveer tegelijkertijd ons vierjarige traject zijn ingegaan. En dat weekendje weg moet er zeker komen als we allemaal klaar zijn!

Sabine, Mayon, Daria, Karlijn, Sanne en Marleen, oud-huisgenootjes aan de Hoogstraat, waar ik de eerste twee jaar van mijn PhD met veel plezier heb gewoond. Bedankt voor de goede huiselijke sfeer die er altijd was, en voor alle keren samen koken, samen eten en lekker suf voor de tv hangen. Dit maakte het tot een super fijn plekje om te wonen.

Daarnaast wil ik nog mijn tennisteam bedanken voor alle keren dat we samen hebben getennist en getraind en bedankt voor alle gezelligheid tijdens de competitie en de afsluitende etentjes. Ook wil ik alle dames van Vrouwenwielrennen bedanken. Ik kijk altijd weer uit naar de zaterdagochtenden in de winter/het voorjaar en de woensdagavonden in de zomer, waarop we weer een training hebben. En het is super gaaf om voor allerlei activiteiten, zoals toertochten, een groepje bij elkaar te kunnen krijgen om mee te kunnen doen. Zoals ik hierboven al noemde, al deze sportactiviteiten zijn super fijn om te compenseren voor het stil zitten overdag tijdens het werken.

Filipa en Martina, bedankt dat ik bij ieder van jullie alles kwijt kan en dat jullie mijn paranimfen willen zijn op deze bijzondere dag.

Lieve familie; Mam, Moniek, en Petra, bedankt dat jullie er altijd voor me zijn. Elke keer dat ik weer in Twente kom, voelt dat nog weer als thuiskomen.

Curriculum Vitae

Ellis Beld was born on 12 October 1988 in Goor, the Netherlands. She attended VWO at De Waerdenborch in Goor (year one to three) and in Holten (year four to six). In 2007, she started the bachelor *Biomedische technologie* at the University of Twente in Enschede, The Netherlands. She finished the bachelor in 2011 with a thesis on 'Quantitative analysis of superparamagnetic iron oxides in phantoms with MRI and vibrating sample magnetometry'. She continued her master in *Biomedical engineering* (track: *Biomedical Physics*) at the University of Twente. She performed her master thesis research at the Department of Radiotherapy in the University Medical Center Utrecht. Her master thesis work was focused on 'Background field correction for phase-based MRI', which she completed in 2014. In June 2014, she started her PhD, also at the Department of Radiotherapy at the UMC Utrecht, under supervision of dr. ir. M.A. Moerland, dr. ir. P.R. Seevinck, prof. dr. ir. J.J.W. Lagendijk and prof. dr. ir. Viergever. Her research, presented in this thesis, focuses on the development of techniques/methods for real-time MRI-guidance of high dose rate (HDR) brachytherapy. Currently, Ellis is working as a post-doctoral researcher at the UMC Utrecht, continuing her research on the development of methods/techniques for MRI-guided HDR brachytherapy.